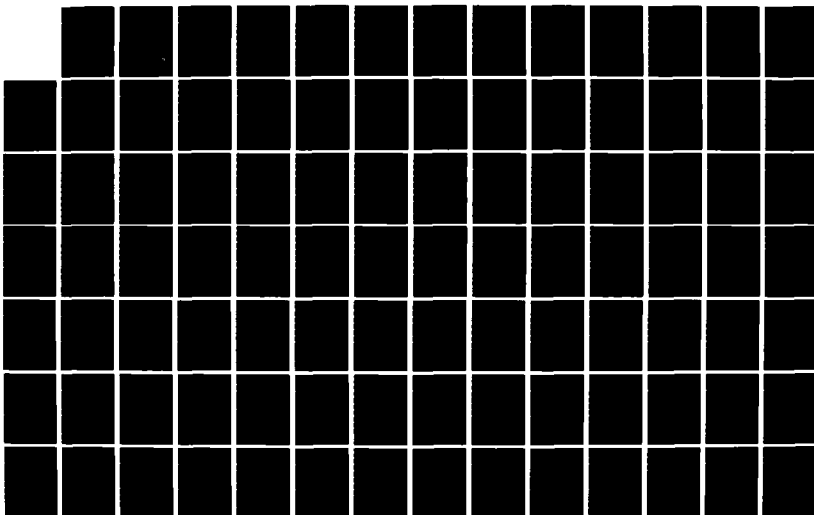AD-A158 841   LUMINESCENT PROPERTIES OF SEMICONDUCTOR ELECTRODES(U)   1/2
              WISCONSIN UNIV-MADISON DEPT OF CHEMISTRY A B ELLIS
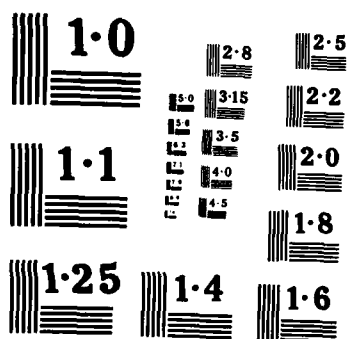   15 AUG 85 UWIS/DC/TR-85/2 N00014-78-C-0633

UNCLASSIFIED   F/G 9/1   NL

OFFICE OF NAVAL RESEARCH

Contract No. N00014-78-C-0633

Task No. NR 051-690

TECHNICAL REPORT NO. UWIS/DC/TR-85/2

Luminescent Properties of Semiconductor Electrodes

Arthur B. Ellis

Prepared for Publication

in

Chemistry and Structure at Interfaces: New Laser and
Optical Techniques
R.B.Hall and A.B. Ellis, Eds. VCH Publishers, Inc.

Department of Chemistry
University of Wisconsin-Madison
Madison, Wisconsin 53706

August 15, 1985

DTIC
ELECTE
SEP 0 4 1985
E

85 8 27 045

REPORT DOCUMENTATION PAGE		READ INSTRUCTIONS BEFORE COMPLETING FORM
1. REPORT NUMBER UWIS/DC/TR-85/2	2. GOVT ACCESSION NO. AD-A158 841	3. RECIPIENT'S CATALOG NUMBER
4. TITLE (and Subtitle) Luminescent Properties of Semiconductor Electrodes		5. TYPE OF REPORT & PERIOD COVERED
		6. PERFORMING ORG. REPORT NUMBER
7. AUTHOR(s) Arthur B. Ellis		8. CONTRACT OR GRANT NUMBER(s) N00014-78-C-0633
9. PERFORMING ORGANIZATION NAME AND ADDRESS Department of Chemistry University of Wisconsin-Madison Madison, WI 53706		10. PROGRAM ELEMENT, PROJECT, TASK AREA & WORK UNIT NUMBERS NR 051-690
11. CONTROLLING OFFICE NAME AND ADDRESS Office of Naval Research/Chemistry Program Arlington, Virginia 22217		12. REPORT DATE August 15, 1985
		13. NUMBER OF PAGES 127
14. MONITORING AGENCY NAME & ADDRESS(if different from Controlling Office)		15. SECURITY CLASS. (of this report) Unclassified
		15a. DECLASSIFICATION/DOWNGRADING SCHEDULE

16. DISTRIBUTION STATEMENT (of this Report)

Approved for Public Release: Distribution Unlimited

17. DISTRIBUTION STATEMENT (of the abstract entered in Block 20, if different from Report)

18. SUPPLEMENTARY NOTES

Prepared for publication in Chemistry and Structure at Interfaces: New Laser
and Optical Techniques. R. B. Hall and A. B. Ellis, Eds. VCH Publishers, Inc.

19. KEY WORDS (Continue on reverse side if necessary and identify by block number)

photoluminescence, electroluminescence, dead-layer model, cadmium sulfoselenide,
gallium arsenide, graded semiconductors, isotype heterojunction semiconductors

20. ABSTRACT (Continue on reverse side if necessary and identify by block number)

The literature regarding photoluminescence and electroluminescence from
semiconductor electrodes is reviewed.

Table of Contents

I. INTRODUCTION

The solid-liquid interface plays a key role in a multitude of disciplines ranging from heterogeneous catalysis to electrochemistry. Within the past decade, photoelectrochemistry has emerged as another active field of research dependent upon this interface. Employing semiconductors as electrodes, photoelectrochemical cells (PEC's) can mediate the conversion of optical (solar) energy to electrical energy or chemical fuels (1-5). These prospects for optical energy conversion have inspired an intense investigation of the semiconductor-electrolyte interface (6).

Attempts to characterize the interfacial region have profited greatly from the optical sensitivity of the semiconductor electrode. Most commonly, optically-based characterization has involved measurement of photocurrent as a function of electrode and electrolyte composition, electrode surface treatment, applied potential, and excitation intensity and wavelength (photoaction spectra). More recently, we and others have exploited the luminescence exhibited by many semiconductors to obtain information about the electrode-electrolyte interface. As a simple, in-situ technique, luminescence offers considerable promise for probing energetic and kinetic features of interfacial charge-transfer processes. Emission can also be used to establish the susceptibility of the semiconductor's excited-state decay routes to physical and chemical perturbation. The intent of this article is to summarize recent work which illustrates these principles.

Prior to discussing emissive properties, a description of PEC's is in order. A typical cell used for optical-to-electrical energy conversion is illustrated in Fig. 1. The cell consists of a semiconductor electrode, a Pt counterelectrode and an electrolyte containing the oxidized and reduced forms of a redox couple, A^+ and A; a reference electrode (saturated calomel (SCE), e.g.) is often present,

as well. In response to light exceeding its band gap energy, E_g, and with
a suitable redox couple, the n-type semiconductor pictured serves as an
anode for the oxidation of A to A^+; reduction of A^+ to A occurs at the
counterelectrode, completing a cycle which leaves the electrolyte composition
unchanged. The only result of the photoexcitation is thus the generation of
electricity. Electrolytes which have been used in this capacity include
those containing chalcogenide ions $(S^{2-}/S_n^{2-}$; Se^{2-}/Se_2^{2-}; $Te^{2-}/Te_2^{2-})$ (7)
or the ferrocene/ferricenium couple (8). Conversion of optical energy to
chemical fuels can also be accomplished with PEC's by running different
half reactions at the two electrodes. The classic example is the photoelectrolysis
of H_2O using metal oxide electrodes (9-12).

We should note at this point that the stability of PEC's constructed
from n-type semiconductors is   dependent upon the choice of redox couple.
In many instances, the semiconductor rather than the electrolyte species
is oxidized. A case in point is n-CdS which decomposes according to eq. [1]

$$CdS_{(s)} \xrightarrow{h\nu} Cd^{2+}_{(aq)} + S_{(s)} + 2e^- \qquad [1]$$
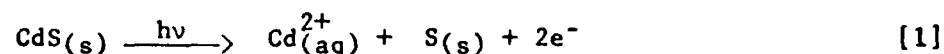
in a 1M OH^- electrolyte, but is protected from photocorrosion if sulfide or
polysulfide ions are present in the electrolyte; apparently, chalcogenide
ions in solution can kinetically compete with the lattice for holes photo-
generated in the solid (7). Considerable effort has been expended identifying
stable electrode-electrolyte combinations with the result that many common
semiconductors can now be studied under conditions of minimal photocorrosion.

The physics governing the semiconductor-electrolyte interface is analogous
to that which characterizes semiconductor-metal junctions. Schottky barriers

result in both cases, as discussed in detail by Gerischer and Fonash (6, 13, 14).
Key features are summarized in Fig. 2. Upon initial immersion of the semi-
conductor in the electrolyte in the dark, Fig. 2a, the chemical potentials of
the two phases - the Fermi level, E_f, for the semiconductor and the redox
potential, E_{redox}, for the electrolyte - will generally be different. Some
charge will then cross the interface, equilibrating the two phases; the charged
interface can be modeled as a parallel-plate capacitor. Because of the low
density of charge carriers, the electric field induced in the semiconductor
extends some distance W into the solid rather than being confined to the surface
as it would be for a metal. This zone, pictured in Fig. 2b with bent band edges,
is depleted of majority carriers and is thus called the depletion region. An
approximate expression for W is given by eq. [2], where ϵ is the semiconductor's

$$W = (2\epsilon\epsilon_o V_B/q N_D)^{1/2} \qquad [2]$$

dielectric constant; ϵ_o is the permittivity of free space; V_B is the amount of
band bending in the depletion region; q is the electronic charge; and N_D is the
charge carrier density in the semiconductor (n-type semiconductor).

Band bending plays a critical role in the semiconductor's ability to serve
as an electrode. Figure 3 depicts an n-type semiconductor after absorption
of ultraband gap photons. The electron-hole (e^--h^+) pairs generated by
photon absorption can be regarded as a "one-electron" picture of the semiconductor's
excited state. Among the deactivation paths available to e^--h^+ pairs is their
separation leading to photocurrent. This nonradiative decay path, symbolized
by the wavy arrows labeled k_x in the figure, is promoted by the electric field
in the solid. The potential gradient present near the surface draws the electron
through the bulk semiconductor to the counterelectrode where it serves as a
reductant; the hole is drawn to the surface where it serves as an oxidant.
This field-induced or drift contribution to photocurrent is augmented by a

contribution based on diffusion: minority carriers generated within a diffusion length, L_p (for holes), of the depletion region can also be captured for photocurrent.

An important feature of the electric field in the semiconductor is its potential dependence. In the idealized model of the semiconductor-electrolyte interface, the band edges are considered to be pinned at the surface and applied potential appears exclusively in the semiconductor. A prediction of this model is that the maximum photopotential of a PEC should be dependent on E_{redox}. Although some semiconductor electrodes satisfy this prediction, other materials exhibit photopotentials which are independent of E_{redox} [15,16]. An alternate model wherein the band edges are unpinned and applied potential appears in the electrolyte has been proposed for some of these systems. Described as Fermi level, pinning, the effect is attributed to a substantial density of surface electronic states which can make the surface appear metal-like insofar as its electrochemical response to applied potential is concerned. While photoelectrochemical and capacitance measurements have provided some insight into the origins of ideal, Fermi-level-pinned, and intermediate behavior, determining the manner in which applied potential is partitioned across the semiconductor-electrolyte interface remains an active area of research. Besides its intrinsic interest, the question also has a direct bearing on the efficiencies attainable with PEC's.

Competing with the field-induced separation of e^--h^+ pairs is recombination. Nonradiative recombination, symbolized by k_{nr} in Fig. 3, leads to heat via lattice vibrations. Its measurement in operating PEC's has been examined using the technique of photothermal spectroscopy [17]. Radiative recombination, denoted by k_r in Fig. 3, is the origin of luminescence in the solid.

The prediction of Fig. 3 is that emission will occur at energies near E_g. Such luminescence, sometimes called edge emission (18), can arise from several mechanisms. Besides the recombination of a free conduction band electron, e^-_{CB}, with a free valence band hole, h^+_{VB}, edge emission also occurs when electrons and/or holes are trapped in states near the band edges prior to recombination. Excitons represent another source of edge emission (18-20). A free exciton is a coulombically-bound $e^- - h^+$ pair which possesses hydrogenic-like states with energies near E_g; bound excitons wherein the e^- or h^+ is associated with a lattice defect site may also contribute to edge emission. Often, however, excitonic binding energies are low, minimizing their contributions to luminescence at room temperature.

Besides edge emission, many semiconductors exhibit subband gap luminescence. Figure 4 presents a more generalized picture of the electronic structure of the solid which accounts for this observation. The lines labelled "A" and "B" in the figure represent deep electronic states characteristic of the bulk material which can arise from lattice imperfections such as native defects (vacancies; interstitial atoms) or impurity atoms. Recombination involving holes or electrons trapped in these deep levels will, of course, lead to subband gap emission. Of particular importance to interfacial characterization are the states labelled "C" in the diagram. Confined to the (near-)surface region of the solid, these states can also participate in radiative transitions producing subband gap emission. Moreover, such surface states may play an important role in mediating interfacial charge transfer processes, as previously discussed.

In addition to its spectral distribution, luminescence is characterized by its excitation spectrum, quantum yield, and decay time. The excitation spectrum has several useful functions. In the case of samples possessing multiple excited states, communication among these states can be probed by

varying the excitation wavelength. More generally, the variation in emission intensity with optical penetration depth reflects material and surface properties. Although the dependence is complex (22-24), it has been used to evaluate the magnitude of surface recombination effects in several semiconductors (24,25) and to verify spatial inhomogeneity within the bulk of certain solids (26-29).

The radiative quantum yield, ϕ_r, and decay time, τ, contain information on the kinetics of excited-state decay. Quantum yields are obtained from steady-state measurements. Defined as photons emitted per photon absorbed, values of ϕ_r reflect the probability of radiative decay among all of the competing deactivation channels available to the solid; the probability, of course, is determined by the rate of radiative decay relative to rate constants associated with the other deactivation paths. Decay times are extracted from the time-resolved decay of emission intensity following pulsed excitation and reflect the longevity of the excited state. The temporal behavior can be quite complex, particularly if trapping states are present in the solid (30).

Initiated by light, the emission described thus far will henceforth be described as photoluminescence (PL). An important complementary technique for populating emissive excited states is electroluminescence (EL). In the case of EL, an electric current is the source of sample excitation. The phenomenon is exploited extensively in the design of LED's where its origin is the injection of minority carriers across a p-n junction; EL can also be produced by impact excitation (19, 31-33).

Semiconductor electrodes can exhibit EL by either of these mechanisms under suitable conditions. By far, the best-studied system involves the use of n-type semiconductors in oxidizing electrolytes. In such media, holes can be injected into the semiconductor's valence band. Hole injection can then be followed by recombination with electrons in the conduction band to yield light.

The PL and EL properties described thus far will be illustrated using specific semiconductor electrodes in the remainder of this article. Subsequent sections will discuss general PL properties of homogeneous semiconductor electrodes; a model which accounts for PL properties of these solids in PEC's; EL studies; and recent work with spatially inhomogeneous semiconductor electrodes.

II. GENERAL PL PROPERTIES

A. Background

Two early studies of emissive semiconductor electrodes were undertaken with p-GaP (34) and n-ZnO (35). In the former case, subband gap PL at ~1.8 eV (E_g ~2.25 eV) was studied while the electrode was used as a photocathode for H_2 evolution in 1 N H_2SO_4 electrolyte. Quenching of PL intensity by a few percent, observed through use of a modulation technique, accompanied the passage of photocurrent; the photocurrent quantum efficiency, ϕ_x, was only ~0.01 in this experiment, even with low optical penetration depths. Also observed was a strong dependence of PL intensity on excitation wavelength which the authors analyzed in terms of surface recombination effects.

Samples of n-ZnO and Cu- and In-doped ZnO (ZnO:Cu; ZnO:In) were employed in similar studies conducted in a pH 1.5 solution prepared from KCl and HCl. The redox chemistry in this PEC is electrode corrosion by eq. [3]. Although the electrode is chemically unstable under the conditions employed, many of the PL

$$ZnO_{(s)} \xrightarrow{\ h\nu\ } Zn^{+2}_{(aq)} + \frac{1}{2} O_{2(g)} + 2e^- \qquad [3]$$
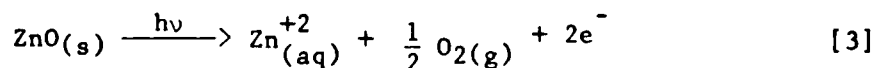
observations made have subsequently been shown to be characteristic of stable PEC's, as well. In particular, the subband gap green PL which was monitored at 500 nm (~2.5 eV; E_g ~3.2 eV) retains its spectral distribution over a substantial potential regime. What does change with potential is the PL intensity. Figure 5 reveals that PL quenching accompanies passage of anodic

photocurrent corresponding to eq. [3] when ultraband gap 350-nm light is used for excitation. For the samples examined, a roughly mirror-image relationship of the photocurrent and PL intensity curves was observed, as indicated in Fig. 5. If, however, excitation wavelengths on the absorption edge are used, little photocurrent and potential-independent PL intensity obtains; at these wavelengths, a substantial fraction of the incident light is absorbed well beyond the depletion width.

B. n-CdS:Te

Our early studies examined many of the phenomena observed for n-ZnO using n-CdS:Te electrodes (36-38). The selection of CdS:Te was made with the expectation that its PEC properties would mimic those for CdS, from which stable PEC's had been constructed, and that it would be very emissive at room temperature (39-44). Both expectations were satisfied.

In addition to green edge emission at 510 nm (E_g $\sim$2.4 eV), the presence of the isoelectronic dopant Te produces, depending on Te concentration, bright orange or orange-red PL at 295 K; we estimated ϕ_r as being $\sim$$10^{-4}$-$10^{-2}$ (38). Solid-state studies of CdS:Te indicate that Te substitutes for S in the CdS lattice and, at concentrations of $\sim$1 ppm, introduces a state $\sim$0.2 eV above the edge (39-44). Holes trapped at Te sites can coulombically bind an electron in or near the conduction band; the radiative collapse of this exciton produces the observed orange PL. At Te concentrations approaching 1000 ppm, a state located $\sim$0.4-0.6 eV from the valence band edge is introduced as a consequence of Te nearest-neighbor interactions; a PL band at $\sim$730 nm results from excitons trapped at these sites. Roessler has reported that the Te concentration in CdS:Te can be estimated from the position and half-width of the sample's PL spectrum (42). It is also noteworthy that local excitation of CdS:Te samples yields global emission, presumably through internal scattering of the subband gap emission (38).

Like n-CdS, polycrystalline and single-crystal n-CdS:Te samples can be incorporated into PEC's employing chalcogenide ions to yield stable cells for mediation of optical-to-electrical energy conversion. Stability is typically demonstrated in prolonged experiments by 1) lack of crystal weight loss; 2) lack of surface damage; 3) evidence of competitive electrolyte redox chemistry; and 4) photocurrent stability. We found that CdS:Te mimicked CdS in these experiments, showing excellent short-term and good long-term stability. The emission of CdS:Te served as another measure of stability with variations in PL intensity reflecting modest deterioration of PEC properties in long-term, high-intensity operation.

Having established PEC stability, the dependence of PL properties on excitation wavelength and applied potential was investigated for CdS:Te-based PEC's. In typical experiments, a PEC was set up in the sample compartment of an emission spectrometer. Samples were oriented at ~45° to both the incident excitation from an Ar^+ laser and the detection optics so as to examine front-surface PL. Complete PL spectra could then be recorded as a function of various PEC parameters in a single geometry.

For CdS:Te, the subband gap PL spectral distribution is independent of potential between open circuit (~-1.0 to -1.5 V vs. SCE) and -0.3 V vs. SCE, indicating that the intraband gap states bend in parallel with the band edges. The spectral invariance obtains for both ultraband gap (<500 nm) excitation and for deeply penetrating 514.5-nm excitation. As a consequence, PL can be monitored at a single wavelength, usually λ_{max}. Photocurrent and PL intensity can thus be simultaneously measured as a function of applied potential to yield what we call iLV curves.

PL quenching with increasingly positive applied potential is a general feature of CdS:Te-based PEC's when ultraband gap excitation is employed.

General iLV data for this system are pictured in Fig. 6. With 496.5-nm excitation (bottom panel), photocurrent and PL intensity show an inverse dependence on potential. With band edge 514.5-nm excitation of comparable intensity, much smaller photocurrents and stronger, potential-independent PL intensity results. These results were reminiscent of those found for n-ZnO-based PEC's and prompted a similar qualitative explanation: when incident light is absorbed predominantly in the depletion region, photogenerated $e^- - h^+$ pairs can be efficiently separated for photocurrent at the expense of recombination. Increasingly positive potentials augment band bending in n-type semiconductor electrodes; as the electric field is enhanced, photocurrent and PL become more and less probable, respectively. This tug-of-war among decay routes is less pronounced with deeply penetrating incident light. In this case, most $e^- - h^+$ pairs are formed beyond the depletion region and deactivation routes are thus relatively insensitive to applied potential. The large difference in PL intensity with more deeply penetrating light suggests that nonradiative surface recombination is substantial in these systems.

The significant dependence of the degree of PL quenching on optical penetration depth impelled us to consider parameters which might enable us vary this depth relative to the depletion width in a given material. A logical choice was temperature. For most semiconductors, an increase in temperature decreases E_g, red-shifting the absorption edge (20). The optical band gap temperature coefficient, dE_g/dT, for undoped CdS of -5.2×10^{-4} eV/K (45) suggested that CdS:Te might absorb a larger fraction of 514.5-nm light in the depletion region if temperature were to be increased. These expectations were realized using a cell modified for variable-temperature work (46,47).

Using PEC's employing single-crystal CdS or 100 ppm CdS:Te electrodes, we found that 514.5-nm-induced photocurrent does increase by an order of magnitude between 20 and 100°C, whereas more modest increases of <20%

obtain with 501.7-nm excitation. The key feature of full <u>iLV</u> curves, Fig. 7,

is that the high-temperature, 514.5-nm PL intensity curve exhibits a potential

dependence (∿27% quenching between open circuit and 0.7 V vs. a Ag pseudoreference

electrode) in sharp contrast ᴜᴊ the potential independence found at room

temperature (curves D' and B'). Energy conversion parameters for these PEC's

as a function of temperature and incident wavelength are given in Table I.

Note, in particular, the substantial increases in maximum energy conversion

efficiency, η_{max}, and in maximum ϕ_x between 23 and 73°C for 514.5-nm excitation,

consistent with a substantially reduced optical penetration depth.

For CdS:Te, PL quenching is not restricted to the Te-exciton-based emission.

As mentioned above, this solid also exhibits green edge emission. We have

studied PL quenching of both bands and used our results to infer the existence

of excited-state communication in the solid (48). The panels of Fig. 8

present complete PL spectra for single-crystal,100-ppm CdS:Te electrodes as a

function of temperature and potential. Curves numbered "1" represent

open-circuit data and show that both bands are quenched by temperature with

the Te-based band quenched more rapidly. A semilog plot of the ratio of 510-

to 600-nm PL intensity vs. T^{-1} is linear with a slope corresponding to ∿0.2 eV;

this apparent activation energy agrees nicely with the ∿0.2 eV energy gap

expected between the two emissive states based on the energetic location of the

Te state relative to the valence band edge. It should be noted that both PL

bands roughly maintain their spectral distributions over the temperature

range indicated in Fig. 8. In fact, little change is observed for the

Te-based band even at 77 K. The edge PL band, on the other hand, tracks the

band gap and blue shifts to ∿490 nm by 77 K.

We sought additional evidence for thermal equilibration of the two excited

states from temporal studies. Rather than having identical decay times, as

anticipated for thermalized states (49,50), we found very different time-resolved

properties: the decay time for the edge PL is faster than the pulse from the N_2-pumped dye laser ($\sim$7 ns)used for 458-nm excitation; intensity-time curves for the 600-nm PL band have rise times of <10 ns and exhibit nonexponential decay with typical $\tau_{1/e}$ values of 120±40 and 80±30 nsec at 295 and 333 K, respectively. Similar data were reported for the 600-nm band by Perone and Richardson (51). In assessing the temporal and steady-state open-circuit results, the data suggest that thermal equilibrium between the two states exists, but that its establishment is relatively slow.

When brought into circuit, the CdS:Te electrode's green PL, like its orange emission, is quenched. The crucial result depicted in Fig. 8 is that at all three temperatures both PL bands are quenched essentially in parallel. Parallel PL quenching also supports excited-state communication, although several mechanistic schemes are compatible with the result. At present, we favor a scheme based on the two states leading to edge and subband gap PL, states A and B, respectively. In principle, a nigher-energy excited state C could participate, as well, but the similar iLV properties obtained with 457.9- and 476.5-nm light argue against its involvement: energetically, 476.5 nm is sufficiently proximate to the onset of the edge emission band that state A is likely populated directly. We thus favor an excited-state scheme wherein state A is populated and subsequently interconverts with state B. Quenching of interconverting excited states has been analyzed in detail for molecular systems (50). In general, parallel quenching of A and B can be expected so long as the quenching process does not upset the interconversion of the two states. Disruption of interconversion requires that a substantial fraction of quenching comes via the lower-energy state. Since we do not observe a significant departure from parallel quenching, we suspect that state A is the principal contributor to photocurrent, i.e.,

holes are extracted for photocurrent predominantly from the valence band rather than from the Te state.

In concluding this section on CdS:Te, we call attention to some additional temporal studies of the orange, 600-nm band obtained in PEC's of sulfide electrolyte (51). Although the intensity-time curves are complex and dependent on incident intensity, some of the properties seem to roughly correlate with steady-state PL measurements. In particular, with ultraband gap excitation, decay times, like steady-state PL intensity, increased with more negative potentials. And with band edge 515-nm excitation, longer and potential-independent decay times were found.

C. $n-CdS_XSe_{1-X}$

Among semiconductor electrodes, n-CdSe has, like n-CdS, been the subject of numerous studies. Its relatively small band gap ($\sim$1.7 eV), the ease with which single-crystal, polycrystalline, and thin film samples can be fashioned into electrodes, and the stabilizing effects of chalcogenide electrolytes have been largely responsible for the extensive use of n-CdSe in PEC's (52). The ability of n-CdS and n-CdSe to form solid solutions of $n-CdS_XSe_{1-X}$ ($0 \leq X \leq 1$) prompted us to examine PL properties of these solids as a family, using the stabilizing chalcogenide electrolytes for PEC construction (52-54).

Band gaps of the CdS_XSe_{1-X} samples, estimated by a variety of techniques, decrease smoothly with X from $\sim$2.4 to 1.7 eV (55-59). All of the samples examined exhibit weak edge emission at 295 K, as shown in Fig. 9 for five compositions. This assignment is based on the energetic proximity of E_g and the bands' temperature dependence. Table II summarizes features of the PL spectra and reveals that the bands blue-shift by $\sim$0.07-0.10 eV in passing from 295 to 77 K, consistent with estimates of dE_g/dT from photoconductivity measurements (57,58,60). A useful feature of the 295 K PL band positions is that they serve as a diagnostic tool for determining composition. As shown in

Fig. 10 and previously reported from PL and cathodoluminescence studies (61),
the PL maxima expressed in nm vary linearly with composition according to eq. [4].

$$\lambda_{max}(nm) \cong 718\text{-}210 \ X \qquad\qquad [4]$$

Compositions were independently determined by electron microprobe analysis.

Table II also provides an upper-limit estimate of ϕ_r. Enhancements in PL
intensity of $\sim$50-200 with cooling under comparable excitation conditions
correspond to upper limits on ϕ_r of 0.02-0.005 at 295 K. A more accurate
estimate of ϕ_r was made by adapting a technique introduced by Wrighton, et al. (62).
What is done is to subtract the intensity of laser light reflected by a sample
of CdS_XSe_{1-X} from that reflected by a nonabsorbing standard, an MgO pellet in
the same geometry. This serves as the "photons absorbed" needed for the ϕ_r
calculation and is divided into the intensity emitted by the CdS_XSe_{1-X} sample,
after correction for detector response (52). Typical ϕ_r values for Br_2/MeOH-etched
CdS_XSe_{1-X} samples were $\sim 10^{-4}$.
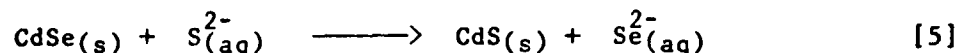
While examining CdS_XSe_{1-X} samples, we found evidence that spatial effects
are important in PL measuements, particularly proximity to the interfacial
region. These effects were most strongly exhibited by CdSe. Our initial
observation, pictured in Fig. 11, was that the PL spectrum of CdSe was
dependent on excitation wavelength. In particular, Fig. 11 demonstrates that
less deeply penetrating 457.9-nm excitation produces a broader PL spectrum
than 632.8-nm light with the spectral mismatch almost exclusively in the
high energy tail of the band. We attribute this to self-absorption effects:
The sharp rise in CdSe absorptivity at $\sim$720 nm and the roughly 3-fold difference
in absorptivity for the two excitation wavelengths (63) imply that PL produced
by the longer excitation wavelength must traverse a longer average path length
to be detected and that the high-energy portion of the PL band is thus more

likely to suffer absorption by the crystal in the process. We found similar effects with the other CdS_xSe_{1-x} samples, as well (53,54).

A more dramatic illustration of the spatial origin of PL and one which may have important consequences for the study of interfacial interactions emerged from etching experiments involving CdSe. After Br_2/MeOH etching, little difference was observed if the PL spectrum was measured in air or water. However, addition of OH^- to the water resulted in up to threefold enhancements in PL intensity; a slight broadening of the high-energy tail of the PL band accompanying the OH^- addition suggests that (near-)surface regions enhance their contributions to PL. An even larger effect was obtained with photo-electrochemical etching (64,65) wherein some photoanodic corrosion was permitted to occur in OH^- electrolyte. PL intensity increases substantially after this etch and the spectrum broadens as expected for greater (near-)surface contributions to PL; on occasion we have seen up to 50-fold increases in PL intensity. The effect of PEC etching is intriguing and has often resulted in greatly improved PEC output characteristics (64,65). Our inference that PEC etching reduces (near-)surface nonradiative recombination has received support from electron beam induced current (EBIC) measurements; in those studies, improved charge collection efficiency was noted after PEC etching for CdS/Au Schottky barriers (66). As to the origin of the effect in CdSe, several possibilities exist including production of a more emissive surface morphology and less efficient quenching of PL from (near-)surface regions of CdSe by electrolyte species or surface states. At present, the point to be emphasized is that this study provides evidence that PL from the solid might be used to probe physicochemical interactions at the semiconductor-electrolyte interface.

Another compelling illustration of the utility of PL measurments for interfacial studies involves characterization of polycrystalline CdSe photoelectrodes.

When CdSe is used as an electrode in polysulfide electrolyte, an exchange

reaction can take place leading to formation of CdS_XSe_{1-X} compositions,

eq. [5] (67). Silberstein and Tomkiewicz have exploited PL and Raman

$$CdSe_{(s)} + S^{2-}_{(aq)} \longrightarrow CdS_{(s)} + Se^{2-}_{(aq)} \qquad [5]$$

spectroscopy as nondestructive techniques for demonstrating the occurrence

of exchange following use of an electrodeposited electrode in a PEC;

particularly persuasive is the appearance of PL above the CdSe band gap

energy (68). By conducting these measurements at 77 and 4.2 K, the authors

were also able to characterize intraband gap states along with donor and acceptor

densities. We looked for evidence of eq. [5] using PL from single-crystal CdSe

electrodes, but saw no change in the PL spectrum with prolonged PEC operation.

The different result reported with the polycrystalline electrode may indicate

that grain boundaries facilitate the exchange reactions. Alternatively,

exchange may have occurred with the single-crystal material with lack of

CdS_XSe_{1-X} $(0 \leq X \leq 1)$ PL a result of nonemissive morphology or of extensive

quenching by, e.g., traps, electrolyte species or CdSe. If exchange were

confined to the (near-) surface region, PL may also not have been sufficiently

surface-sensitive to reveal an altered surface composition.

The examples described above show that surface chemistry can be

reflected in PL intensity and spectral distribution. Evidence that temporal

PL properties are influenced by surface chemistry has been reported, as well.

Harzion, et al. have studied time-resolved PL, photocurrent, and photopotential

for n-CdS and n-CdSe electrodes in PEC's employing polysulfide electrolyte (69,70).

In tandem, the techniques provided information on the rates of recombination

and transport properties within the solid and their perturbation by mechanical

polishing and chemical etching. PL decay times were on the order of 50 psec for mechanically-polished crystals and as long as ∿8 nsec for a component of decay from etched CdSe crystals. We measured decay times of etched CdS_xSe_{1-x} samples in air and found values of ∿20 nsec ($\tau_{1/e}$) for CdSe and $CdS_{0.11}Se_{0.89}$; for the more S-rich samples, our measurements were limited by the duration of the N_2 laser pulse, setting $\tau < 7$ nsec (53). It is worth emphasizing that temporal PL measurements in PEC's have only recently begun to be exploited. Measurements of PL in these systems may serve as a means for separating recombination kinetics from transport rates and cell RC time constants.

Still another tool which may be useful is the polarization of PL from semi-conductor electrodes. We have recently examined polarization properties of CdSe (71). Polarization effects can be anticipated for uniaxial semiconductors such as CdS_xSe_{1-x} possessing hexagonal structures. For CdSe, polarization effects had previously been reported in its 77 K PL spectrum (72) and its absorption (63,73), reflection (73), and photoaction (photoconductivity vs wavelength) spectra (58).

The 295 K PL spectra of CdSe a- and c- plates are shown in Fig. 12. For the a-plate, a polarizer was inserted to analyze for light emitted with its electric vector oscillating parallel and perpendicular to the c-axis, $E_{em}||C$ and $E_{em} \perp C$, respectively. Fig. 12 shows that use of the polarizer yields two bands with λ_{max} values of ∿715 and 708 nm, corresponding to $E_{em} \perp C$ and $E_{em}||C$, respectively. As expected, PL from the c-plate closely resembles in shape and energy the PL spectrum of the a-plate having $E_{em} \perp C$.

From earlier work, the two PL bands observed for the a-plate probably have their origin in a split valence band, as pictured in Fig. 13. A tight-binding treatment wherein the conduction and valence bands are derived from Cd 5s and Se 4p orbitals, respectively, leads, at k = (0,0,0), to the electronic structure

of Fig. 13 when crystal-field and spin-orbit effects are incorporated. The
indicated valence band splittings have been estimated from excitonic structure
observed in previous studies (58,63,73). The irreducible representations to
which the bands belong allow predictions, using the electric dipole selection
rules, of the allowedness and polarization properties of interband transitions.
All of the band-to-band transitions of Fig. 13 are allowed; those connecting
Γ_7 states are unpolarized, whereas those connecting Γ_7 and Γ_9 states should be
polarized with $E \perp C$.

Data in Fig. 12 are consistent with these predictions. The peak at 708 nm
exhibiting little polarization dependence is reasonably assigned to the
transition between the conduction band and the middle valence band. The
715-nm band polarized with $E_{em} \perp C$ is logically a composite of the 708-nm band
and the transition between the conduction band and the uppermost valence band.
By subtracting the 708-nm band from the 715-nm band, the lowest energy,
band-to-band transition should be unmasked. Such a deconvolution yields
a band with λ_{max} of ~717 nm and an energetic separation of the two transitions
of ~0.022 eV (using 717 and 708 nm), in reasonable agreement with the ~0.019 eV
separation estimated from 295 K photoconductivity data (58). Some caveats to
this analysis involve the dichroism of the solid (spectra are uncorrected for
this effect, which we estimate to be minor) and our description of the
transitions as "band-to-band". In the latter case, PL may actually involve
states near the band edges. However, if such states have the same symmetry
as the band edge with which they are associated, they will follow the same
selection rules with regard to polarization (58).

The existence of two emissive excited states prompted us to probe
communication between the states. With an energetic separation on the
order of kT, our expectation was that the two states would be in thermal
equilibrium. We found evidence for thermalization from temporal studies:

using the unpolarized 620-nm output of a N_2-pumped dye laser, a decay time, $\tau_{1/e}$, of $\sim$20 nsec was found to be independent of polarizer orientation and the portion of the PL spectrum monitored. In terms of Fig. 13, this result indicates that holes at or near the two uppermost valence band edges are thermalized prior to recombining with electrons at or near the conduction band edge. Attempts to extract the energetic separation of the states through steady-state, variable-temperature measurements of the PL intensity ratio were unsuccessful. Unlike the situation for CdS:Te (vide supra), the anticipated change in this ratio is small and, for measurements from 298-323 K, it fell within our experimental error.

Additional evidence for communication in steady-state measurements came from PEC experiments conducted with a CdSe a-plate electrode. The general observation that PL intensity is quenched in passing from open circuit to potentials yielding photoanodic current is manifest in this PEC. More significant, however, is the parallel quenching of the two PL bands, monitored through use of the polarizer. The mechanistic arguments made for CdS:Te are thus applicable to CdSe, as well: parallel quenching is expected so long as interconversion of the two emitting states is not disrupted.

In concluding this section we note that all of the single-crystal n-CdS$_x$Se$_{1-x}$ samples examined exhibit quenching of their PL intensity when used as PEC electrodes, as illustrated in Fig. 14; the extent of quenching and corresponding properties related to optical energy conversion are summarized in Table III for these PEC's. The point to be emphasized in this section is that despite their broad diversity of electronic structures and excited-state deactivation routes, all of the semiconductors discussed thus far share a common feature, viz., quenching of PL intensity accompanying their use as PEC electrodes. The next section will demonstrate that the quenching properties can be modeled in such a way as to provide information on interfacial energetics and kinetics.

III. MODELS FOR QUENCHING OF PL IN PEC'S

A. Background

An initial attempt at modeling PL quenching was made by Petermann, et al. in their study of n-ZnO-based PEC's (35). Their assumption that photocurrent competes directly with recombination predicts a mirror-image relationship between PL intensity and photocurrent as a function of voltage. Fig. 5 illustrates the goodness-of-fit obtained with a ZnO electrode.

In essence, the aforementioned argument is molecular in nature and analogous to a Stern-Volmer treatment of excited-state quenching (74). We recast the argument in molecular terms by treating photocurrent, nonradiative recombination and radiative recombination as the three pathways available for deactivation (75); their quantum yields, ϕ_x, ϕ_{nr}, and ϕ_r, respectively, thus sum to unity. At open circuit, all e^--h^+ pairs are forced to recombine with the ratio of radiative to nonradiative recombination dependent, in general, on such parameters as excitation wavelength and temperature. The effect of bringing the PEC into circuit is to permit some fraction of e^--h^+ pairs to separate rather than recombine; the e^--h^+ pairs which continue to recombine are treated as doing so subject to the open-circuit proportionality relation. The ratio of PL intensity at any two potentials, 1 and 2, can then be expressed by eq.[6]. Moreover, if the first potential is open circuit, eq. [7] obtains.

$$\frac{1-\phi_{x_1}}{1-\phi_{x_2}} = \frac{\phi_{r_1}}{\phi_{r_2}} \tag{6}$$

$$\frac{\phi_{r_o}}{\phi_r} = \frac{1}{1-\phi_x} \tag{7}$$

For conditions where ϕ_x reaches a maximum value of unity, eq. [7] predicts a mirror-image relationship between photocurrent and PL intensity as a function of applied potential.

We examined both n-CdS:Te- (46,47,75) and n-CdS$_x$Se$_{1-x}$-based PEC's (52,53) for agreement with eq. [7]. Table III presents data for the sulfoselenide electrodes culled from the iLV curves of Fig. 14. Reasonable agreement obtains between ϕ_x values calculated from PL quenching and values measured at saturation potentials ($\sim$-0.3 V vs. SCE). Similar accord was found for n-ZnO:Cu-based PEC's (76,77). In general, however, we found that the complete iLV curves do not obey eq. [7]. An exaggerated discrepancy was observed for an n-GaAs$_{0.6}$P$_{0.4}$-based PEC: photocurrent and hence ϕ_x were constant from -1.8 to -1.0 V vs. SCE, yet PL intensity declined by almost a factor of two over this potential regime (78). Similar effects at positive potentials were noted in the n-ZnO work and attributed to a deficiency of near-surface majority carriers under these conditions of substantial band bending. This rationale foreshadows the key role that carrier properties can play in photocurrent and PL, properties which are ignored in the molecular model. A broader framework for interpreting the relationship between photocurrent and PL quenching is provided in Section IIIC.

B. The Dead-Layer Model

Aspects of PL quenching have for some time been studied in semiconductor/metal Schottky barrier systems. In many of these solid-state studies, PL quenching has been analyzed using a dead-layer model (79-86). Originally formulated from cathodoluminescence studies (79), the essential feature of the model is that there exists a totally nonemissive zone of distance D from the surface into the bulk of the semiconductor. This zone is treated as being "dead" to luminescence.

The thickness of this nonemissive zone is correlated with the extent of the electric field into the semiconductor. Physically, e^--h^+ pairs formed within this electric field by optical excitation are swept apart more rapidly than the radiative decay rate. Hence, due to the effectively small density of carriers in this region, the probability for luminescence is very small. Expectations regarding PL quenching for the Schottky barrier are illustrated in Fig. 15. At flat-band potential, the radiative quantum efficiency, $\phi_{r_{FB}}$, should be proportional to the incident absorbed intensity, I_o; as an electric field is introduced by applied potential, PL will be proportional to $I_o \exp(-\alpha'D)$, the fraction of light absorbed beyond the dead layer. In this expression, $\alpha' = \alpha + \beta$ with α and β the absorptivities of the solid for the exciting and emitted light, respectively; β represents the correction for self-absorption of PL. A ratio of the in-circuit and flat-band PL efficiencies yields eq. [8]

$$\frac{\phi_r}{\phi_{r_{FB}}} = \exp(-\alpha'D) \qquad [8]$$

which can be used to calculate the dead-layer thickness from known absorptivities and measured PL quenching. A good test of the model is the acquisition of a consistent value of D from PL quenching data obtained for different optical penetration depths.

To our knowledge, the first report on the dead-layer thickness as a function of potential was by Hetrick and Yeung in 1971 (80,87). They reported on the intensity of the edge emission from n-type CdS as a function of applied bias for the case of a Au/CdS Schottky barrier diode. They found that variations in the PL intensity could be well acounted for by using an expression with the functional form $\exp(-\alpha W)$. Therefore, they equated the thickness of the dead layer

with that of the depletion width, W, and demonstrated that their functional

dependence on voltage, equation [2], was identical for the system examined.

The next system studied was that of n-GaAs Schottky barrier diodes by

Langmann in 1974 (81). He studied the PL intensity-voltage behavior for the

case of reverse bias and observed a dead-layer thickness of width equal to

that of the depletion width determined by capacitive measurements. He pointed

out that this method was useful for measuring absorption coefficients of the

semiconductor for excitation wavelengths well above the absorption edge; only

the carrier concentration of the semiconductor need be known. Due to the

high value of α above the absorption edge, these quantities are difficult to

acquire by normal transmission measurements, since very thin samples are required.

A key paper was published by Mettler in 1977 (88). He studied the PL

intensity of GaAs samples as a function of excitation wavelength and therefore

penetration depth of the incident light. The intent of this work was to

extend the simple dead-layer model to include the effect of surface recombination

on the PL intensity and to point out how one could separate near-surface

properties from bulk properties. An important expression that he arrived at

is given here for the PL intensity, I_L:

$$I_L \approx K(1-R_e)N \exp(-\alpha W) \left[\frac{1}{\alpha L_p} + \frac{1}{S_{rv}} \right] \tag{9}$$

K is a constant which depends upon the internal quantum efficiency and

geometrical factors; R_e is the reflectivity of the sample for the incident

wavelength, N is the number of incident photons; and S_{rv} is the reduced

surface recombination velocity, i.e., $S_{rv} = S_v(\tau_p/L_p)$ where S_v is the

surface recombination velocity , τ_p is the lifetime of the minority carrier,

and Lp is its diffusion length.

In 1978, Volodina and co-workers examined the PL intensity-voltage behavior of Ni/GaAs Schottky barrier diodes for both forward and reverse bias (82). They observed a decrease in the luminescence in the forward bias region, contrary to the expectations of the dead-layer model; one excitation wavelength and one carrier concentration of n-GaAs was used in these experiments. The conclusion reached from these studies was that the surface recombination velocity was increasing in the forward bias regime and that this factor was more significant in affecting the luminescence than the diminution of the depletion width with forward bias.

Ando and co-workers have more recently reported on the PL behavior of n-InP and n-ZnSe Schottky barrier diodes and n-InP metal-insulator-semiconductor (MIS) diodes (83-85). They found a good correlation with the dead-layer model for both types of structures for the situation in which a depletion region exists in the semiconductor. For the metal-semiconductor (MS) diodes the maximum PL intensity occurred at the flat-band potential. For an MIS diode an accumulation layer can be formed with sufficient forward bias. In this case, the authors observed a large increase in PL intensity compared to that at flat-band. They proposed a model which involved the concentration of excess surface carriers to explain the results.

Hollingsworth and Sites have provided the most recent results on the dead-layer model applied to a solid-state system (86). They examined p-type InP Schottky diodes using eq. [8]. They did not equate the thickness of D with that of W (as measured by capacitance). Rather, they showed that D and W have the same functional dependence on voltage. Consistent values of D were found at any given potential while using several different excitation wavelengths corresponding to several values of α.

In summary, then, there is ample evidence from the solid-state literature that field-induced quenching can be explained using a dead-layer model. An important caveat which has emerged from these studies is that surface recombination velocity can also substantially influence PL quenching properties.

C. Applications of the Dead-Layer Model to PEC's

Availability of good-quality, single-crystal material with a wide range of carrier concentrations and known ultraband gap absorptivities made n-GaAs a logical choice for evaluating the dead-layer model in PEC's. We examined PL quenching from samples having carrier concentrations of $\sim 10^{16}$-10^{19} cm^{-3} in PEC's employing stabilizing ditelluride electrolyte (89). Edge emission with $\lambda_{max} \sim 870$ nm, corresponding to $E_g \sim 1.42$ eV, was observed in these experiments. Excitation was delivered by three laser wavelengths -457.9, 514.5 and 632.8nm - for which GaAs α values are ~ 1.6, 0.91 and 0.44x10^5 cm^{-1} (88,90). As was noted with the other electrodes examined, no change in PL spectral distribution was found between open circuit (~ -1.4 to -1.7 V vs. SCE) and potentials slightly positive of short circuit (~ -1.0 V vs. SCE), permitting PL to be monitored solely at λ_{max}. In describing PL properties we will use fractional quenching, ϕ_{xr}, for comparisons,

$$\phi_{xr} = 1 - \frac{\phi_r}{\phi_{r_{FB}}} \qquad [10]$$

where ϕ_{xr} is given by eq. [10] and represents quenching between the flatband potential (approximated as open circuit) and an in-circuit potential.

Qualitative observations regarding PL quenching are presented in Figs. 16 and 17. The former demonstrates that for a given excitation wavelength, ϕ_{xr} varies inversely with carrier concentration, n. This trend is consistent with the dead-layer model in that D should shrink relative to the optical penetration depth as n increases. For a given value of n, Fig. 17 indicates that ϕ_{xr} varies inversely with excitation wavelength, reflecting greater fractional light absorption beyond D.

Also evident from Figs. 16 and 17 is the decoupling of maximum photo-
current yield, ϕ_x, from ϕ_{xr}: values of ϕ_x approach unity at short circuit
for all of the experimental conditions shown, yet ϕ_{xr} varies from ~10-90%.
The large values of ϕ_x reflect the substantial diffusion lengths
(~2 μm) of most of the materials used; only for the most highly-doped samples,
which likely possess smaller values of L_p (91), do we see ϕ_x values substantially
below unity. Short minority carrier diffusion lengths may account for the
crude correlation between ϕ_x and PL quenching observed with several II-VI
electrodes (vide supra; section IIIA) (87). For sufficiently small values of
Lp, the primary mechanism for current collection is by drift rather than diffusion:

only e^--h^+ pairs absorbed within the depletion region are effectively
separated so as to produce a net current. The premise of the dead-layer model,
it will be recalled, is that e^--h^+ pairs generated within roughly the depletion
width do not lead to luminescence. Therefore, the same fraction of incident
e^--h^+ pairs are both collected as current and prohibited from recombining for
luminescence. This then appears to be the basis on which one would expect
the relation $\phi_x = \phi_{xr}$ (eq. [7]) to hold. A further requirement is that all holes that
reach the semiconductor surface result in a net current via charge transfer
to a solution species, as opposed to nonradiative surface recombination. The
latter process, if operative, could effectively remove the holes and hence
ensure the quenching of the luminescence, yet the result would be no net
current. Hence, the relation $\phi_x = \phi_{xr}$ would break down under these
circumstances. For the system under consideration, it is likely that the
polychalcogenide redox couple ensures very fast interfacial kinetics, since
it is a very effective couple for the stabilization of many n-type photoanodes.

Quantitative features of these n-GaAs-based PEC's are summarized in
Table IV. The crucial observation is that for each sample examined, excitation
at three different wavelengths yields different degrees of fractional
quenching, yet substitution into eq. [8] produces a consistent value of D.
Moreover, this thickness is comparable to the value of W calculated from the
manufacturers' material specifications; roughly, D depends on $n^{-\frac{1}{2}}$, as expected
from the expression for W (eq. [2]).

Although the Table IV data only represent a single in-circuit potential
(-1.0 V vs. SCE), similar calculations of D can be made from measured ϕ_{xr}
values throughout the potential range of interest. Table V epitomizes such
an analysis. The table reveals that consistent values of D are obtained at
several potentials and that, as expected, D increases with applied potential.

The beauty of the dead-layer model as applied to PEC's is that, in
principle, it serves as a simple in situ technique for mapping the electric
field in the solid. As such, it might be used to determine how applied
potential is partitioned across the semiconductor-electrolyte interface.
Limiting cases illustrate this notion. For example, in PEC's conforming
to the "ideal" model, applied potential appears exclusively in the semiconductor
and PL intensity should exhibit its maximum dependence on this parameter;
at the other extreme, Fermi-level-pinned systems are characterized by
the appearance of potential exclusively in the Helmholtz region of the
electrolyte, and potential-independent PL intensity is expected. The extent
to which applied potential appears in the depletion and Helmholtz regions
and the influence of surface states on this distribution of potential has
been treated theoretically but has been difficult to measure experimentally
(15, 92,93). The technique used most extensively for analyzing interfacial
energetics has been capacitance.

The foregoing analysis prompted us to examine the applicability of PL to characterizing interfacial energetics by comparing experimental quenching curves for n-GaAs-based PEC's with curves calculated by assuming that all of the applied potential appears in the depletion region; similar comparisons have been made in solid-state systems (80-86). Assumptions made in calculating the quenching curves are: (1) the open-circuit potential is the flat-band potential; (2) D is proportional to W; and (3) surface-recombination velocity does not substantially influence our results. With respect to the last assumption, equation [9] related PL intensity to the width of the depletion region and to surface recombination velocity. An expression that gives the ratio of PL intensity at some bias to that at flat-band is given in equation [11]:

$$\frac{\phi_r}{\phi_{r_{FB}}} = \exp(-\alpha W) \frac{\left[\frac{1}{\alpha L} + \frac{1}{S_{rv}}\right]}{\left[\frac{1}{\alpha L} + \frac{1}{S_{rv_{FB}}}\right]} \qquad [11]$$

The quantities in eq. [11] have their previously defined meanings and $S_{rv_{FB}}$ is the reduced surface recombination velocity at flat-band ($S_{rv} = S_v \tau_p/L_p$). Equation [11] reduces to the form of the simple dead-layer expression (eq. [8]) if S_v is either relatively independent of potential or relatively large ($S_v \gg L_p/\tau_p$ and $\alpha L_p^2/\tau_p$). The surface recombination velocity for GaAs is known to be quite large (94,95).

Using these assumptions, PL quenching is calculated from eq [12], where C

$$\frac{\phi_r}{\phi_{r_{FB}}} = \exp[-\alpha'C(V-V_{FB})^{\frac{1}{2}}] \qquad [12]$$

is a constant such that $D = C(V-V_{FB})^{\frac{1}{2}}$. The value of C was calculated at -1.0 V vs. SCE using the experimental values of $(V-V_{FB})$ and D; D was calculated

by eq. [8] from the measured $\phi_r/\phi_{r_{FB}}$ value. In the potential regime near short circuit, the value of C appears to be relatively insensitive to modest changes in potential. The constant was then used to calculate $\dfrac{\phi_r}{\phi_{r_{FB}}}$ as a function of applied bias.

When the calculated and experimental PL intensity curves are arbitrarily matched at open circuit, they are very clearly nonsuperimposable, as shown in Fig. 18. The discrepancy demonstrates that the measured PL curve does not have a functional dependence of the form $\exp[-(V-V_{FB})^{1/2}]$. Specifically, with the assumptions given, all of the n-GaAs electrodes examined exhibit less quenching of their open-circuit PL intensities than is calculated on the basis of the expected expansion of the depletion width with potential.

A simple explanation for the discrepancy illustrated in Fig. 18 is that at potentials near open circuit, approximated here as the flatband potential, applied potential appears predominantly in the Helmholtz layer rather than in the semiconductor. In fact, the curves of Fig. 18 can be roughly matched using the dead-layer model by assuming that ~150 mV of the first 200 mV of potential applied to the electrode falls in the Helmholtz layer; beyond this point, additional anodic potential appears exclusively in the semiconductor. The partitioning of applied potential near flatband could reflect the presence of a large number of ionized surface states (92), a reasonable situation for GaAs under our experimental conditions (96). Potential applied to such electrodes is calculated to drop largely in the Helmholtz region until the Fermi level has reached a position where much of this surface charge no longer remains (92,97).

The PL intensity of the n-GaAs electrodes remains essentially constant at the open-circuit PL intensity as the potential is scanned ~100-200 mV negative of open circuit (87). A slight decline in PL intensity is usually observed at more negative potentials. These observations are consistent with the

aforementioned surface state mechanism, wherein applied potential drops predominantly in the Helmholtz layer at potentials near open circuit. This would prevent the formation of an accumulation region, which has previously been invoked as a factor in the greatly enhanced PL intensity (vide supra) observed at potentials negative of V_{FB} for the n-InP MIS Schottky diode (85). It is important to note that this invariance of PL intensity need not be associated with the flatband potential, but could, for example, result from a finite depletion width whose thickness is fixed or pinned by surface states. In such a case, the calculated dead-layer thickness (eq. [8]) corresponds to the difference in D which occurs between the two potentials of interest. The slight decline in PL intensity at potentials ∿100-200 mV more negative than open circuit is most likely due to an increase in the surface recombination velocity, possibly induced by reductive decomposition of the semiconductor surface.

While the partitioning of applied potential is an appealing rationale for the disparity in calculated and observed PL intensity curves of Fig. 18, this model masks kinetic features of the interface which are reflected in the interfacial energetics. We have mentioned, for example, the neglect of surface recombination velocity in the curve-fitting procedure. Equally significant is the rate of interfacial charge transfer. For the concentrated chalcogenide electrolytes and moderate light intensities used in our studies, charge-transfer is not rate-limiting. But it can be, and this is a key feature which distinguishes semiconductor-electrolyte from semiconductor-metal interfaces. Slow charge transfer in the potential regime near flat-band may result in the buildup of holes in the near-surface region. One consequence is that the capacitance of the semiconductor can increase in this regime such that applied potential may drop in the Helmholtz layer. Another consequence is a flattening of the bands due to the resultant countervoltage, as brought about by a mechanism similar to that which occurs in open-circuit photovoltage measurements (98).

The gratifying fit of PL intensity from n-GaAs electrodes to the dead-layer

model piqued our interest in determining how widely the model could be applied. We examined a single-crystal c-plate of n-CdSe in ditelluride electrolyte with 457.9-, 514.5-, and 626-nm excitation, and found good agreement with the model (87) using published absorptivities for CdSe (63). Unlike PL from GaAs, however, PL from CdSe increases dramatically at potentials cathodic of open circuit. The origin of this increase is most likely due to the formation of an accumulation region, as discussed by Ando and co-workers for the case of an n-InP MIS Schottky barrier diode (85). Greatly increasing the excess concentration of electrons in the near-surface region through the formation of an accumulation layer will lead to a rise in the recombination rate. Additionally, minority carriers will be repelled from the surface by the resultant electric field and hence be more likely to recombine radiatively as opposed to nonradiatively via surface recombination. The dramatic rise in PL intensity is therefore most likely indicative of the fact that applied potential negative of open circuit drops across the semiconductor, at least in part. This is in contrast with the GaAs system, where all of the applied potential appears to drop across the Helmholtz layer.

In related studies, Tomkiewicz, et al. reported agreement with the dead-layer model at potentials near and anodic of flatband for n-CdSe in polysulfide electrolyte using 514.5-nm excitation; modulated rather than steady-state PL was examined in this work (99). Not surprisingly, edge emission from n-$Cd_{0.95}Mn_{0.05}Se$ electrodes in diselenide electrolyte also appears to satisfy the dead-layer model at potentials anodic of open circuit (100).

In light of the above discussion, a particularly appealing electrode for PL studies is n-CdTe, which has been reported by Wrighton, et al. to exhibit Fermi-level-pinned or ideal behavior depending on whether an oxidizing or reducing etchant was used, respectively (101,102). The electrode properties were characterized by cyclic voltammetry conducted primarily in CH_3CN solution.

Fermi-level pinning was attributed to the presence of a thin Te-rich overlayer on the oxidized samples. Use of X-ray photoelectron spectroscopy (XPS) verified that elemental Te and some TeO_2 comprised this overlayer. The existence of this overlayer may well give rise to the presence of surface states in sufficient density that pinning will occur. Essentially, a stoichiometric surface composition was found by XPS for reduced samples; this surface composition was therefore correlated with the observation of ideal behavior.

PL results were obtained for n-CdTe electrodes in both aqueous and nonaqueous PEC's (87,103). The ditelluride electrolyte was the redox couple of choice for the aqueous PEC; the solubility of Te in this medium should minimize the ability of the element to pin the system. Presented in the top panel of Figure 19 are two PL intensity-V curves which were obtained using 514.5- and 620-nm excitation, respectively. Although CdTe absorptivities are not sufficiently well-established to permit a quantitative analysis, the PL quenching is greater for the shorter penetration depth light, as expected from the dead-layer model. Also to be noted is the presence of hysteresis in both curves at potentials within 100 mV of open circuit (∿-1.8 V vs. SCE). Hysteresis in the PL intensity-V curve is most likely an indication of changing surface chemistry. The surface recombination velocity may well be changing as a function of potential. Therefore, the dead layer model in its simplest form, as used for the n-GaAs system, must be used with caution in this case. Qualitatively, however, PL measurements indicate that the n-CdTe/ditelluride PEC is behaving in an unpinned manner.

The other electrolyte utilized in conjunction with n-CdTe was the ferrocene/ferricenium redox couple in acetonitrile. Two sets of iLV curves are shown in Figure 20. These were obtained on the same n-CdTe electrode which was treated with either a reducing etch ($OH^-/S_2O_4^{2-}$) or an oxidizing etch

($HNO_3/Cr_2O_7{}^{2-}$); excitation was with 514.5-nm light. Virtually negligible quenching is observed for the oxidized electrode ($\phi_{xr} \sim 0.04$), in contrast to that observed for the reduced electrode ($\phi_{xr} \sim 0.39$). The i-V behavior is also quite disparate. Values of ϕ_x at +0.1 V vs. Ag/Ag^+ were 0.45 and 0.04 for the reduced and oxidized electrode, respectively. Additionally, the i-V curve for the reduced electrode exhibits negligible hysteresis, as opposed to that for the oxidized electrode. Other excitation wavelengths were also used in these experiments. For the reduced n-CdTe electrodes, values of ϕ_{xr} of 0.53, 0.46, and 0.24 were obtained using 457.9-, 488.0-, and 620-nm excitation, respectively. Quenching remained negligible with the other excitation wavelengths for the oxidized electrode.

As discussed previously, the phenomenon of Fermi-level pinning is expected to give rise to potential-independent PL. This is based upon the central assumption of the simple dead-layer model, viz., only changes in the width of the space-charge layer affect the PL intensity. The extent of the electric field within the semiconductor is invariant to changes in applied potential for a pinned system. From this reasoning, it appears that the PL behavior observed for the oxidized n-CdTe electrode is indicative of a Fermi-level-pinned system. This assignment is consistent with the conclusions of Wrighton and co-workers (101). On the other hand, the reduced n-CdTe electrode exhibits behavior more akin to that expected for an "ideal" semiconductor. Just exactly how "ideal", however, is uncertain at this point and is still under investigation.

Although the studies described thus far have utilized edge emission, we have examined one PEC, constructed from an n-ZnSe:Al electrode and stabilizing diselenide or ditelluride electrolyte, for which subband gap PL was used for characterization (104). Figure 21 shows that n-ZnSe:Al electrodes display both a weak, sharp edge PL band at ~ 460 nm ($E_g \sim 2.7$ eV) and an intense, broad PL peak at ~ 600 nm.

The latter, assigned as self-activated (SA) PL, is believed to involve a deep level arising from a complex based on a Zn vacancy, V_{Zn}, and a next-neighbor donor impurity such as Al_{Zn} (Al on a Zn site)(105-108). A 77 K PL spectrum, also shown in Fig. 21, indicates that the 600-nm band is a composite of bands with λ_{max} ~630 and 550 nm. Assignments reported for similar spectra suggest that the 630-nm band is SA in origin and involves a neutral $(V_{Zn}Al_{Zn})$ or ionized defect $(V_{Zn}Al_{Zn}^-)$; the 550-nm band was ascribed to a defect involving Al and an alkali metal impurity (109). For convenience, we will refer to the 600-nm transition as a SA band, although its origin in our samples has not been fully established.

The remarkable feature of the SA PL is its efficiency. As shown in Table VI, we measure ϕ_r to be ~0.02-0.05 at several ultraband gap excitation wavelengths. A large ϕ_r value is also consistent with the modest doubling of ϕ_r observed when samples are cooled to 77 K, Fig. 21.

Prior to exploring PEC behavior, we investigated temporal features of the two PL bands. The edge PL band has a decay time of $\lesssim 7$ ns, its measurement limited by the duration of the N_2 laser pulse. A similar limitation was observed for the rise time of the SA PL and its initial decay. After the SA PL peak intensity had declined ~30%, however, a longer exponential decay was seen with a typical $\tau_{1/e}$ value of ~1 μs. Mechanistically, the different temporal properties of the two bands indicate that the corresponding excited states are not thermally equilibrated. As with CdS:Te, these data are consistent with population of the SA state via the state yielding edge PL or from a yet higher energy state; in the latter case, the strong lattice coupling characteristic of deep traps provides a relaxation mechanism for rapid population of the SA state in parallel with population of the state leading to edge PL. Either scheme for excited-state communication is also supported by steady-state measurements wherein the intensities of the edge and SA PL bands maintain a constant ratio over incident intensities spanning several orders of magnitude.

When used in a PEC, both PL bands of the n-ZnSe:Al electrodes are quenched

in parallel, consistent with a mechanistic scheme in which separation

of e^--h^+ pairs occurs prior to population of the SA state. The dead-layer model,

previously applied to PL from a Au/ZnSe Schottky diode (84), was used to

interpret quenching in the PEC. A difficulty encountered is that reliable

absorptivities are not available for the solid. However, if the dead-layer

model is assumed applicable, it provides a means for acquiring relative absorptivities

for ultraband gap wavelengths. By use of the dead-layer model, we determined

α at 405 and 366 nm using a reported value at 442 nm (84). As with n-GaAs-based

PEC's, we compared calculated and observed PL intensity curves and found

similar discrepancies in the region near open circuit, again interpretable in

terms of the partitioning of applied potential across the interface.

The effect of carrier concentration on PL quenching was also qualitatively

consistent with the dead-layer model. As was found in the solid-state study

(84), more resistive samples, prepared by heating ZnSe:Al in an evacuated ampule

with Se, exhibited greater PL quenching, as shown in Table VI. Larger ϕ_x values

were also observed for these treated samples; low ϕ_x values, Table VI, were

common for these electrodes and probably reflect small diffusive contributions

to photocurrent, Lp having been estimated as only $\sim10^2$ Å (110).

In concluding this section, it is worth noting that the influence of

surface properties on PL has been noted in at least three other studies.

Although not quantitative, effects of surface properties on PL intensity were

invoked in an early study of n-Ge electrodes in H_2SO_4 and $OH^-/Fe(CN)_6^{3-}$ electrolytes

(111,112) and, more recently, in studies of n-TiO$_2$ electrodes in H_2SO_4 electrolyte

(113) and of several III-V electrodes in HCl electrolyte (114). The effects of

surface states are expected to reveal themselves in a maximum in PL intensity-

potential plots: for an n-type material, intensity will decrease at the anodic

extreme due to a limited supply of conduction band electrons (depletion conditions)

and at the cathodic extreme due to high surface recombination rates owing to the

large surface concentration of conduction band electrons (accumulation conditions).

The study with n-TiO_2 was particularly interesting (113). Subband gap PL at 1.47 eV ($E_g \sim 3.0$ eV) was found and attributed to an ·OH surface adduct designated $X_{1.47}$. This species was thought to be an intermediate in the oxidation of H_2O which occurs at the irradiated electrode. That the PL band is surface-localized is supported by its growth from illumination at anodic bias and its quenchability by reductants such as halide ions and hydroquinone; these species also suppress O_2 evolution at the irradiated electrode. EL studies, described in the next section, also supported the assignment.

In summary, then, the dead-layer model provides a simple conceptual framework with which PL properties of semiconductor electrodes can be used to study the electric field within the solid. Although our results suggest that this model may be used to examine kinetic and energetic features of the semi-conductor-electrolyte interface, such as the manner in which applied potential is partitioned across the interface, uncertainties in surface properties presently limit the information which can be derived from PL quenching data. In principle, the surface recombination velocity can be extracted from plots of PL intensity as a function of optical penetration depth, as formulated by Mettler (88); an analysis of PL properties presented by Stephens (115) permits extraction of S_{rv} as well as minority carrier transport properties in the limit of an infinitesimal dead-layer thickness. Determination of S_{rv} as a function of potential should greatly increase the mechanistic information available from PL measurements.

IV. GENERAL EL PROPERTIES

A. Background

As described in the Introduction, EL complements PL as a tool for characterizing excited-state processes by providing an alternate mode of excited-state population. Extensively studied in solid-state systems, EL has

been exploited in the design of display devices. Although far less work has been conducted with liquid junctions, there is evidence that the injection and impact excitation mechanisms identified for EL in solid-state systems are also applicable to wet systems.

Before discussing liquid-junction effects, a brief overview of solid-state systems is appropriate. As summarized in several excellent reviews (19,31-33), p-n junctions at forward bias can be very efficient structures for injection of minority carriers and are the key component of light emitting diodes (LED's). More relevant to liquid-junction systems is the production of EL from Schottky barriers (32). For a metal-semiconductor (MS) structure, surface states can induce an inversion layer wherein the surface has a conductivity type opposite to that of the bulk material (a p-type surface on bulk n-type material, e.g.). Under forward bias, the bands flatten, resulting in the injection of minority carriers into the bulk where recombination leads to emission. Another strategy for introducing surface charges for production of EL is to use a metal-insulator-semiconductor (MIS) structure (32). The MIS structure permits band bending to be controlled by applied potential; changes in potential alternately produce an inversion layer and band flattening to inject the accumulated minority carriers.

Production of EL is not restricted to injection processes driven by forward bias. Another EL mechanism is based on impact excitation wherein a large electric field in the semiconductor can impart sufficient kinetic energy to electrons to excite by impact other electrons from the valence band (kinetic energy on the order of E_g) or from impurities (32). Successive collisions multiply the number of free electrons. If both electrons and holes are involved in this process, it is termed "avalanche" breakdown. The necessary electric fields for electron acceleration ($\sim 10^5$-10^6 V/cm) can occur in the depletion region of reverse-biased MS contacts and in high ohmic

surface layers of forward-biased MIS structures (33). EL spectra generated by impact processes can extend to energies exceeding E_g owing to radiative recombination of hot carriers (32).

B. EL from Reverse-Biased Electrodes

Relatively few studies of EL have been made using reverse-biased electrodes. An early investigation of an n-ZnS:Cu electrode in an oleum (H_2SO_4 plus 30% excess SO_3) electrolyte was conducted at a reverse bias of 190 V (116). The white light observed was attributed to avalanche radiation resulting from the presence of an inversion layer.

Anodic breakdown of n-ZnO electrodes was accompanied by EL (117). Beyond $\sim$2.5 V vs. SCE in 5M KOH electrolyte, edge emission (λ_{max} $\sim$380 nm) was observed. The mechanism proposed involved Zener tunneling (electron tunneling from the valence band to the conduction band) with the electrons needed for recombination provided by solution species capable of injecting electrons into the conduction band. Support for this mechanism was provided by the increase in EL intensity accompanying addition of current-doubling substances to the electrolyte. The current-doubling species were two-electron oxidants such as HCHO: after oxidation by a valence band hole, the oxidized intermediate is energetically capable of injecting an electron into the conduction band. An alternate mechanism to Zener tunneling involving impact ionization was considered but thought unlikely due to the moderate applied potentials employed and low electron concentration at the semiconductor surface.

More recently, EL has been reported for n-type metal oxide semiconductors at strong anodic polarization in aqueous electrolytes (118,119). For n-TiO$_2$, e.g., at 10 V vs. SCE, a broad EL band (λ_{max} $\sim$630 nm) is produced with an efficiency of $\sim$10^{-3} to 10^{-4}. This subband gap EL was ascribed to radiative

transitions involving intraband gap surface states: Zener tunneling was proposed to create valence band holes at the surface which could radiatively recombine with electrons in surface states; oxidation of OH^- to O_2 was also thought to be mediated by these states. Extension of the study to n-$SrTiO_3$ and n-WO_3 revealed analogous subband gap EL which was used to construct maps of the surface state distributions. Maxima of these distributions were found to coincide with the electrolyte OH^-/O_2 redox level, if recombination were assumed to involve holes at the top of the valence band. The authors suggest that this coincidence in energetics supports the notion that mediation of redox chemistry occurs through the surface states involved in the emissive transitions.

Samples of n-ZnSe:I displayed EL at anodic potentials exceeding ~ 6 V vs. Hg/Hg_2SO_4 in aqueous electrolytes (120). Self-activated (SA) emission character-istic of ZnSe is observed with $\lambda_{max} \sim 2.0$ eV. The mechanism proposed in an alkaline medium is electron tunneling from adsorbed OH^- into the conduction band followed by field acceleration in the space-charge region. Once accelerated, the electrons have enough energy to impact ionize acceptor centers formed by a Zn vacancy and iodine donor atom; emission then accompanies the recombination of conduction band electrons in these centers. In addition to the SA band, emission at ~ 2.2 eV could be observed at anodic potentials in acidic solutions containing Cu^{+2} ions; this band, observed after an initial reduction of Cu^{+2} ions to adsorbed Cu^0, matched a band found for solid-state Cu-doped ZnSe diodes.

A novel mechanism for EL production, ion injection into a semiconductor surface, has been reported for p-GaP electrodes (121). When reverse-biased to ~ -10 V vs. SCE, a broad emission from ~ 1.0 to 2.8 eV is found; since E_g is ~ 2.2 eV, a substantial portion of the emitted light occurs at energies exceeding E_g. An intriguing feature of the EL is its dependence on electrolyte composition: independent of anion, the emission is only found with cations

of ionic radius ≤ 0.75 Å, in good accord with GaP crystal channel size. The proposed mechanism for EL is that hot electrons created by Zener tunneling reach the surface and radiatively fill empty states created by cation injection. Evidence for ion injection was provided by elastic-recoil detection experiments which detected Li^+ ions to depths of ≥ 0.5 μm at concentrations of $\sim 10^{20}$ cm^{-3}.

C. EL from Forward-Biased Electrodes

The majority of studies involving EL from semiconductor electrodes have used forward-biased n-type material in oxidizing electrolytes. Under these conditions, holes can be injected into the solids, leading to emission upon recombination with majority carriers. Because h^+ injection is initiated at the semiconductor-electrolyte interface, it is a promising technique for characterizing this region and the near-surface zone of the semiconductor. This is a recurrent theme of much of the reported research. Comparisons with PL, generally dominated by bulk semiconductor properties, make EL a powerful complementary tool for probing spatial features of electronic structure and excited-state deactivation processes in semiconductor electrodes. EL is also useful for examining mechanistic features of interfacial charge-transfer processes.

An early study of EL was made with n-Ge electrodes used for the reduction of H^+ and $Fe(CN)_6^{3-}$ ions (111). Near-ir edge emission (~ 0.7 eV) was observed, and h^+ injection into the valence band was independently demonstrated using a p-n junction, as shown in Fig. 22. The technique illustrated, the "thin-slice method", uses two circuits to partition the total current between the conduction and valence bands for solids with appreciable m′... ity carrier diffusion lengths and the ability to form p-n junctions: in addition to the normal electrochemical circuit, the p-n junction can be reverse-biased in a separate circuit to collect

by diffusion minority carriers which have been injected from the electrolyte; this second circuit thus serves as a measure of minority carrier current (122-125).

Subband gap EL was reported for n-GaP electrodes when they were used to reduce aqueous $Fe(CN)_6^{3-}$ or Fe^{3+} ions (34,126). Emission bands at $\sim$1.2 and 1.6 eV were found (direct band gap energy $\sim$2.25 eV) with the former observed in PL and attributed to recombination through a bulk intraband gap state. The 1.6-eV band was attributed to surface-state-mediated recombination. Besides the absence of the band in PL spectra, photoaction spectra of p-GaP electrodes in oxidizing electrolytes exhibited a weak peak at $\sim$1.6 eV.

The electrolyte which has dominated EL studies is an aqueous alkaline solution containing peroxydisulfate, $S_2O_8^{2-}$, ions. Memming showed that $S_2O_8^{2-}$ is reduced in two steps with normal potentials estimated to be $\leq$ +0.6 and $\geq$ +3.4 V vs. NHE, respectively (127). For appropriate n-type semiconductor electrodes, reduction could be anticipated by the mechanism pictured in Fig. 23. To initiate the reaction, a conduction band electron reduces $S_2O_8^{2-}$ to SO_4^{-} and SO_4^{2-} at potentials negative of flat band where the electrode serves as a dark cathode. The sulfate radical anion which is generated is a sufficiently strong oxidant that it can then inject a hole into the valence band of many semiconductors. Accompanying this completion of the reduction to SO_4^{2-}, conduction band electrons recombine with the injected holes to yield EL. The observation of EL from n-GaP electrodes (and many other n-type semiconductors) in $OH^{-}/S_2O_8^{2-}$ electrolyte provides strong evidence for this current-doubling mechanism. Similar arguments were made for H_2O_2 with estimates of first and second reduction potentials being $\leq$ 0.6 V and $\geq$ 2.9 V vs. NHE. The same n-GaP EL spectral distribution was found with H_2O_2 as with $S_2O_8^{2-}$.

Besides these inorganic current-doubling reagents, quinones were also found to induce EL from n-GaP electrodes used as dark cathodes (123). Complementary demonstrations of the effect, revealed in enhanced photocurrents at p-GaP

electrodes in the presence of quinone (analogous to the n-ZnO/HCHO system, vide supra), were pH dependent, reflecting the involvement of acid-base equilibria in the mechanistic scheme. Studies with n-Ge using the "thin-slice method" demonstrated valence band involvement in current flow and the importance of surface properties on mechanism: with anodic prepolarization, the reduction of benzoquinone proceeded via both energy bands, whereas with cathodic prepolarization exclusively valence band current was found. Photocurrents examined with p-Si/quinone systems paralleled results with p-GaP and indicated a current-doubling mechanism for this system, as well.

An extensive study of EL was reported by Gerischer, et al. for several n-type semiconductors (SnO_2, ZnO, CdS, GaP, and GaAs) in aqueous media containing O_2, H_2O_2, or $Na_2S_2O_8$ as oxidants (128). Reduction currents could generally be observed for the three oxidants with onsets at potentials near and negative of flat band. Observation of EL required potentials negative of the onset of reduction current. Evidence that metal films formed during reduction (e.g., Zn on ZnO) prompted use of a pulse technique ($\sim$0.5-msec pulses) to minimize such surface reduction. Temporal measurements of EL intensity, spectral distributions, and EL quantum yields were determined for these systems. In time-resolved measurements, maximum EL intensity was observed $\sim$0.1 msec after the reduction current began; declines in EL intensity at later time (up to $\sim$0.6 msec after pulse initiation) were attributed to a diminished surface $S_2O_8^{2-}$ concentration (0.1 N solutions) and possible generation of nonradiative recombination sites on the electrode surface. EL transients for the n-ZnO/$S_2O_8^{2-}$ system have recently been examined in more detail (129). With regard to spectral distribution, ZnO, CdS, GaP, and GaAs all exhibited subband gap emission ascribable to surface-state-mediated recombination. Strong edge emission was observed for ZnO. The spectral distributions were dependent on applied potential with increasingly negative bias generally increasing the intensity of edge emission relative to subband gap EL. Quantum yields at various potentials were determined by estimating total emitted light

and the hole injection current. Efficiencies increased with cathodic bias, reaching maximum values of $\sim 10^{-4}$ (GaAs). For a given electrode, efficiency generally increased by orders of magnitude in passing from O_2 to H_2O_2 to $Na_2S_2O_8$. Energetics of h^+ injection were examined using band edge positions and potentials associated with the reduction of SO_4^-, $OH\cdot$, and O_2.

Several of these systems have also been examined by Tsubomura, et al. EL from n-GaP in $Fe(CN)_6^{3-/4-}$ and $S_2O_8^{2-}$ electrolytes has been the subject of a series of papers (130-133). The EL spectrum is dominated by a band at ~ 1.6 eV of surface origin; a bulk band, identified as such from PL spectra, was also observed at ~ 1.4 eV. Although the position of the 1.6 eV band was insensitive to the choice of oxidant, pH, electrode potential and crystal face ((111)Ga face or ($\overline{111}$)P face), the band's intensity was influenced by these factors. These effects and the band's assignment were discussed in terms of "surface-trapped holes", electron-deficient Ga-P surface bonds: establishment of an electron-transfer equilibrium was proposed between the solution redox couple and an electrode distribution of surface states. From the energetics of the n-GaP/$Fe(CN)_6^{3-/4-}$ system, the authors concluded that the 1.6 eV band arises from recombination of a conduction band electron with the "surface trapped hole". Additional evidence for this interpretation was offered from EL studies of n-CdS and n-ZnO in these same electrolytes: Comparisons of PL and EL were used to identify bands originating from the near-surface region which, in turn, were used to locate a distribution of surface states relative to the band edges (133). The resulting distribution of surface-trapped holes roughly corresponded to a range of solution redox couples with which the n-type semiconductors passed from photostability to efficient photoanodic decomposition.

The notion that EL reflects the existence of surface-trapped holes which might be precursors to photoanodic reactions was extended to reaction intermediates in studies with n-TiO$_2$ (113). In particular, EL spectra obtained with aqueous

solutions of H_2O_2 are dominated by a band at ~ 1.47 eV which is proposed to arise from a surface species produced by reaction of $OH\cdot$ (the one-electron H_2O_2 reduction intermediate) with the electrode surface, i.e,, a radical surface adduct. Recall that this species, $X_{1.47}$, was postulated to account for a PL band found at the same energy which appeared to be surface-localized, since its appearance required illumination at anodic bias (vide supra, Section IIIC). Support for the assignment also comes from the following experiment: irradiation of the electrode at 0.0 V vs. SCE in 1 N NaOH followed by a potential jump in the dark to -0.8 V vs. SCE yielded a burst of emission at 1.47 eV. Results of such experiments were interpreted as being consistent with accumulation of a radical surface adduct having a lifetime of ~ 1 h; such a species can radiatively recombine with conduction band electrons at forward bias to yield 1.47-eV emission. The authors suggest that $X_{1.47}$ or a species related to it is a rate-determining intermediate in the photooxidation of water at $n-TiO_2$ electrodes. In this context another experiment of interest is EL generation from $S_2O_8^{2-}$ electrolytes. Tsubomura, et al. observed much weaker emission with $S_2O_8^{2-}$ than with H_2O_2 and saw a different spectrum: the 1.47-eV band was only observed in some samples (especially with those previously irradiated at anodic bias) with the spectrum typically displaying unassigned bands at 1.9 and 2.2 eV. EL in the 1.2-1.5-eV region from $n-TiO_2/S_2O_8^{2-}$ along with edge emission was observed by Bard, et al. who also conducted some temporal studies of its intensity (134). EL from $n-SrTiO_3/S_2O_8^{2-}$ has been reported over a spectral range of $\sim 1.0-3.0$ eV ($E_g \sim 3.2$ eV) (135).

O. r EL studies have focused on the II-VI materials whose PL properties we examined, viz., $n-CdS:Te$, $n-CdS_xSe_{1-x}$ ($0 \leq X \leq 1$), and $n-ZnSe:Al$ (52-54,71,104,136). All of these studies were conducted with $OH^-/S_2O_8^{2-}$ electrolyte using a pulse technique to minimize electrode reduction and to maximize EL intensity. The EL cell was placed in the sample compartment of the emission spectrometer. By continuously pulsing the electrode while the emission monochromator was scanned, a series of spikes constituting the EL spectrum was generated. In cases where EL

intensity was bright enough to acquire steady-state EL spectra, a good match with pulse-generated spectra was found.

In general, a reduction current for $S_2O_8^{2-}$ at Cd chalcogenide electrodes could be observed at potentials cathodic of ~-0.8 V vs. SCE; the onset of EL was typically ~-0.9 to -1.2 V vs. SCE. These potentials are in the neighborhood of flat-band potentials for the solids. For several samples (100 ppm CdSe:Te; $CdS_{0.49}Se_{0.51}$; CdSe), prolonged experiments conducted with pulse potentials yielding intense EL (-1.5 or -1.8 V vs. SCE) resulted in minimal sample weight loss. We inferred from this that if reduction to Cd occurred at the electrode surface, subsequent deposition of the metal could arise from reduction of Cd^{+2} species formed during the anodic portion of the pulsing cycle. Electrode surface chemistry of these solids appears to be complex. It has also been studied by other techniques such as photoacoustic spectroscopy and reflectivity (137,138).

Our initial EL studies were conducted with CdS:Te samples for which we were interested in evaluating the role of intraband gap Te states (136). We found both edge emission (λ_{max} $\sim$510 nm) and broad Te-based emission (λ_{max} $\sim$600 nm) with 100-ppm,CdS:Te single-crystal samples. Fig. 24 illustrates these features as well as a good PL-EL spectral match. With a 1000-ppm,CdS:Te electrode, the EL spectrum still exhibits an edge band, but its intensity is dwarfed by a band at $\sim$620 nm. The latter is likely a composite of 600 and 730-nm bands arising from excitons trapped at a single Te site and nearest neighbor Te sites, respectively (vide supra,Section IIB). EL spectral distributions were relatively insensitive to the cathodic initiation potential employed, but the onset of edge emission is somewhat more negative than that for Te-based emission.

To evaluate EL efficiency we adapted measures from electrogenerated chemiluminescence (ecl) (139-141). Steady-state, instantaneous EL efficiency, ϕ_{EL}, is given by eq. [13] and determined by sitting at a given potential;

$$\phi_{EL} = \frac{\text{emitted light (ein/s) x F}}{\text{current due to h}^+ \text{ injection}} \qquad [13]$$

integrated EL efficiency, $\overline{\phi}_{EL}$, is given by eq. [14] and determined in pulse

$$\overline{\phi}_{EL} = \frac{\text{total emitted light (ein) x F}}{\text{total coulombs due to h}^+ \text{ injection}} \qquad [14]$$

experiments. In both expressions, F is Faraday's constant. Numerators of the equations were obtained by placing a flat-response radiometer next to the exposed electrode surface. Either power in μW for the steady-state experiment (eq. [13]) or integrated energy in μJ for a single-pulse experiment (eq. [14]) was measured. These values were converted to ein/s or ein, respectively, using either the maximum of the emissive spectral distribution for a sharp band or band extrema for a broad band so as to bracket the value. Since not all of the emitted photons are collected, these are lower-limit numerator values. To acquire values for the denominators of eq. [13] and [14], we used total current and coulombs, even though this likely overestimates the magnitude. For example, if the current-doubling mechanism for $S_2O_8^{2-}$ reduction is correct, this procedure overestimates the denominator by a factor of 2. Moreover, some of the current is due to H_2O reduction, although this is typically $\leq 5\%$. We adopted this conservative procedure because of the ambiguities in the EL generation mechanism. A consequence of this treatment is that EL efficiencies are lower limits. For samples with common EL and PL bands, a comparison of ϕ_{EL} or $\overline{\phi}_{EL}$ with ϕ_r is worthwhile because it provides insight into the efficiency with which the common emissive excited state is populated in an EL experiment.

In particular, by analogy with ecl studies, ϕ_{EL} or $\overline{\phi}_{EL}$ can be factored into an efficiency for excited-state population, ϕ_{ES} (excited states populated per hole injected), and the radiative efficiency ϕ_r, definable in this context as photons emitted per excited state populated. Estimates of ϕ_r and $\overline{\phi}_{EL}$ can be made under similar conditions to improve the validity of the comparison (52). For CdS:Te electrodes ϕ_{EL} was estimated to be $\sim 10^{-5}$. With ϕ_r values in air ranging from $\sim 10^{-4}$ to 10^{-2}, ϕ_{ES} could not be accurately determined but appears to be at least an order of magnitude less than 1. More precise comparisons of ϕ_r and ϕ_{EL} were obtained with CdS_XSe_{1-X} samples.

The family of solids formed from CdS and CdSe exhibited interesting EL properties both with regard to spectral distribution and efficiency (52-54). In the former case, the samples generally mimicked their PL counterparts in yielding a spectrum dominated by edge emission with a common λ_{max} value. At high resolution, however, the spectrum generally displayed a mismatch, as illustrated for n-CdSe in Fig. 25. As was observed in the excitation wavelength dependence of PL spectra, the mismatch is almost exclusively in the high-energy tail of the edge band and is indicative of self-absorption effects. A qualitative interpretation of the broader EL band is that it supports the idea that EL originates, on average, nearer the semiconductor-electrolyte interface than PL. Other spectral differences are that for some CdS_XSe_{1-X} samples, particularly those that were sulfur-rich, weak subband gap emission was observed in the EL but not the PL spectrum, indicative of intraband gap surface states.

The PL and EL from electrodeposited, polycrystalline, thin film CdSe electrodes have been examined (142). Both spectra exhibited 720-nm edge emission and a band at 1060 nm, but an additional peak at 945 nm was seen only in EL. PEC etching of these samples had little effect on PL or on the subband gap EL; however, the process enhanced the EL edge band intensity, providing a probe of changes in surface recombination properties.

Studies of EL polarization have also been conducted for n-CdSe $\underline{a}$-plate electrodes to complement the PL studies discussed earlier (71). Essentially similar results are obtained to those shown in Figure 12. Apparently, excited-state population of the split valence band proceeds in a similar manner with the two modes of excited-state population.

With regard to EL efficiency, values of $\overline{\phi}_{EL}$ for the CdS_XSe_{1-X} electrodes were determined for comparison with ϕ_r data taken under similar experimental conditions (values for $\overline{\phi}_{EL}$ were generally similar (52), but $\overline{\phi}_{EL}$ was easier to measure at the most positive potentials). Table VII presents a compilation of $\overline{\phi}_{EL}$ values taken near the onset of EL and at -1.5 V vs. SCE where maximum values typically obtain. At the latter potential, $\overline{\phi}_{EL}$ ranges from $\sim 10^{-5}$ to in excess of 10^{-4} with the samples of largest Se content consistently giving the largest EL efficiency. At the onset potential, $\overline{\phi}_{EL}$ only drops by factors of $\sim 2-8$. Since typical ϕ_r values are $\sim 10^{-4}$ to 10^{-3} at -1.5 V, ϕ_{ES} appears to be substantial and could approach unity for these systems. This comparison needs to be qualified by the different spatial zones involved in the PL and EL experiments, since the regions may have different average ϕ_r values. Additionally, there are substantial uncertainties in both ϕ_r and $\overline{\phi}_{EL}$. Nevertheless, the near agreement is enticing in that it suggests that EL efficiency might be able to rival PL efficiency in liquid-junction systems.

A disappointment in this regard is the $n-ZnSe:Al/S_2O_8^{2-}$ system for which ϕ_r was measured to range from $\sim 10^{-2}$ to 10^{-1} (vide supra, Section IIIC) (105). Although the EL spectrum mimicks the PL spectrum, the SA band has integrated EL efficiencies of only $\sim 10^{-6}$ (-1.8 V; near the EL onset potential) to 10^{-4} (-2.2 V vs. SCE) or two to four orders of magnitude below the radiative efficiency. Whether this reflects an anomalously low ϕ_{ES} value or grossly different ϕ_r values for the two regions of the solid involved in EL and PL remains to be determined.

That relatively efficient EL from a II-VI electrode can be obtained has been demonstrated by Bard, et al. with n-ZnS:Al ([143]). A value for $\overline{\phi}_{EL}$ of $\sim 2 \times 10^{-3}$ was measured at a current density of 25 mA/cm^2; efficiency was measured with an integrating sphere photometric detection system. The n-ZnS:Al system was

studied in considerable detail and revealed several interesting properties. EL was initiated at potentials near or negative of flatband (~-1.7 V vs. SCE at pH 1) using $S_2O_8^{2-}$ or H_2O_2 as oxidants; a h^+-injection mechanism was evidenced by the absence of EL in supporting electrolyte even at -10 V vs SCE. For the $S_2O_8^{2-}$ electrolyte, i was proportional to $(V-V_{fb})^2$ at potentials well negative of flatband (V_{fb}), consistent with a current-doubling mechanism; the EL intensity varied linearly as i^2. The blue emitted light (λ_{max} $\sim$460 nm or 2.7 eV) occurs at subband gap energies, E_g being $\sim$3.66 eV. Interestingly, the maximum and breadth of the EL band as well as its integrated intensity were sensitive to the cathodic potential employed, electrolyte pH, and the electrode history. In the latter case, temporal studies were used to demonstrate changes in EL properties as a function of pulse number. Illustrative of the effect were a 100-fold increase in integrated EL intensity between the first and 26th pulse (0 to -2.25 V vs SCE at 100 Hz; pH 8.9, $S_2O_8^{2-}$ electrolyte) accompanied by a 20-nm blue shift in λ_{max}. Stability of EL was also investigated in pH 8, $S_2O_8^{2-}$ electrolyte where <1% electrode weight loss was found after 11 days of continuous pulsing; since $S_2O_8^{2-}$ is a sacrificial reagent, it was added at intervals throughout the experiment. The ZnS:Al results were interpreted using a model based on tunneling between donor and acceptor intraband gap states. For this model, the rate-determining step for radiative recombination is the tunneling-mediated electron transfer between the occupied upper states and empty lower states, a mechanism which, for a current-doubling oxidant, would lead to the observed proportionality of EL intensity to the square of the current. The substantial EL efficiency of this system in the blue portion of the spectrum was noted earlier with a value of $\sim10^{-2}$ for n-ZnS/H_2O_2 (144). This system is clearly quite efficient for a liquid-junction construction.

EL from n-type III-V electrodes has continued to attract interest. Samples of n-GaAs have been the subject of at least four studies. An initial obs⁻rv⁻tion of edge EL ($\sim$1.43 eV) with passage of cathodic current in 1M H_2SO_4 electrolyte led to the conclusion that h^+ injection was the dominant contributor to the current (145). This H_2 evolution reaction was re-investigated using n- and p-type GaAs electrodes from which it was concluded that h^+ injection into the valence band of n-GaAs contributes $<$ 1% of the current corresponding to H_2 evolution (146).

An extensive study of EL from n-GaAs electrodes has been reported using a rotating ring-disk electrode (RRDE) system (147). EL can be used to distinguish between currents derived from capture of conduction band electrons and injection of valence band holes. With n-GaAs disk and Pt ring electrodes, electrochemistry was correlated with EL properties (monitoring emission with $\lambda <$ 860 nm) as a function of electrode potential, mass transport, and electrolyte pH. Holes were found to be injected into the valence band from Ce^{4+} ions at a diffusion-limited rate independent of electrode potential (the $Ce^{4+/3+}$ couple is well below the valence band edge). At anodic potentials, the injected holes cause anodic dissolution; minimal EL is found owing to the presence of a depletion region. With increasingly cathodic potentials, the dissolution is suppressed and EL increases with bias until changes in surface properties occur. A point emphasized from these results is that h^+ injection persists even with large surface electron concentrations and even though capture of conduction band electrons has a greater thermodynamic driving force. EL can also be observed with $Fe(CN)_6^{3-}$ at pH 12 where the (pH-dependent) valence band edge is estimated to lie above the $Fe(CN)_6^{3-/4-}$ redox potential. Much weaker EL obtains with Fe^{3+} in acidic solution where the redox potential is above the valence band edge. Surface chemistry such as oxide formation appears to be a general complicating feature of these systems, but the RRDE and EL

techniques appear to be powerful tools with which to probe it. The maximum

measured EL efficiency was $\sim 10^{-7}$ with the n-GaAs electrode.

These GaAs-based systems were subsequently re-examined so as to character-

ize both edge and subband gap EL as well as corresponding PL spectra; the

subband gap transition at ~ 1100 nm was attributed to Ga vacancies in the

lattice (148). Both emissive bands could be observed in PL and EL spectra of

melt-grown samples. Evidence that EL is produced nearer the surface, on

average, than PL came from a direct comparison of the spectra which revealed

a mismatch consistent with self-absorption effects. Interestingly, the

relative intensities of the two bands in PL and EL spectra were different

with the difference dependent on electrolyte; several possible explanations

for this effect related to (near-)surface electrode properties were proposed.

From EL measurements employing $Fe(CN)_6^{3-}$, Ce^{4+}, and Fe^{3+} aqueous electrolytes,

the authors concluded that all three oxidants inject holes both into the valence

band and the intra-band gap state. But from the ratio of edge to subband gap

EL intensity, Fe^{3+} appeared to inject holes less efficiently into the valence

band than the other two oxidants. Rates of hole injection for Ce^{4+} and

$Fe(CN)_6^{3-}$ were described as comparable and greater than that for Fe^{3+}.

Studies of GaAs have been extended to provide a unique example of EL from a

p-type semiconductor. Uosaki and Kita report edge emission from p-GaAs in $S_2O_8^{2-}$

electrolyte under strong reverse bias (149). Their data provide evidence for

the formation of an inversion layer under these conditions. They found that EL

intensity increased with carrier concentration but was at best only a few

percent of that obtained with n-GaAs samples under the same conditions. These

researchers also examined EL from n-GaAs samples of various carrier concentrations

and found that peak energy and width of the edge emission band increased with

carrier concentration (150). Time-resolved EL studies were conducted, as well.

EL from forward-biased n-InP electrodes has been observed in aqueous solutions of HNO_3 by Aharon-Shalom and Heller (151). The edge emission at 1.34 eV is initiated at potentials of 0.0 to -0.5 V vs SCE, depending on solution composition, and has a measured efficiency of as much as $\sim 10^{-5}$ to 10^{-4}. Chemistry in the electrolyte is sufficiently complex that it was difficult to identify the h^+-injecting species, but possible candidates include NO_2 and NO_2^+. EL properties were studied as a function of several variables including pH, nitrate and nitrite concentrations, potential, and excitation mode (dc vs ac). Temporal studies were also reported. The stability of the n-InP electrode was

gauged under prolonged cycling conditions. Some corrosion was evident from the presence of In(III) in solution, but the rate appeared to be slow (0.36 µg InP/Coulomb) and decreased with increasing nitrate concentration. Many of the features of this system were interpreted in terms of the presence of a chemically passive, thin (6-10 Å) layer of hydrated indium oxide on the InP surface which permits free tunneling of electrons and minimizes surface recombination velocity. In general, little attention has been paid to possible differences in surface and bulk compositions in EL measurements, yet, as discussed in this study, such differences can have significant electrooptical consequences.

V. EMISSIVE INHOMOGENEOUS SEMICONDUCTOR ELECTRODES

A. Background

The homogeneous semiconductor electrodes described thus far provide considerable insight into the location of electric fields within the solids and the interplay of those fields with interfacial conditions and excited-state deactivation routes. A strategy for examining these effects with greater spatial resolution is to prepare inhomogeneous semiconductor electrodes: By examining materials whose emission spectra depend on the site of recombination in the solid, it should be possible to more accurately map the electric field in the electrode. Such color-coded emission can also be exploited in the construction of novel display devices.

While these features are very appealing, there is a sacrifice made in working with inhomogeneous solids and that is that their electronic structures are considerably more complex. The isotype (n-type) heterojunctions which form the basis of the studies conducted at this writing exhibit fascinating properties but additionally pose numerous questions whose answers will require a better understanding of electronic structure within the inhomogeneous zone.

In this section, the emissive properties of two classes of inhomogeneous electrodes will be discussed. Graded CdS_XSe_{1-X} electrodes formed the basis of our initial studies (26,27,29). This work was followed by an examination of luminescence from $GaAs_{1-X}P_X-GaAs_{1-Y}P_Y$ isotope heterojunction electrodes (28).

B. Graded CdS_XSe_{1-X} Electrodes

A logical choice for preparing an inhomogeneous semiconductor electrode with color-coded emission is the CdS_XSe_{1-X} system. Recall that $\lambda_{max}(nm)$ for emission shifts linearly with composition (eq. [4]) in CdS_XSe_{1-X} compounds. Previous studies have established that CdS_XSe_{1-X} samples may be prepared by the vapor-phase diffusion of S into CdSe (CdSe/S) or Se into CdS(CdS/Se); homogeneous, mixed samples were obtained in long-term exchange reactions, whereas graded materials resulted from short-term experiments (56,152-158). Neutral interstitial chalcogens were proposed to be the diffusing defect (152).

We prepared graded solids from single-crystal, etched samples. Initial studies were conducted by heating CdSe in an evacuated quartz ampule, first in the presence of S, then in the presence of Cd; the latter heat treatment was necessary to yield a conductive solid, since heating in the presence of S makes the material very resistive, presumably by filling chalcogen vacancies in the lattice. As expected, the depth of the graded region could be varied by the temperature and duration of the heat treatment. At 700°C, a 60-min heat treatment yielded a graded zone of ∿2 μm thickness (26), whereas 15 min of heating produced a ∿1- μm graded region (27).

The graded nature of the material was evidenced by Auger electron spectroscopy (AES) using Ar ion sputter etching. Fig. 26 presents AES data showing a surface composition of nearly CdS ($X \cong 0.98$) and a monotonic decrease in S content over ∿1 μm until the substrate CdSe composition is reached; at any of the sputter times of Fig. 26, the fractional S and Se compositions sum to

roughly unity, as expected for Se/S lattice substitution. The sputter rate
provides a rough measure of the graded region's thickness. An independent
measurement was made by exposing different strata in the graded zone through
chemical etching: as described below, PL changes accompany this process
and, by restricting etching to half of the sample by use of a mask while
etching until substrate PL was seen, the thickness of the graded zone
could be estimated by measuring step heights with a contacting stylus.
The AES data are, of course, uninformative with regard to the crystallinity
of the graded layer. Indirect evidence for some degree of crystallinity
came from a long-term CdSe/S heat treatment (4 days at 700°C): an X-ray
powder pattern of the exchanged solid indicated the presence of crystalline
CdS (26).

PL properties of the CdSe/S samples corroborate their graded composition.
Curve 1 of Fig. 27 is the PL spectrum of a CdSe/S sample with an $\sim$2-μm thick
graded region. The observation of emitted light from $\sim$470-750 nm is consistent
with emissive contributions from CdS_xSe_{1-x} compositions which comprise the
graded region (eq. [4]). That PL from these graded samples is derived from
PL characteristic of homogeneous CdS_xSe_{1-x} samples is also seen in chemical
etching: curves 2-5 of Fig. 27, spectra obtained after successive chemical
etchings, illustrate the red shift expected for loss of S-rich, near-surface
compositions. It is noteworthy that although the PL spectra appear to be
dominated by edge emission, contributions from subband gap transitions cannot
be rigorously excluded. Another caveat is that some lateral inhomogeneity may
occur in sample preparation. Evidence for this is that modest variations in
the PL spectrum are observed when a focused laser beam excites the semiconductor
at various positions on its surface.

Further PL evidence for a CdSe/S graded region comes from the dependence of the spectral distribution on excitation wavelength. In general, more deeply penetrating wavelengths yield spectra with greater contributions from Se-rich compositions. An interesting feature in this regard is that PL is observed from compositions well beyond the penetration depth of the incident light which is ~ 0.1 μm. To what extent this reflects e^--h^+ ambipolar diffusion and/or excited-state energy transfer processes has yet to be determined.

Of particular interest to us was the effect of applied potential on PL properties. When CdSe/S samples are used as electrodes in sulfide electrolyte, their PL spectra are quenched asymmetrically by applied potential. Fig. 28 reveals that PL from S-rich, near-surface compositions is quenched by modest applied potentials; in contrast, negligible quenching occurs for $\lambda \geq 600$ nm. These data provide a crude map of the effective electric field in the solid: a PL wavelength of 600 nm corresponds to a composition of $\sim CdS_{0.5}Se_{0.5}$ which, from the AES/sputter etch data, occurs ~ 0.2 μm from the electrode surface (27). Thus, beyond ~ 0.2 μm from the surface, the electric field does not appear to be sufficiently strong to disrupt the recombination of e^--h^+ pairs; with the CdSe/S sample having a 2-μm thick graded zone, the corresponding diminution in electric field occurred at ~ 0.4 μm (26).

An independent measurement of the effective electric field is the photoaction spectrum. The inset of Fig. 28 indicates that the graded samples give reasonable i-V curves and the wavelength dependence of current is readily measured. A photoaction spectrum reveals that photocurrent from the electrode of Fig. 28 rises steeply below ~ 560 nm, supporting the conclusion from PL that near-surface, S-rich compositions are chiefly responsible for photocurrent (27).

Although we initially attempted a more complete analysis of PL quenching

in these graded samples using the aforementioned molecular model (vide supra,

Section IIIA), the foregoing explanation is more in accord with the dead-layer

model. At this point, a detailed analysis is limited by the complexity of

the electronic structure of the solid and uncertainties in material properties

(lateral inhomogeneity, e.g.). It is important to recognize, however, that

the electric field in such systems consists not only of space-charge and

applied voltage contributions but also of terms based on band edge and effective

mass gradients, hence the term "effective electric field" (159, 160).

A particularly exciting feature of the CdSe/S systems with thin graded

zones became evident in EL experiments conducted in $OH^-/S_2O_8^{2-}$ electrolyte:

With $\sim$1-μm thick graded regions, the EL spectral distribution is strongly

potential dependent. Fig. 29 demonstrates that as little as a 300-mV shift in

EL initiation potential causes the color of the emitted light to shift

reversibly from red to green! The direction of the spectral shift is such

that as the initiation potential becomes more cathodic, EL originates,

on average, nearer the semiconductor-electrolyte interface. A possible

explanation for this is that the concentration of conduction band electrons

needed for near-surface recombination increases with cathodic potential.

This ability to, in a sense, direct traffic of e^--h^+ pairs in the solid with

applied potential can, of course, be exploited in the construction of

variable-color display devices (161).

An interesting complementary graded system to that described above is

CdS/Se. A reverse graded band gap can be prepared by heating n-CdS at 700°C,

first in the presence of Se (15 min), then in the presence of Cd (30 min)

to restore conductivity (29). This treatment yields a surface composition

of $\sim CdS_{0.2}Se_{0.8}$ and a graded thickness of $\sim 0.7-0.9$ µm by AES/sputter etch data. The PL spectrum of this sample, shown in Fig. 30, differs markedly from that of CdSe/S samples having comparably thick graded zones for similar optical penetration depths: In contrast to the broad band of the latter, the CdS/Se sample exhibits a band at ~ 680 nm (40 nm fwhm), corresponding essentially to the emission of near-surface compositions. We suspect that the large difference in spectral characteristics between these materials hinges on their relative graded-gap structures. Specifically, for CdS/Se, the presence of the smallest band gap material at the surface disfavors h^+ transport toward the bulk along an intrinsic valence band edge gradient as well as excited-state energy transfer, processes which may occur in graded CdSe/S samples. An alternate means for investigating the gradient in the CdS/Se system is to remove the graded zone from one side by chemical etching and to excite through the exposed CdS by using light whose energy falls between the CdSe and CdS band gaps (1.7 to 2.4 eV). In this "backside" illumination, a broad PL band is, in fact, observed.

With "frontside" illumination in a PEC employing polysulfide electrolyte, the graded CdS/Se electrode exhibits modest quenching with an occasional preferential quenching of the low-energy tail, Figure 30. Using the arguments applied to the graded CdSe/S system, the effective electric field appears to extend at least 0.1-0.2 µm into the material from the AES/sputter etch and PL quenching data. Another estimate can be made by "backside" illumination of the electrode (the CdS surface is covered by a transparent polymer to permit excitation but not charge transfer). Figure 31 reveals that asymmetric quenching of the broad PL band occurs and supports the estimate of the thickness of the effective electric field as being $\sim 0.1-0.2$ µm. Photo-action spectra obtained with "backside" illumination also support this estimate.

The EL spectrum of the graded CdS/Se sample resembles the PL spectrum obtained with "frontside" illumination. In contrast to the CdSe/S sample of similar graded thickness, no significant potential dependence was observed, presumably reflecting the difference in electronic structure of the two materials as discussed above.

Before leaving the graded CdS_xSe_{1-x} system, it is worth noting that the electrodes offer display possibilities through spatially-controlled chemical etching (162). As shown in Figure 32 for a graded CdS/Se electrode, removal of some or all of the graded zone affords a change in the color of emission from the etched region. By appropriate masking and etching techniques, patterned, multi-colored emitting electrodes are readily fabricated. We have crudely prepared such electrodes from both graded CdS/Se and CdSe/S substrates by masking a portion of the electrode surface and chemically etching the exposed material with HCl or Br_2 in water. The etching was done incrementally, and the electrode was used to generate EL between each etching step so that the extent of removal of the graded layer could be inferred from the color of the emission. After removal of the mask with acetone, the electrode displayed two-toned EL.

An alternative to chemical etching of the graded layer is photoelectrochemical etching (PEC etching) in which the semiconductor electrode is irradiated under reverse bias in a cell with a non-stabilizing electrolyte (64,65). For CdS/Se electrodes, PEC etching is advantageous in that the extent of etching can be controlled by excitation wavelength (163) : Because bandgap increases with depth over the graded zone, etching with monochromatic light of energy between ∿1.7 and 2.4 eV will only proceed until a composition whose band gap roughly matches the photon energy is exposed to the electrolyte; of course, an alternative to monochromatic light is a white light source with

an appropriate cutoff filter. One other advantage of PEC etching for both

the CdS/Se and CdSe/S electrodes is that patterns can be generated by projection

rather than by physically masking the surface.

C. $GaAs_{1-X}P_X$-$GaAs_{1-Y}P_Y$ Isotype Heterojunction Electrodes

A second strategy for the preparation of inhomogeneous electrodes

exploits the tremendous potential of techniques like metal-organic chemical

vapor deposition (MOCVD) or molecular beam epitaxy (MBE) which can be used

to grow samples by depositing layers of atoms. Solid solutions of n-GaAs

and n-GaP, which form direct band gap materials of $n\text{-}GaAs_{1-X}P_X$ so long as

$X \lesssim 0.44$, were used to illustrate emissive properties of isotype heterojunction

electrodes (28).

Samples were prepared by the MOCVD technique (164). Their compositions

consist of a n-GaAs substrate covered, in turn, by layers of n-GaAs (2.0 μm),

$n\text{-}GaAs_{0.93}P_{0.07}$ (2.0 μm), $n\text{-}GaAs_{0.76}P_{0.24}$ (1.9 μm), $n\text{-}GaAs_{0.59}P_{0.41}$ (1.9 μm)

and $n\text{-}GaAs_{0.70}P_{0.30}$ (0.2 μm). The samples were conductive with a carrier

concentration of $\sim 10^{17}$ cm^{-3}.

A PL spectrum of the sample, shown in Fig. 33, consists of two overlapping

bands originating from the "bulk" $GaAs_{0.59}P_{0.41}$ and "surface" $GaAs_{0.70}P_{0.30}$

compositions. Homogeneity within the layers was demonstrated from the integrity

of the individual PL bands observed with different excitation wavelengths and

after chemical etching. As expected, the relative intensities of the two bands

vary with these parameters.

Applied potential can also be used to influence the relative intensities

of the bands. Fig. 33 reveals that when the sample is used as an electrode

in aqueous ditelluride electrolyte, PL from the "surface" layer is quenched

to a greater extent than "bulk" PL. Quenching in both layers can be treated

quantitatively by the dead-layer model. For the "bulk" emission, the dead-layer thickness is given by the conventional expression, eq. [15], where α^b is the

$$D^b = \frac{-1}{\alpha^b} \ln\left(\frac{PL^b}{PL^b_{FB}}\right) \qquad [15]$$

absorptivity of the bulk layer for the excitation wavelength, and PL^b and PL^b_{FB} are the in-circuit and flat-band (approximated as open circuit) PL intensities. For the surface PL band, the dead-layer model is easily modified using the partitioning of absorbed light shown in Fig. 34. The expression for the "surface" layer's dead-layer thickness is given by eq. [16], where the

$$D^s = \frac{-1}{\alpha^s} \ln\left\{\frac{PL^s}{PL^s_{FB}} \ [1-\exp(-\alpha^s X)] + \exp(-\alpha^s X)\right\} \qquad [16]$$

superscript s refers to the surface layer and X is the thickness of the surface layer; the incomplete quenching observed for the surface band indicates that $D^s < X$. The validity of these expressions was demonstrated by observing the quenching from different excitation wavelengths, as done for homogeneous electrodes.

The EL properties of this electrode were initially investigated in aqueous $OH^-/S_2O_8^{2-}$ electrolyte, but rapid loss of the "surface" band indicated gross instability in this medium. By using formamide as a solvent, a 0.5 M $Na_2S_2O_8$ solution could be used to generate stable EL spectra. Fig. 35 reveals that hole injection in this medium leads primarily to radiative recombination in the "surface" layer, the spectrum being dominated by this emission.

Although the spectral changes observed for this system are modest, they are important proof-of-concept experiments for demonstrating that inhomogeneous semiconductor electrodes can give rise to novel electrooptical effects. The

ability to tune sample composition at the atomic level can be used to
vary junction and layer thicknesses and carrier concentrations, as well as
to prepare superlattices. Materials science thus offers enormous potential
for investigating the interrelationship of interfacial properties and
excited-state decay routes in semiconductor electrodes.

VI. SUMMARY

The electronic structure of semiconductors makes the investigation of
interfaces constructed from these materials well-suited to electro-optical
interrogation. This review has focused on the use of luminescence as an
in-situ probe of the semiconductor-electrolyte interface. Emissive studies
have shown that the excited states of these solids, whether populated by
photoexcitation or electrical excitation, can be substantially influenced
by physicochemical properties of the interface. Of particular significance
is the use of emission to characterize electric fields occurring within the
semiconductor.

In order to extend these studies, surface and bulk effects need to be
decoupled. Models for doing this have been proposed for the emission from
homogeneous solids, and their successful application should provide detailed
information about the semiconductor-electrolyte interface, including rates
of interfacial charge transfer. More generally, separation of surface and
bulk effects should permit characterization of virtually any optically-accessible
semiconductor interface. Examples presented herein included interfaces of
semiconductors with electrolytes, metals, and other semiconductors.
The nature of these interfaces is clearly reflected in the experiments
which can be brought to bear on them, including absorption, emission, excitation
and photoaction spectroscopy, and temporal measurements. Realizing the full

electronic, thermodynamic, and kinetic information content which is intimated

by the studies conducted thus far is the exciting and challenging direction

of future work.

1. A. J. Nozik, Annu. Rev. Phys. Chem. 29, 189 (1978).

2. M. S. Wrighton, Acc. Chem. Res. 12, 303 (1979).

3. A. J. Bard, Science (Washington, D.C.) 207, 139 (1980).

4. A. Heller, Acc. Chem. Res. 14, 154 (1981).

5. A. Heller, Science (Washington, D.C.) 223, 1141 (1984).

6. H. Gerischer, In "Physical Chemistry: An Advanced Treatise", Vol. 9A;
    H. Eyring, D. Henderson, W. Jost, Eds.; Academic Press: New York,
    1970; Chapter 5.

7. A. B. Ellis, S. W. Kaiser, J. M. Bolts, and M. S. Wrighton, J. Am. Chem. Soc.
    99, 2839 (1977).

8. K. D. Legg, A. B. Ellis, J. M. Bolts, and M. S. Wrighton,
    Proc. Nat. Acad. Sci.,U.S.A. 74, 4116 (1977).

9. A. Fujishima and K. Honda, Nature 238, 37 (1972).

10. M. S. Wrighton, D. L. Morse, A. B. Ellis, D. S. Ginley, and
    H. B. Abrahamson, J. Am. Chem. Soc. 98, 44 (1976).

11. M. S. Wrighton, A. B. Ellis, P. T. Wolczanski, D. L. Morse,
    H. B. Abrahamson, and D. S. Ginley, J. Am. Chem. Soc. 98, 2774 (1976).

12. A. B. Ellis, S. W. Kaiser, and M. S. Wrighton, J. Phys. Chem. 80,
    1325 (1976).

13. H. Gerischer, J. Electroanal. Chem. Interfacial Electrochem. 58, 263 (1975).

14. S. Fonash, "Solar Cell Device Physics"; Academic Press: New York, 1981.

15. A. J. Bard, A. B. Bocarsly, F.-R. F. Fan, E. G. Walton, and M. S. Wrighton,
    J. Am. Chem. Soc. 102, 3671 (1980).

16. F.-R. F. Fan and A. J. Bard, J. Am. Chem. Soc. 102, 3677 (1980).

17. A. Fujishima, Y. Maede, K. Honda, G. H. Brilmyer, and A. J. Bard,
    J. Electrochem. Soc. 127, 840 (1980).

18. R. E. Halsted, In "Physics and Chemistry of II-VI Compounds"; M. Aven amd J. S. Prener, Eds.; North-Holland Publishing Co: Amsterdam, 1967; Chapter 8.

19. J. I. Pankove, "Optical Processes in Semiconductors"; Dover: New York, 1971.

20. R. A. Smith, "Semiconductors", 2nd Ed.; Cambridge University Press: Cambridge, 1978; Chapters 3.5, 9.5, and 10.14.

21. A. B. Ellis, J. Chem. Ed. 60, 332 (1983).

22. N. N. Winogradoff, Phys. Rev. 138, A1562 (1965).

23. E. W. Williams and R. A. Chapman, J. Appl. Phys., 38, 2547 (1967).

24. H. C. Casey, Jr. and E.Buehler, Appl. Phys. Lett. 30, 247 (1977).

25. T. Suzuki and M. Ogawa, Appl. Phys. Lett. 34, 447 (1979).

26. H. H. Streckert and A. B. Ellis, J. Phys. Chem. 86, 4921 (1982).

27. M. K. Carpenter, H. H. Streckert, and A. B. Ellis, J. Solid State Chem. 45, 51 (1982).

28. W. S. Hobson, P. B. Johnson, A. B. Ellis, and R. M. Biefeld, Appl. Phys. Lett. 45, 150 (1984).

29. M. K. Carpenter and A. B. Ellis, J. Electroanal. Chem. Interfacial Electrochem., in press.

30. H. W. Leverenz, "An Introduction to Luminescence of Solids"; Dover: New York, 1968, Chapter 5.

31. E. M. Williams and R. Hall, "Luminescence and the Light Emitting Diode", International Series on Science of the Solid State, Vol. 13; Pergamon Press: Oxford, 1978.

32. J. I. Pankove, Ed. "Electroluminescence", Topics in Applied Physics, Vol. 17; Springer-Verlag: Berlin, 1977.

33. H. Hartmann, R. Mach, and B. Selle, In "Current Topics in Materials Science", Vol. 9; E.Kaldis, Ed.; North-Holland Publishing Co: Amsterdam, 1982; Chapter 1, Section 3.2.

34. K. H. Beckmann and R. Memming, J. Electrochem. Soc. 116, 368 (1969).

35. G. Petermann, H. Tributsch, and R. Bogomolni, J. Chem. Phys. 57, 1026 (1972).

36. A. B. Ellis and B. R. Karas, J. Am. Chem. Soc. 101, 236 (1979).

37. A. B. Ellis and B. R. Karas, Adv. Chem. Ser. 184, 185 (1980).

38. B. R. Karas and A. B. Ellis, J. Am. Chem. Soc. 102, 968 (1980).

39. A. C. Aten and J. H. Haanstra, Phys. Lett. 11, 97 (1964).

40. A. C. Aten, J. H. Haanstra, and H. deVries, Philips Res. Rep. 20, 395 (1965).

41. J. D. Cuthbert and D. G. Thomas, J. Appl. Phys. 39, 1573 (1968).

42. D. M. Roessler, J. Appl. Phys. 41, 4589 (1970).

43. J. D. Cuthbert, J. Appl. Phys. 42, 739 (1971).

44. P. F. Moulton, Ph.D. Dissertation, Massachusetts Institute of Technology, 1975.

45. R. H. Bube, Phys. Rev. 98, 431 (1955).

46. B. R. Karas, D. J. Morano, D. K. Bilich, and A. B. Ellis, J. Electrochem. Soc. 127, 1144 (1980).

47. A. B. Ellis and B. R. Karas, ACS Symposium Series 146, 295 (1981).

48. B. R. Karas, H. H. Streckert, R. Schreiner, and A. B. Ellis, J. Am. Chem. Soc. 103, 1648 (1981).

49. B. DiBartolo, "Optical Interactions in Solids"; Wiley: New York, 1968; Chapter 18.3.

50. P. J. Wagner, In "Creation and Detection of the Excited State", Vol. I, Part A; A. A. Lamola, Ed.; Marcel Dekker: New York, 1971.

51. J. H. Richardson, S. P. Perone, L. L. Steinmetz, and S. B. Deutscher, Chem. Phys. Lett. 77, 93 (1981).

52. H. H. Streckert, J. Tong, and A. B. Ellis, J. Am. Chem. Soc. 104, 581 (1982) and references therein.

53. H. H. Streckert, J. Tong, M. K. Carpenter, and A. B. Ellis,

    J. Electrochem. Soc. 129, 772 (1982).

54. H. H. Streckert, J. Tong, M. K. Carpenter, and A. B. Ellis, In

    "Photoelectrochemistry: Fundamental Processes and Measurement

    Techniques", Vol. 82-3; W. L. Wallace, A. J. Nozik, S. K. Deb, and

    R. H. Wilson, Eds.; Electrochemical Society: Pennington, New Jersey,

    1982; p. 633.

55. F. L. Pedrotti and D. C. Reynolds, Phys. Rev. 127, 1584 (1962).

56. E. T. Handelman and W. Kaiser, J. Appl. Phys. 35, 3519 (1964).

57. R. H. Bube, J. Appl. Phys. 35, 586 (1964).

58. Y. S. Park and D. C. Reynolds, Phys. Rev. 132, 2450 (1963).

59. R. N. Noufi, P. A. Kohl, and A. J. Bard, J. Electrochem. Soc. 125,

    375 (1978).

60. R. H. Bube, Phys. Rev. 98, 431 (1955).

61. G. Oelgart, R. Stegmann, and L. John, Phys. Status Solidi A 59, 27

    (1980).

62. M. S. Wrighton, D. S. Ginley and D. L. Morse, J. Phys. Chem. 78, 2229 (1974).

63. R. B. Parsons, W. Wardzynski, and A. D. Yoffe, Proc. R. Soc. London, A

    262, 120 (1961).

64. R. Tenne and G. Hodes, Appl. Phys. Lett. 37, 428 (1980).

65. For reviews, see G. Hodes, In "Energy Resources through Photochemistry

    and Catalysis"; M. Grätzel, Ed.; Academic Press: New York, 1983; pp. 458-61,

    and R. Tenne and G. Hodes, Surf. Sci. 135, 453 (1983).

66. G. Hodes, D. Cahen, and H. J. Leamy, J. Appl. Phys. 54, 4676 (1983).

67. A review is presented on pp. 434-48 of reference 65a.

68. R. P. Silberstein and M. Tomkiewicz, J. Appl. Phys. 54, 5428 (1983).

69. Z. Harzion, N. Croitoru, and S. Gottesfeld, J. Electrochem. Soc. 128,

    551 (1981).

70. Z. Harzion, D. Huppert, S. Gottesfeld, and N. Croitoru, _J. Electroanal. Chem. Interfac. Electrochem._ 150, 571 (1983).

71. H. H. Streckert, H. Van Ryswyk, R. N. Biagioni, and A. B. Ellis, _J. Phys. Chem._ 88, 1544 (1984).

72. R. Baltrameyunas, Yu. Vaitkus, and V. Nyunka, _Sov. Phys.-Solid State_ (Engl. Transl.) 20, 1346 (1978).

73. R. G. Wheeler and J. O. Dimmock, _Phys. Rev._ 125, 1805 (1962).

74. N. J. Turro, "Modern Molecular Photochemistry"; Benjamin/Cummings: Menlo Park, California, 1978; Chapter 8.

75. A. B. Ellis, B. R. Karas, and H. H. Streckert, _Faraday Discuss. Chem. Soc. No. 70._, 165 (1980).

76. A. Fujishima, Y. Maeda, S. Suzuki, and K. Honda, _Chem. Lett._ 1982, 179.

77. A. Fujishima, Y. Maeda, and K. Honda in reference 54, pg. 562.

78. W. S. Hobson and A. B. Ellis, _Appl. Phys. Lett._ 41, 891 (1982).

79. D. B. Wittry and D. F. Kyser, _J. Appl. Phys._ 38, 375 (1967).

80. R. E. Hetrick and K. F. Yeung, _J. Appl. Phys._ 42, 2882 (1971).

81. U. Langmann, _Appl. Phys._ 1, 219 (1973).

82. G. K. Volodina, L. I. Gorshkov, G. P. Peka, and V. I. Strikha, _J. Appl. Spectrosc._ 29, 1077 (1978).

83. K. Ando, A. Yamamoto, and M. Yamaguchi, _J. Appl. Phys._ 51, 6432 (1981).

84. K. Ando, A. Yamamoto, and M. Yamaguchi, _Jpn. J. Appl. Phys._ 20, 679 (1981).

85. K. Ando, A. Yamamoto, and M. Yamaguchi, _Jpn. J. Appl. Phys._ 20, 1107 (1981).

86. R. E. Hollingsworth and J. R. Sites, _J. Appl. Phys._ 53, 5357 (1982).

87. W. S. Hobson, Ph.D. Thesis, University of Wisconsin-Madison (1984).

88. K. Mettler, _Appl. Phys._ 12, 75 (1977).

89. W. S. Hobson and A. B. Ellis, _J. Appl. Phys._ 54, 5956 (1983).

90. D. D. Sell and H. C. Casey, Jr. _J. Appl. Phys._ 45, 800 (1974).

91. C. J. Hwang, _J. Appl. Phys._ 40, 3731 (1969).

92. M. Green, J. Chem. Phys. 31, 200 (1959).

93. V. A. Myamlin and Y. V. Pleskov, "Electrochemistry of Semiconductors";
    Plenum: New York, 1967; pp. 23-149.

94. L. Jastrzebski, J. Lagowski, and H. C. Gatos, Appl. Phys. Lett.
    27, 537 (1975).

95. R. J. Nelson, J. S. Williams, H. J. Leamy, B. Miller, H. C. Casey, Jr.,
    B. A. Parkinson, and A. Heller, Appl. Phys. Lett. 36, 76 (1980).

96. B. A. Parkinson, A. Heller, and B. Miller, J. Electrochem. Soc.
    126, 954 (1979).

97. M. Green, In "Modern Aspects of Electrochemistry"; J. O'M. Bockris, Ed.;
    Butterworths: London, 1959; Chapter 2.

98. W. P. Gomes and F. Cardon, Prog. Surf. Sci. 12, 155 (1982) and
    references therein.

99. R. Garuthara, M. Tomkiewicz, and R. P. Silberstein, J. Appl. Phys.
    54, 6787 (1983).

100. A. A. Burk, Jr., A. B. Ellis, D. Ridgley, and A. Wold, J. Lumin.,
     in press.

101. S. Tanaka, J. A. Bruce, and M. S. Wrighton, J. Phys. Chem. 85, 3778 (1981).

102. H. S. White, A. J. Ricco, and M. S. Wrighton, J. Phys. Chem. 87, 5140
     (1983).

103. P. B. Johnson, W. S. Hobson, and A. B. Ellis, unpublished observations.

104. P. M. Smiley, R. N. Biagioni, and A. B. Ellis, J. Electrochem. Soc.
     131, 1068 (1984).

105. D. Curie and J. S. Prener, In "Physics and Chemistry of II-VI Compounds";
     M. Aven and J. S. Prener, Eds.; North-Holland Publishing Co: Amsterdam,
     1967; Chapter 9.4 and references therein.

106. S. Iida, J. Phys. Soc. Jpn. 25, 177 (1968).

107. G. Jones and J. Woods, J. Lumin. 9, 389 (1974).

108. S. Satoh and K. Igaki, Jpn. J. Appl. Phys. 22, 68 (1983).

109. J. C. Bouley, P. Blanconnier, A. Herman, Ph. Ged, P. Henoc, and J. P. Noblanc, J. Appl. Phys. 46, 3549 (1975).

110. J. Gautron and P. Lemasson, J. Cryst. Growth 59, 332 (1982).

111. H. Gobrecht, M. Schaldach, F. Hein, and W. Paatsch, Electrochim. Acta 13, 1279 (1968).

112. H. Gobrecht and R. Blaser, Electrochem. Acta 13, 1285 (1968).

113. Y. Nakato, A. Tsumura, and H. Tsubomura, J. Phys. Chem. 87, 2402 (1983).

114. T. Fukui and Y. Horikoshi, Jpn. J. Appl. Phys. 18, 1651 (1979).

115. R. B. Stephens, Phys. Rev. B. 29, 3283 (1984).

116. L. J. Van Ruyven and F. E. Williams, Phys. Rev. Lett. 16, 889 (1966).

117. B. Pettinger, H.-R. Schöppel, T. Yokoyama, and H. Gerischer, Ber. Bunsenges. Phys. Chem 78, 1024 (1974).

118. H. Morisaki and K. Yazawa, Appl. Phys. Lett. 33, 1013 (1979).

119. H. Morisaki, H. Kitada, and K. Yazawa, Jpn. J. Appl. Phys. 19, 679 (1980).

120. J. Gautron, J.-P. Dalbéra, and P. Lemasson, Surf. Sci. 99, 300 (1980).

121. M. A. Butler and D. S. Ginley, Appl. Phys. Lett. 36, 845 (1980).

122. R. Memming and G. Schwandt, Surf. Sci. 4, 109 (1966).

123. R. Memming and F. Möllers, Ber. Bunsenges. Phys. Chem. 76, 609 (1972).

124. Reference 6, pp. 499-500.

125. R. Memming, In "Electroanalytical Chemistry", Vol. 11; A. J. Bard, Ed.; Marcel Dekker: New York, 1979; Chapter 1, pp. 21-2.

126. R. Memming and G. Schwandt, Electrochim. Acta 13, 1299 (1968).

127. R. Memming, J. Electrochem. Soc. 116, 785 (1968).

128. B. Pettinger, H.-R. Schöppel, and H. Gerischer, Ber. Bunsenges. Phys. Chem. 80, 849 (1976).

129. T. Yamase and H. Gerischer, Ber. Bunsenges. Phys. Chem. 87, 349 (1983).

130. Y. Nakato, A. Tsumura, and H. Tsubomura, Chem. Lett. 1981, 127.

131. Y. Nakato, A. Tsumura, and H. Tsubomura, ACS Symposium Series 146, 145 (1981).

132. Y. Nakato, A. Tsumura, and H. Tsubomura, Bull. Chem. Soc. Jpn. 55, 3390 (1982).

133. Y. Nakato, A. Tsumura, and H. Tsubomura, Chem. Phys. Lett. 85, 387 (1982).

134. R. N. Noufi, P. A. Kohl, S. N. Frank, and A. J. Bard, J. Electrochem. Soc. 125, 246 (1978).

135. J. G. Mavroides, Proc.-Electrochem. Soc. 77-3, 84 (1977).

136. H. H. Streckert, B. R. Karas, D. J. Morano, and A. B. Ellis, J. Phys. Chem. 84, 3232 (1980).

137. D. M. Kolb and H. Gerischer, Electrochem. Acta 18, 987 (1973).

138. H. Masuda, A. Fujishima, and K. Honda, Chem. Lett. 1980, 1153.

139. A. J. Bard, C. P. Keszthelyi, H. Tachikawa, and N. E. Tokel, In "Chemiluminescence and Bioluminescence"; M. J. Cormier, D. M. Hercules, and J. Lee, Eds.; Plenum Press: New York, 1973; pp. 193-208.

140. L. R. Faulkner and A. J. Bard, Electroanal. Chem. 10, 1 (1977).

141. C. P. Keszthelyi, N. E. Tokel-Takvoryan, and A. J. Bard, Anal. Chem. 47, 249 (1975).

142. N. Müller, M. Abramovich, F. Decker, F. Iikawa, and P. Motisuke, J. Electrochem. Soc. 131, 2204 (1984).

143. F.-R. F. Fan, P. Leempoel, and A. J. Bard, J. Electrochem. Soc. 130, 1866 (1983).

144. V. A. Tyagai, M. K. Sheinkman, E. L. Shtrum, G. Ya. Kolbasov, and N. K. Moiseeva, Sov. Phys.- Semicond. (Engl. Transl.), 14, 112 (1980)

145. D. J. Benard and P. Handler, Surf. Sci. 40, 141 (1983).

146. H. Gerischer, N. Müller, and O. Haas, J. Electroanal. Chem. Interfacial Electrochem. 119, 41 (1981).

147. F. Decker, B. Pettinger, and H. Gerischer, J. Electrochem. Soc. 130, 1335 (1983).

148. F. Decker, M. Abramovich, and P. Motisuke, J. Electrochem. Soc. 131, 1173 (1984).

149. K. Uosaki and H. Kita, J. Phys. Chem. 88, 4197 (1984).

150. K. Uosaki and H. Kita, Bull. Chem. Soc. Jpn., in press.

151. E. Aharon-Shalom and A. Heller, J. Phys. Chem. 87, 4913 (1983).

152. H. H. Woodbury and R. B. Hall, Phys. Rev. 157, 641 (1967).

153. H. F. Taylor, V. N. Smiley, W. E. Martin, and S. S. Pawka, Phys. Rev. B. 5, 1467 (1972).

154. H. F. Taylor, W. E. Martin, D. B. Hall, and V. N. Smiley, Appl. Phys. Lett. 21, 95 (1972).

155. L. J. Brillson and E. M. Conwell, J. Appl. Phys. 45, 5289 (1974).

156. W. E. Martin and D. B. Hall, Appl. Phys. Lett. 21, 325 (1972).

157. M. Kawabe, H. Kotani, K. Masuda, and S. Namba, Appl. Phys. Lett. 26, 46 (1975).

158. T. Gabor and G. H. Dierssen, J. Elctrochem. Soc. 122, 430 (1975).

159. T. Gora and F. Williams, Phys. Rev. 177, 1179 (1969).

160. L. J. Van Ruyven and F. E. Williams, Am. J. Phys. 35, 705 (1967).

161. A. B. Ellis and H. H. Streckert, U. S. Patent Application Serial No. 478,476.

162. A. B. Ellis and M. K. Carpenter, U. S. Patent Application Serial No. 480,471.

163. A. B. Ellis and M. K. Carpenter, U. S. Patent Application Serial No. 000000.

164. R. M. Biefeld, J. Crystal Growth 56, 382 (1982).

Table I. Optical to Electrical Energy Conversion Parameters[a]

Electrode	T,°C	$\lambda_{exc.}$	η_{max}[b]	E_V[c]	$\Phi_x @\eta_{max}$[d]	$\Phi_{x_{max}}$[e]
CdS:Te	23	501.7	5.6	0.32	0.44	0.75
		514.5	0.27	0.28	0.02	0.04
	73	501.7	3.8	0.21	0.44	0.74
		514.5	1.0	0.18	0.14	0.26
CdS	24	501.7	5.0	0.27	0.46	0.68
		514.5	0.21	0.27	0.02	0.03
	73	501.7	2.5	0.19	0.32	0.68
		514.5	0.92	0.24	0.09	0.20

[a] The indicated crystal served as the photoanode in a PEC similar to that shown in Figure 1 with a Pt counterelectrode. Electrolyte composition is 5M OH^-/0.3M Se^{2-}/0.001M Se_2^{2-}. Table entries represent typical values.

[b] Maximum efficiency for optical to electrical energy conversion calculated as (maximum electrical power out divided by input optical power) x 100.

[c] Output voltage at η_{max} in volts.

[d] Quantum efficiency for e^- flow at η_{max} ($\pm$ 15%), uncorrected for reflection losses and electrolyte absorption.

[e] Maximum quantum efficiency ($\pm$ 15%) for e^- flow, measured at ~0.7 V vs. Ag(PRE), uncorrected for reflection losses and electrolyte absorption.

Table 11. Temperature Dependence of Photoluminescence Spectra[a]

CdS$_X$Se$_{1-X}$ Sample, X	λ_{max}, nm(eV)[b]		Spectral Shift, eV[c]	Intensity Enhancement
	295 K	77 K		
1.00 (CdS)	508(2.44)	488(2.54) 502 sh (2.47) 510 sh (2.43) 592 (2.09)	0.10	50
0.74	563(2.20)	545 (2.27) 555 sh(2.23)	0.07	200
0.49	615(2.02)	591 (2.10) 604 sh(2.05)	0.08	200
0.11	695(1.78)	665 (1.86) 680 sh (1.82) 850(1.46)	0.08	100
0.00 (CdSe)	718(1.73)	681 (1.82) 698 sh (1.78) 830 (1.49)	0.09	20

Table II footnotes

a. Properties of uncorrected PL spectra of CdS_xSe_{1-x} samples excited with
457.9—nm excitation. Spectra were recorded at 295, 77,
and 295 K again to demonstrate reproducibility.

b. Emission band maxima at 295 and 77 K. At 77 K the highest-energy band
generally displayed a shoulder whose position is indicated by "sh". Other
bands were occasionally seen and their positions indicated as well. Spectral
resolution was ~ 2.0 nm.

c. Spectral shift between 295 and 77 K for the highest-energy emission band
maxima.

d. Factor by which the emitted intensity of the highest-energy band increased
on cooling from 295 to 77 K. This factor has been corrected for relative
detector sensitivity.

Table III. Measurements of Efficiency in Luminescent $CdS_X Se_{1-X}$ -based PECs [a]

$CdS_X Se_{1-X}$ Electrode, X	ϕ_{r_0}/ϕ_{r_i} [b]	$\phi_{x\,calc.}$ [c]	$\phi_{x\,meas.}$ [d]	ϕ_x at η_{max} [e]	E_v at η_{max}, V [f]	$\eta_{max,Z}$ [g]
1.00 (CdS)	1.7	0.41	0.37	0.30	0.42	4.6
0.74	15	0.93	0.91	0.63	0.42	9.7
0.49	7.8	0.87	0.86	0.55	0.35	7.1
0.11	37	0.97	0.90	0.58	0.34	7.3
0.00 (CdSe)	51	0.98	0.86[h]	0.65	0.39	9.3

Table III footnotes

a. PEC characterization parameters extracted from the iLV curves of Figure 14. The indicated crystal served as the photoanode in a PEC employing N_2-purged $1 M OH^-/1 M S^{2-}/0.1 M S$ polysulfide electrolyte; a Pt foil counterelectrode and SCE completed the PEC. Electrodes were irradiated with ~ 1.0 to 1.2 mW of 457.9 -nm excitation; their exposed surface areas were ~ 0.25 cm^2.

b. Ratio of open-circuit to in-circuit emission intensity with the in-circuit value taken at - 0.30 V vs SCE. Emission intensity was monitored at the emission band maximum.

c. Photocurrent quantum efficiency at - 0.30 V vs. SCE calculated from the ϕ_{r_0}/ϕ_{r_i} ratio in the preceding column and eq. [7] in the text.

d. Measured photocurrent quantum efficiency at - 0.30 V vs. SCE determined with a radiometer. Measured values are uncorrected for reflection and electrolyte absorption.

e. Measured photocurrent quantum efficiency at the potential where maximum optical to electrical energy conversion efficiency obtains.

f. Output voltage at the maximum energy conversion point. The redox potential of the polysulfide electrolyte was - 0.78 V vs. SCE.

g. (Maximum electrical power out divided by input optical power) x 100.

h. The electrolyte pathlength was visibly longer for this electrode than for the others and would, therefore, require a larger correction for electrolyte absorption.

Table IV. PL-Related Properties of n-GaAs-Based PECs.[a]

Electrode No. (n,cm^{-3})[b]	λ_{ex},nm[c]	ϕ_x[d]	ϕ_{xr}[e]	Dx10^8 cm (Å)[f]	Wx10^8 cm (Å)[g]
1 (4-8x10^{18})	457.9	0.62	0.09	60[i]	80-110
	514.5	0.44	0.07	80[i]	80-110
	632.8	0.33	0.07	160[i]	80-110
2 (1x10^{18})	457.9	0.77	0.15	100	280
	514.5	0.69	0.11	120	280
	632.8	0.75	0.06	120	280
3 (2.5x10^{17})	457.9	0.73	0.46	390	650
	514.5	0.64	0.30	380	650
	632.8	0.65	0.18	430	650
4 (4x10^{16})	457.9	0.76	0.89	1400	1600
	514.5	0.67	0.75	1500	1600
	632.8	0.75	0.48	1400	1600
5 (0.7-1x10^{16})	457.9	0.70	h	h	3300-3900
	514.5	0.69	0.84	2000	3300-3900
	632.8	0.69	0.60	2000	3300-3900

[a]Properties derived from iLV curves of n-GaAs-based PECs. The PECs consisted of a three-electrode potentiostatic setup and ditelluride electrolyte. Vigorous magnetic stirring and a N_2 blanket were used in all experiments.

[b]N-GaAs electrodes used in PECs. Carrier concentrations are given in parentheses. Electrodes 1 and 2 are (100) melt-grown samples from Laser Diode Laboratories doped with Si and Te, respectively. Electrode 3 is a (100) GaAs:Te melt-grown sample from Morgan Semiconductors, Inc. Electrodes 4 and 5 are VPE samples from McDonnell-Douglas Astronautics, Co. with epilayer thicknesses of 2.3 and 25 μm, respectively, on n$^+$ GaAs substrates. Electrode surface areas exposed to the electrolyte were ~0.18, 0.30, 0.18, 0.20 and 0.18 cm^2 for electrodes no. 1-5, respectively.

Table IV footnotes

[c] Excitation wavelengths from Ar^+ (457.9, 514.5 nm) and He-Ne (632.8 nm) lasers. Incident intensities of ~ 0.5-20 mW/cm^2 were used.

[d] Photocurrent quantum efficiency, defined as electrons flowing in the external circuit per photons absorbed. Data were obtained at -1.0 V vs. SCE and are uncorrected for solution absorption and reflective losses. Current densities of ~ 1-10 mA/cm^2 were measured.

[e] Fractional PL quenching, defined by Eq.[1u], between open circuit and -1.0 V vs. SCE. The open-circuit potentials were $\sim$ -1.35, -1.55, -1.75, -1.72, and -1.72 for electrodes no. 1-5, respectively; these potentials were relatively insensitive to light intensity over the ~ 0.5-20 mW/cm^2 intensity range employed. Error bars in ϕ_{xr} are $\sim \pm 0.02$. PL intensity was monitored at λ_{max}, ~ 870 nm.

[f] Dead-layer thickness at -1.0 V vs. SCE calculated from Eq.[8] using absorptivities given in ref. 89 and the corresponding fractional PL quenching values given in the adjacent column of this table.

[g] Depletion width at -1.0 V vs. SCE calculated by equating open-circuit potentials given in footnote e of this table with V_{FB}, and equating values of n given in the table with N_D. These should be treated as rough values owing to the uncertainties in N_D and V_{FB}. A value of 12.9 was used for the GaAs dielectric constant.

[h] The PL intensity was too weak at this excitation wavelength to obtain reliable data.

[i] There is somewhat greater uncertainty in these values owing to the smaller fractional quenching (ϕ_{xr}) observed.

Table V.   Potential Dependence of the Dead-Layer Thickness[a]

Electrode Potential,[b] V vs. SCE	$Dx10^8$ cm (Å)[c]		
	457.9 nm	514.5 nm	632.8 nm
-1.0	1400	1500	1400
-1.1	1300	1300	1300
-1.2	1100	1100	1100
-1.3	910	910	840
-1.4	670	700	620
-1.5	440	460	460
-1.6	210	240	230
-1.65	120	110	110
-1.72	0	0	0

[a]Dead-layer thickness, D, as a function of potential for n-GaAs electrode no. 4 (n ∿$4x10^{16}$ cm^{-3}) when used in the PEC described in footnote a of Table IV. The iLV data from which the D values in this table are derived are shown in Figure 17.

[b]Potential of the n-GaAs electrode; the open-circuit potential is -1.72 V.

[c]Calculation of dead-layer thickness from Eq. [8] using absorptivities given in ref. 89 and the fractional PL quenching (eq.[10]) between open-circuit (equated to V_{FB}) and the indicated potential. PL quenching data were obtained using each of the three indicated wavelengths for excitation; changes in PL intensity were monitored at λ_{max} ∿870 nm. Current densities are given in Figure 17.

Table VI. PL properties and measurements of efficiency in n-ZnSe:Al-based PEC's[a]

Electrode[b]	λ_{ex}, nm[c]	ϕ_r[d]	ϕ_x[e]	$(1 - \frac{\phi_{xr}}{\phi_{r_{FB}}})$[f]	$\phi_x @ \eta_{max}$[g]	$E_v @ \eta_{max}, V$[h]	η_{max} (%)[i]
as received	366	0.02	0.50	0.16	0.35	0.85	7.2
	405	0.03	0.25	0.11	0.18	0.85	4.9
	436	0.04	0.18	0.09	0.14	0.90	4.2
	460	0.05					
treated	366		0.60	0.38	0.42	0.85	10.4
	405		0.31	0.17	0.23	0.77	5.3
	436		0.22	0.13	0.13	0.73	3.6

[a] PL properties related to use of n-ZnSe:Al electrodes in PEC's. Most of the properties are derived from iLV curves generated with a three-electrode potentiostatic setup (n-ZnSe:Al working electrode, Pt foil counterelectrode and SCE reference electrode). To optimize transparency, experiments with 366-nm light were conducted in 10M KOH/0.25M Se^{2-}/0.001 M Se_2^{2-} electrolyte; for 405- and 436-nm light, an electrolyte of 8M KOH/0.2M Te^{2-}/0.002M Te_2^{2-} was employed. The electrode, having an exposed surface area of ~0.25 cm^2, was excited with ~0.5-2 mW of power.

[b] The n-ZnSe:Al sample was used either "as received" or treated with Se as described in ref. 104.

[c] Excitation wavelength. A 150-W high-pressure Xe lamp or 200-W high-pressure Hg lamp equipped with interference filters was employed for ϕ_r data and iLV curves, respectively.

[d] Radiative quantum efficiencies obtained in air for the SA band. Values are uncorrected for self-absorption and internal reflectivity.

[e] Measured photocurrent quantum efficiency at -1.0 V vs. SCE. Values are uncorrected for solution absorption and reflective losses.

[f] Fractional PL quenching between -1.0 V vs. SCE and the flat-band potential, approximated here as the open-circuit potential. PL intensity was monitored at 600 nm.

[g] Measured photocurrent quantum efficiency at the potential corresponding to maximum optical-to-electrical energy conversion efficiency.

[h] Output voltage at the maximum energy conversion point. The diselenide and ditelluride redox potentials were -0.95 and -1.10 V vs. SCE, respectively.

[i] (Maximum electrical power out divided by input optical power) x 100.

Table VII. Estimates of Electroluminescence Efficiency[a]

$CdS_X Se_{1-X}$ Electrode, X	Potential, V vs. SCE[b]	Total emitted light, μJ (10^{12} einsteins)[c]	10^3 total Coul (10^8 mole e^-)[d]	$10^4 \bar{\phi}_{EL}$[e]
1.00 (CdS)	-1.50	0.11 (0.49)	3.4 (3.5)	0.14
	-1.05	0.00063 (0.0027)	0.049 (0.050)	0.054
0.74	-1.50	0.23 (1.1)	6.8 (7.1)	0.15
	-1.00	0.0029 (0.014)	0.61 (0.63)	0.023
0.49	-1.50	0.61 (3.2)	9.7 (10.1)	0.32
	-1.00	0.0014 (0.0073)	0.080 (0.083)	0.088
0.11	-1.50	1.2 (7.1)	5.7 (5.9)	1.2
	-1.00	0.036 (0.21)	0.40 (0.42)	0.51
0.00 (CdSe)	-1.50	5.6 (34)	7.0 (7.2)	4.7
	-1.00	0.056 (0.34)	0.53 (0.55)	0.62

Table VII footnotes

a. A single-crystal, n-type CdS_xSe_{1-x} sample was used as the working electrode in a one-compartment EL experiment conducted in a N_2-purged 5 M NaOH/0.1 M $K_2S_2O_8$ electrolyte; a Pt foil counterelectrode and SCE completed the cell. The CdS_xSe_{1-x} exposed surface areas were ~ 0.25 cm^2.

b. EL experiments were conducted by pulsing the CdS_xSe_{1-x} electrode between 0.00 V (11 s) and the indicated potential (1 s).

c. Total emitted light collected per pulse with a radiometer operated in its integrating mode. The radiometer was placed ~ 1 cm away from the emitting electrode. If all of the indicated energy were converted to photons at the emission band maxima (508, 563, 615, 695 and 718 nm for X = 1.00, 0.74, 0.49, 0.11, and 0.00, respectively), the quantity of einsteins given in parentheses would be obtained.

d. Total coulombs collected per pulse with a digital coulometer. The value in parentheses is the corresponding quantity of electrons in the external circuit, obtained by dividing the coulombs by Faraday's constant.

e. Integrated EL efficiency. This value is derived by dividing the einsteins by the moles of electrons from the preceding columns. These efficiencies are lower limits, as described in the text. Table entries for each potential are representative values. At least five pulse sequences were used at each potential, yielding $\overline{\phi}_{EL}$ values within 10% of one another.

Figure Captions

Figure 1. A typical photoelectrochemical cell (PEC). At the irradiated
n-type semiconductor electrode, n-SC, electrolyte species A is oxidized
to A^+. The electrochemistry occurring at the dark counterelectrode, CE,
is reduction of A^+ to A. The net process is conversion of input optical
energy into electricity through the external circuit.

Figure 2. Interfacial energetics for a n-type semiconductor-electrolyte
system a) before and b) after equilibration. E_{redox} is the electrolyte
redox potential. The dashed line represents the semiconductor Fermi
level, E_F.

Figure 3. Excited-state deactivation pathways of an n-type semiconductor
electrode. Wavy arrows signify nonradiative decay routes: k_{nr}
and k_x correspond to electron (filled circle)-hole (open circle)
recombination leading to heat and e^--h^+ pair separation leading to
electrolyte redox reactions, respectively. The straight arrow
and k_r correspond to radiative e^--h^+ pair recombination, the source
of luminescence. CB and VB denote the conduction and valence band
edges. The displacement of E_F and E_{redox} corresponds to forward bias,
a potential negative of short circuit (E_{redox}). Intraband gap states
which might play a role in the various deactivation routes have been
omitted for simplicity.

Figure 4. Electronic structure of a semiconductor electrode. The lines
labelled "A" and "B" represent bulk electronic states while those
labelled "C" are surface states. [Reprinted from reference 21 with
permission].

Figure 5. Voltage dependence of PL intensity (I_F) and photocurrent density (I_{pH}) of an n-ZnO-based PEC. The electrode was excited with 350-nm light and its PL intensity monitored at 500 nm. The dashed curve shows the mirror image of the photocurrent density. [Reprinted from reference 35 with permission].

Figure 6. Photocurrent (solid line, left hand scale) and emission intensity (dashed line, right-hand scale) monitored at 600 nm vs. potential for a CdS:Te,100-ppm,single-crystal electrode in 5M OH^-/0.117M Se^{2-}/0.001 M Se_2^{2-} electrolyte excited at 514.5 nm (top frame) and 496.5 nm (bottom frame). The Ar ion laser was beam expanded and irradiated the ∿0.25 cm^2 exposed area of the electrode with ∿0.8 mW at 514.5 nm and ∿1 mW at 496.5 nm. The iLV curves were swept at ∿13 mV/sec. E_{redox} is -0.96 V vs. SCE. [Reprinted from reference 38 with permission].

Figure 7. Current-luminescence-voltage (iLV) curves for a 100-ppm,single-crystal CdS:Te electrode in diselenide electrolyte. Unprimed, solid-line curves are photocurrent (left-hand scale) and primed, dotted-line curves are emission intensity (right-hand scale) monitored at λ_{max} ∿600 nm. Curves A and A' result from excitation at 501.7-nm, 23°C; curves B and B' from 514.5-nm excitation at 23°C; curves C and C', 49°C and 501.7-nm excitation; curves D and D', 86°C, 514.5-nm irradiation. Note that the ordinate of curve D' has been expanded by a factor of 10. Equivalent numbers of 501.7- and 514.5-nm photons were used to excite the photoelectrode in identical geometric configurations. The exposed electrode area is ∿0.41 cm^2, corresponding to an estimated ϕ_x value for 501.7-nm excitation at 23°C and +0.7 V vs. Ag (pseudoreference electrode) of ∿0.50, uncorrected for solution absorbance and reflection losses. [Reprinted from reference 46 with permission].

Figure 8. Uncorrected emission spectra of a 100-ppm,CdS:Te electrode as

a function of potential and temperature in sulfide (1M OH$^-$/1M S^{2-})

electrolyte. Frames a, b, and c are data taken at 295, 312 and 333 K,

respectively. Curves 1, 2, 3, 4 and 5 in each frame correspond to

open circuit, -0.5, -0.3, +0.15 and +0.7 V vs. Ag (pseudoreference

electrode), respectively. Pt foil (1x3 cm) served as the counter-

electrode in the N$_2$-purged PEC. Because PEC geometry and incident

intensity ($\sim$1.7 mW of 457.9-nm excitation incident on the $\sim$0.16cm^2

CdS:Te exposed surface area) were unchanged throughout these experiments,

the emissive intensities pictured are directly comparable. [Reprinted

from reference 48 with permission].

Figure 9. Uncorrected PL spectra of homogeneous, single-crystal CdS$_X$Se$_{1-X}$

samples irradiated in 5M OH$^-$ electrolyte while they were held at -1.50 V

vs. SCE; similar spectra are observed in air. Curves 1-5 correspond

to X = 1.00, 0.74, 0.49, 0.11, and 0.00, respectively. The $\sim$0.25-cm^2

samples were excited with $\sim$1.0 mW of 457.9-nm light (excitation spike

shown at 1/100 the scale of the PL spectrum). Emission intensities are

not directly comparable because of differences in geometry. [Reprinted

from reference 26 with permission].

Figure 10. Plot of the PL band maxima of Figure 9 vs. composition, X,

of the CdS$_X$Se$_{1-X}$ samples. [Reprinted from reference 53 with permission].

Figure 11. Uncorrected, front-surface PL spectra of n-CdSe obtained in air with

632.8-nm (solid line) and 457.9-nm (dashed line) excitation. Both spectra

were taken in identical sample and excitation beam geometries; the $\sim$0.20-cm^2

surface area was excited with 5.0 and 15 mW of 632.8- and 457.9-nm light,

respectively, delivered in laser beams of $\sim$0.03-cm^2 area. The emission

intensity from 457.9-nm excitation was $\sim$2 times larger but has been scaled

Figure 11 continued

down to match the intensity from 632.8-nm light at $\lambda_{max} \sim 720$ nm.

A spectral resolution of 0.3 nm was employed, as illustrated by

the 632.8-nm excitation spike which is shown at 1/200 of the

sensitivity used for the corresponding emission band. [Reprinted from

reference 52 with permission].

Figure 12. Corrected, polarized PL spectra of n-CdSe a- and c- plates,

top and bottom panels, respectively. Samples were excited with ~ 13 mW/cm^2

of linearly-polarized 514.5-nm light; for the a- plate, this light was

polarized with $E \perp a,c$. The position of the polarizer for each spectrum

is indicated in the figure. [Reprinted from reference 71 with permission.]

Figure 13. Band structure and corresponding symmetries for n-CdSe at

k = (0,0,0). Band-to-band transitions involving Γ_9 and Γ_7 are allowed

only for $E \perp c$, whereas those involving two Γ_7 bands are allowed for

both $E \perp c$ and $E \parallel c$. Energetic separations between bands are indicated

at the left-hand side of the diagram. [Adapted from ref. 58 and

reprinted from reference 71 with permission]..

Figure 14. Photocurrent (solid lines, left-hand scales) and emission

intensity (dashed lines, right-hand scales) monitored at emission

band maxima for single-crystal CdS$_x$Se$_{1-x}$ electrodes in 1M OH$^-$/1M S^{2-}/0.1M S

electrolyte as a function of potential. The electrodes (~ 0.25-cm^2 exposed

area) were excited with ~ 1.0-1.2 mW of 457.9-nm light from a beam-expanded

Ar ion laser. These iLV curves were swept at 10 mV/s. The electrolyte

redox potential was -0.78 V vs. SCE. [Reproduced from reference 53

with permission].

Figure 15. Scheme describing the dead-layer model for PL quenching. Symbols

are defined in the text.

Figure 16. Relative photocurrent (bottom panel) and PL intensity (top panel)
for two n-GaAs electrodes as a function of potential in PEC's employing
ditelluride electrolyte; the electrodes were excited with 514.5-nm
light and their PL signals were monitored at $\lambda_{max} \sim 870$ nm. The solid
curves correspond to electrode no. 5 (cf. Table IV) with n $\sim 0.7-1 \times 10^{16}$ cm^{-3}
and a surface area of ~ 0.18 cm^2; a current density at -1.0 V vs. SCE
of 4.2 mA/cm^2 was measured ($\phi_X = 0.69$). Dashed curves correspond to
electrode no. 2 (cf. Table IV) with n $\sim 1 \times 10^{18}$ cm^{-3} and a surface area
of ~ 0.30 cm^2; the current density at -1.0 V vs. SCE was ~ 1.5 mA/cm^2
($\phi_X = 0.69$). Photocurrents for the two electrodes are relative to
values at -1.0 V vs. SCE which have been arbitrarily set at 100; PL
intensities are likewise relative to open circuit values of 100. The
iLV curves for each electrode were swept simultaneously at 10 mV/s. The
electrolyte redox potential, the short-circuit potential, is -1.13 V vs. SCE.
[Reprinted from reference 89 with permission].

Figure 17. Relative photocurrent (bottom panel) and PL intensity (top panel)
as a function of potential and excitation wavelength for an n-GaAs-based
PEC employing ditelluride electrolyte; PL intensity was monitored at
$\lambda_{max} \sim 870$ nm. Electrode no. 4 with n $\sim 4 \times 10^{16}$ cm^{-3} (cf. Tables IV and V)
was sequentially irradiated in these experiments by 457.9-, 514.5-, and
632.8-nm light, yielding curves A, B, and C, respectively. PL intensities
are relative to open-circuit values which have been arbitrarily set at
100 for all three excitation wavelengths. Photocurrents are relative
to their values at -1.0 V vs. SCE which have also been arbitrarily set
at 100. Photocurrent densities at -1.0 V vs. SCE from 457.9-, 514.5-
and 632.8-nm light were 4.7, 4.3, and 8.6 mA/cm^2, respectively, with
corresponding calculated ϕ_X values of 0.76, 0.67, and 0.75; the electrode
surface area was 0.20 cm^2. The iLV curves for each excitation wavelength

Figure 17 continued

were swept simultaneously at 10 mV/s. The electrolyte redox potential

was -1.13 V vs. SCE. [Reprinted from reference 89 with permission].

Figure 18. Observed (solid curve) and calculated (dashed curve) PL

intensity as a function of potential for an n-GaAs-based PEC. The

observed curve is that labeled A in Figure 17 and corresponds to

electrode no. 4 with n $\sim 4 \times 10^{16}$ cm^{-3} excited by 457.9-nm light. The

calculated curve was obtained by using the dead-layer model and assuming

that the dead-layer thickness is proportional to the depletion width,

as described in the text. [Reprinted from reference 89 with permission].

Figure 19. Photocurrent (bottom panel) and relative PL intensity (top panel)

as a function of potential and wavelength for an n-CdTe-based

PEC employing ditelluride electrolyte; PL intensity was monitored at

λ_{max} ~ 830 nm. The solid and dashed PL intensity-V curves were obtained with

514.5- and 620-nm excitation, respectively. PL intensities

are relative to open circuit values which have been arbitrarily set

at 100 for both excitation wavelengths. Virtually superimposable i-V

curves were obtained for these excitation wavelengths. The electrode

surface area was ~ 0.15 cm^2. Incident intensities were 0.94 and 0.90 mW

for 514.5- and 620-nm excitation, respectively. PL-V and i-V curves

were swept simultaneously at 10 mV/s. The electrolyte redox potential

was -1.15 V vs. SCE.

Figure 20. Photocurrent (bottom panel) and relative PL intensity (top panel)

for an n-CdTe electrode as a function of potential in a PEC

employing a 14 mM ferrocene/0.5 mM ferricenium redox couple in aceto-

nitrile; the electrode was excited with 514.5-nm light and the PL signals

were monitored at λ_{max} ~ 830 nm. The solid curves were obtained

subsequent to treating the n-CdTe electrode with a reducing etch while

Figure 20 continued

the dashed curves were obtained subsequent to an oxidizing etch. PL

intensities are relative to open-circuit values which have been

arbitrarily set at 100 for both experiments. The electrode surface

area was ∿0.15 cm^2. Incident intensities were 1.9 and 3.5 mW for the

solid and dashed curves, respectively. A reference electrode consisting

of Ag/0.01M Ag$^+$/0.2M TBAP in acetonitrile was used (+0.33 V vs. SCE).

The electrolyte redox potential was ∿+0.014 V vs. Ag/Ag$^+$.

Figure 21. Corrected, front-surface PL spectra of n-ZnSe:Al at 295 K (dashed

line) and 77 K (solid line). Both spectra were taken at the same

sensitivity (a 100-fold increase in sensitivity was used in scanning

the 410-480-nm region). The sample was excited with identical

intensities of 405-nm light without disturbing the experimental geometry.

[Reprinted from reference 104 with permission].

Figure 22. Transistor-like device for the detection of hole injection

or extraction; CE represents the counterelectrode. The current through

the reverse-biased p-n junction is limited by the concentration of holes

(minority carriers) in the n-type material. Hole injection or extraction

at the semiconductor-electrolyte interface will raise or lower the

magnitude of the current through the p-n junction, respectively. Adapted

from reference 6.

Figure 23. Mechanism for EL in peroxydisulfate electrolyte as proposed in

refs. 34, 127, and 128. Filled and open circles represent electrons

and holes, respectively. [Reprinted from reference 21 with permission].

Figure 24. (a) Uncorrected EL spectrum of a 100-ppm CdS:Te electrode obtained in

5M KOH/0.1 M $K_2S_2O_8$ electrolyte. The electrode was continuously

pulsed between 0.0 V (11 sec) and -1.8 V vs. SCE (1 sec) while the

emission was scanned at 12 nm/min. A maximum current density of

39.4 mA/cm^2 was measured at -1.8 V vs. SCE throughout the scan.

(b) Uncorrected PL spectrum of the same sample in

air (curve 1) and out of circuit but immersed in the peroxydisulfate

electrolyte used for the EL experiment (curve 2). The sample was

excited with the 457.9-nm line ($\sim$5 mW/cm^2) of an Ar ion laser

(excitation spike is shown at 1/100 the scale of the PL spectrum);

scattered laser light accounts for the loss of baseline at the high-

energy extreme of the PL spectrum. Sample geometry is identical in

curves 1 and 2 but differs from that used in (a). [Reprinted from

reference 136 with permission].

Figure 25. Uncorrected PL (solid curve) and EL (vertical lines) spectra of

CdSe obtained in the same sample geometry. The PL spectrum was taken

with the CdSe electrode immersed in 5M NaOH electrolyte at -1.50 V vs. SCE.

An Ar ion laser whose beam was expanded and masked to fill the $\sim$0.30-cm^2

electrode surface was used for excitation; 0.4 mW of 514.5-nm light was

delivered to the electrode. The EL spectrum was taken in 5M NaOH/0.1 M

$K_2S_2O_8$ electrolyte. The electrode was continuously pulsed between 0.0 V

(11s) and -1.50 V vs. SCE (1s) while the emission spectrum was scanned

at 6 nm/min. For both EL and PL a spectral resolution of 0.3 nm was

employed. The EL spectrum has been scaled down to match the PL intensity at

λ_{max} $\sim$720 nm. [Reprinted from reference 52 with permission].

Figure 26. Auger/depth profile analysis of a graded CdS_xSe_{1-x} sample

(CdSe/S) with an $\sim$1-μm thick graded zone, prepared as described

in the text. Sputter etching employed Ar ions and was conducted

at a rate of $\sim$300 Å/min. [Reprinted from reference 27 with permission].

Figure 27. Uncorrected PL spectra of a graded CdS_xSe_{1-x} sample (CdSe/S)

with an $\sim$2-μm thick graded zone, prepared as described in the text.

All spectra were obtained in air with 457.9-nm excitation. Curve 1

is the PL spectrum of the as-grown sample and curves 2-5 are spectra

obtained after successive chemical etchings with a Br_2/H_2O solution

(1:1000 v/v) of 0.5, 3.0, 4.5 and 16 min, respectively. The $\sim$0.3-cm^2

exposed surface area of the sample was uniformly irradiated with

$\sim$1.5 mW of power, and the excitation geometry was made as nearly

identical as possible throughout the experiment. [Reprinted from

reference 26 with permission].

Figure 28. PL spectra and i-V properties of a graded CdS_xSe_{1-x} sample

with an $\sim$1-μm thick graded zone. The inset shows i-V properties obtained

with 457.9-nm excitation of the electrode when incorporated in a PEC

employing 1M OH^-/1M S^{2-} electrolyte. The Ar ion laser beam used for

excitation uniformly irradiated the entire $\sim$0.15-cm^2 sample surface

area with $\sim$1.6 mW of power. A sweep rate of 10 mV/s was used and

the electrolyte redox potential was -0.71 V vs. SCE. Corresponding,

uncorrected PL spectra obtained at open circuit (-), -1.0 V (---) and

-0.3 V vs. SCE (-··-) are shown in the main panel of the figure. All

spectra were taken in an identical sample geometry. Similar data were

obtained in 1M OH^-/1M S^{2-}/0.1M S electrolyte. [Reprinted from

reference 27 with permission].

END

FILMED

DTIC
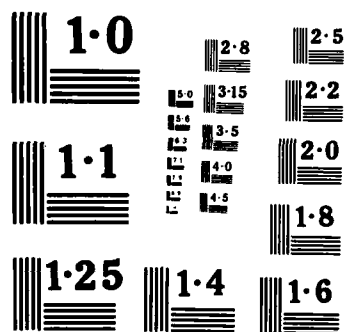
Figure 29. Uncorrected EL spectra of the graded CdS_xSe_{1-x} electrode of

Figure 26. The series of vertical lines which constitute the EL

spectra were obtained in 5M OH^-/0.1M $S_2O_8^{2-}$ electrolyte by repetitively

pulsing between 0.00 V (11s) and -1.30 V (top panel), -1.45 V (middle

panel) or -1.60 V (bottom panel) for 1s while scanning the emission

monochromator at 12 nm/min. The -1.3-V spectrum was obtained at both

the beginning and end of this experiment to demonstrate reproducibility.

All spectra were taken in an identical sample geometry; however, the

-1.45-V spectrum was taken at twice the sensitivity used to obtain

the -1.30- and -1.60-V spectra. [Reprinted from reference 27 with

permission].

Figure 30. PL spectra and i-V properties of a graded CdS/Se sample with an

$\sim$1-μm thick graded zone, prepared as described in the text. The inset

shows i-V properties obtained with 457.9-nm "frontside" excitation

of the electrode ($\sim$0.25-cm^2 exposed surface area) when incorporated

in a PEC employing 1M OH^-/1M S^{2-}/0.01M S electrolyte. A sweep rate of

10 mV/s was used and the electrolyte redox potential was -0.73 V vs. SCE.

Corresponding, uncorrected PL spectra obtained at open circuit (——) and

-0.3 V vs. SCE (---) are shown in the main panel of the figure. Both

spectra were taken in identical geometries. [Reprinted from reference 29

with permission].

Figure 31. Uncorrected PL spectra obtained with "backside" illumination

and viewing of the same CdS/Se electrode as in Fig. 30 in

the same PEC. The sample was excited with 570-nm

light. The solid curve corresponds to PL obtained at open circuit

and the dashed curve to PL at -0.3 V vs. SCE and a

current density of $\sim$0.2 mA/cm^2. Both spectra were taken in identical geometries.

The cut-off filter used to reject excitation light blocked PL at wavelengths

$\lesssim$ 600 nm. [Reprinted from reference 29 with permission].

Figure 32. Schematic of graded CdS/Se sample etched in a spatially-controlled

fashion to yield patterned, multi-colored emission when used as an

electrode. The color each exposed composition will emit in an EL experiment

is indicated. [Reprinted from reference 29 with permission].

Figure 33. PL spectra and i-V properties of the isotype heterojunction

electrode described in the text. The inset shows i-V properties obtained with

457.9-nm   excitation of the electrode when incorporated in a PEC

employing ditelluride electrolyte. The Ar^+ laser beam

was   expanded to irradiate the ~ 0.25-cm^2 exposed sample area with

~ 0.7 mW of power. A sweep rate of 10 mV/s was used and the electrolyte

redox potential (short circuit) was -1.15 V vs. SCE. Corresponding,

uncorrected PL spectra obtained at open circuit, -1.7 V vs. SCE, and

-1.0 V vs. SCE are shown as the solid, dashed, and dot-dashed curves,

respectively. All spectra were taken in an identical geometry.

[Reprinted from reference 28 with permission].

Figure 34. Schematic of the isotype heterojunction electrode described

in the text. The partitioning of incident light by a dead-layer

model is shown and discussed in the text. [Reprinted from reference

28 with permission].

Figure 35. Uncorrected EL spectrum of the electrode of Fig. 33. The

series of vertical lines constituting the spectrum was obtained in

dry, N_2-blanketed 0.5M $Na_2S_2O_8$ formamide electrolyte by repetitively

pulsing between -1.1 V (5.5 s) and -3.2 V vs. a CH_3CN Ag/Ag^+ reference

electrode (0.5 s) while scanning the emission monochromator at 12 nm/min.
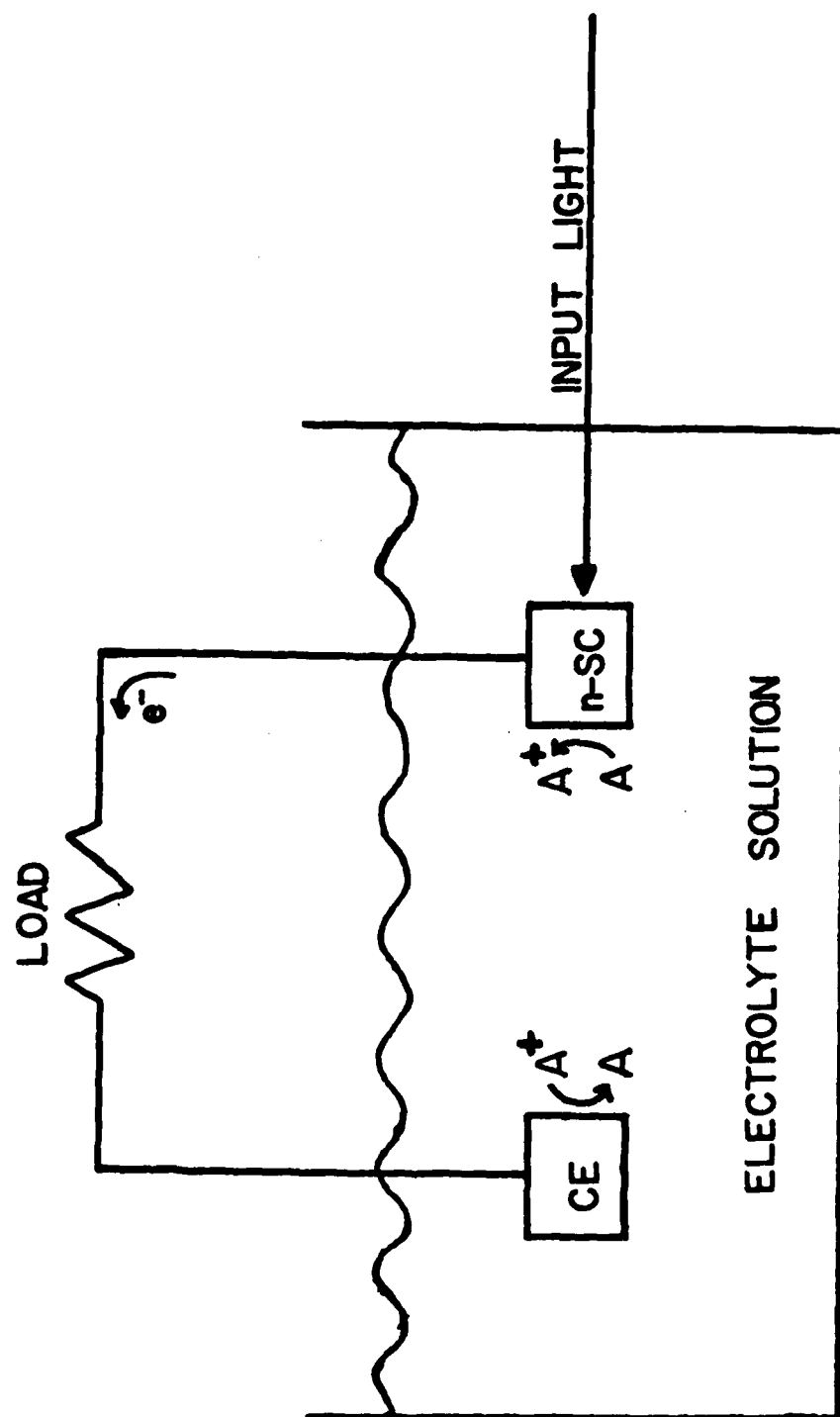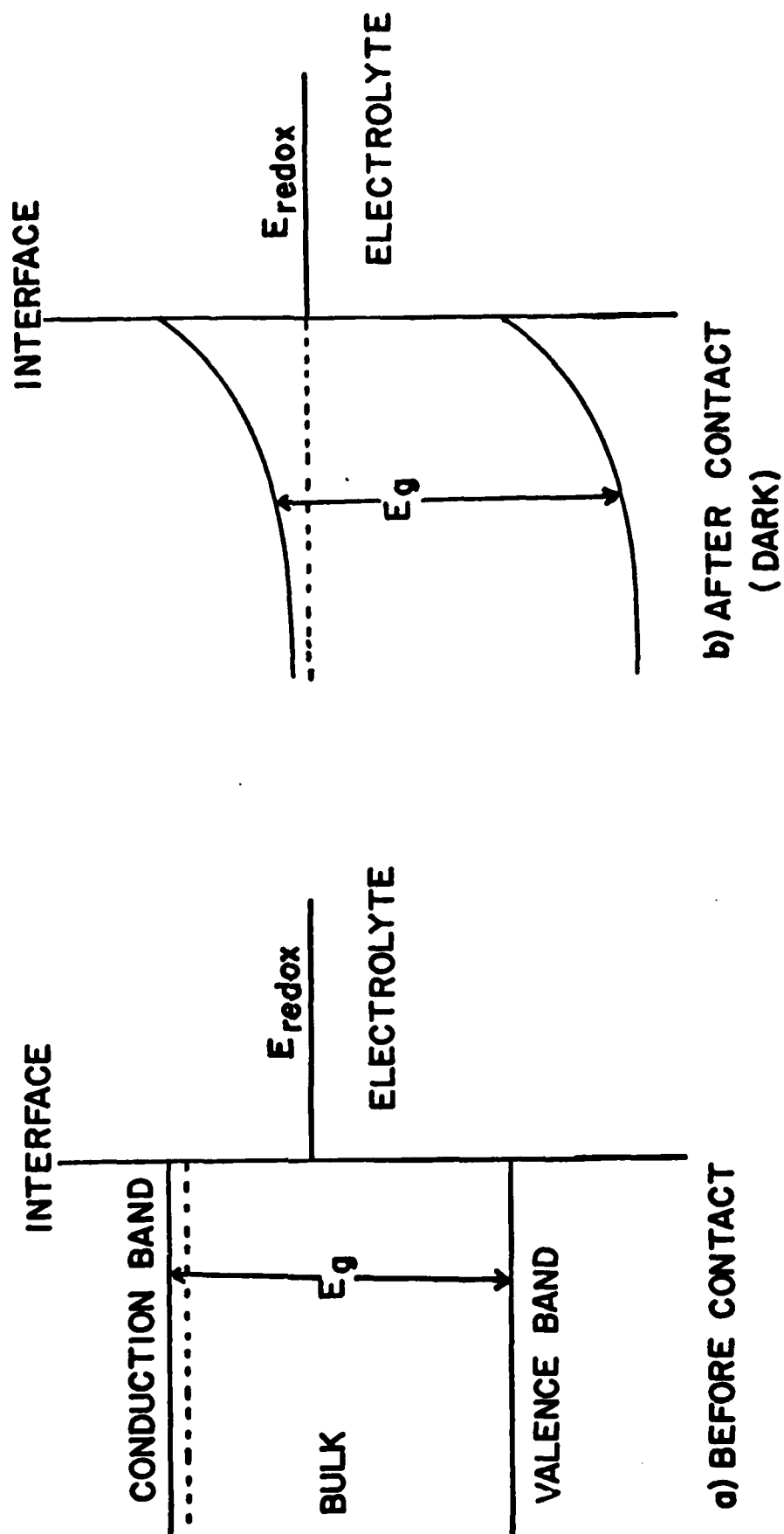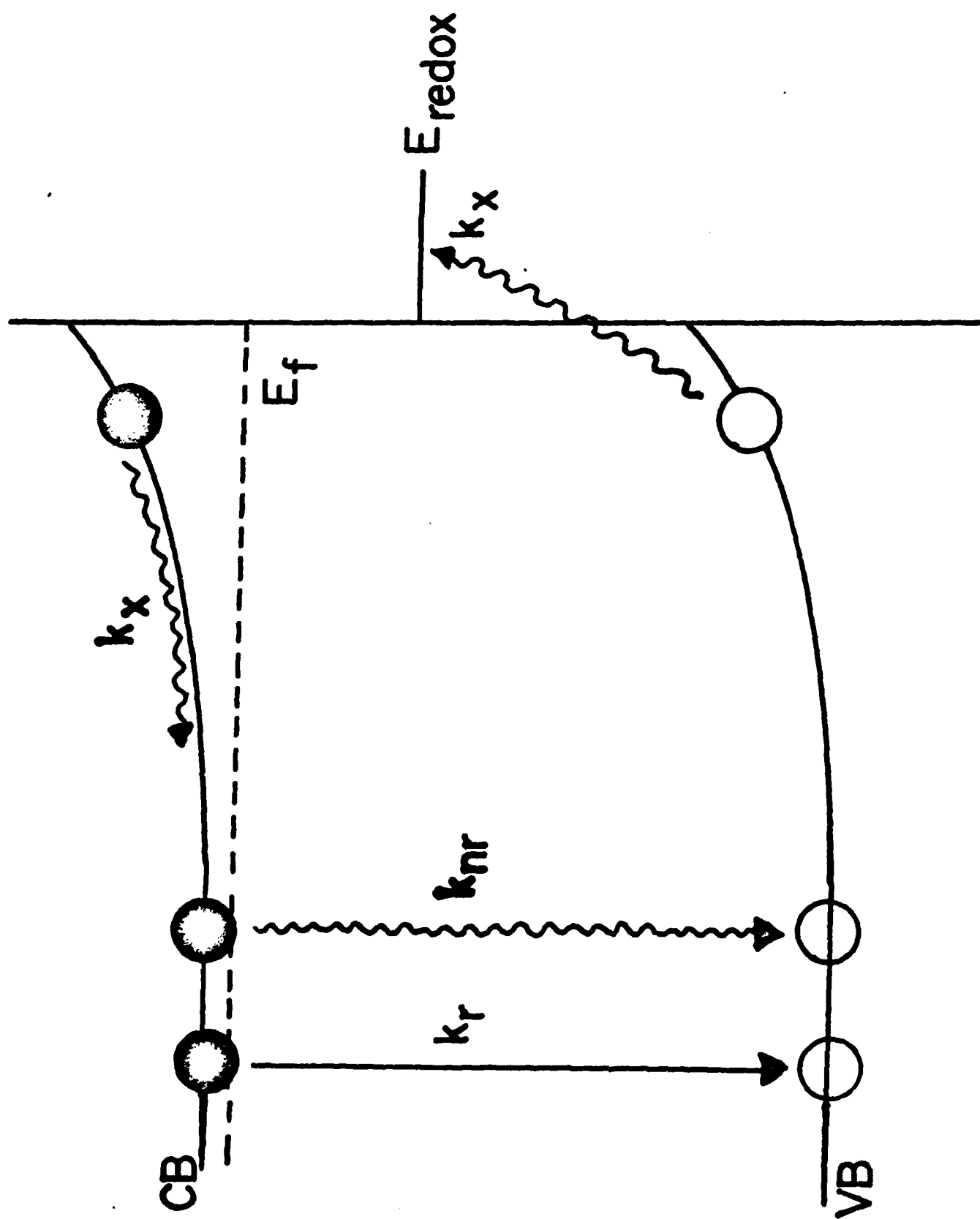
LOAD

INPUT LIGHT

n-SC

CE

ELECTROLYTE SOLUTION

93

n-TYPE SEMICONDUCTOR

a) BEFORE CONTACT

b) AFTER CONTACT (DARK)

Figure 1

RELATIVE EMISSION INTENSITY, a.u.

WAVELENGTH, nm

Figure 2.

PHOTOCURRENT, MICROAMPS

RELATIVE EMISSION INTENSITY, a.u.

POTENTIAL, VOLTS vs. SCE
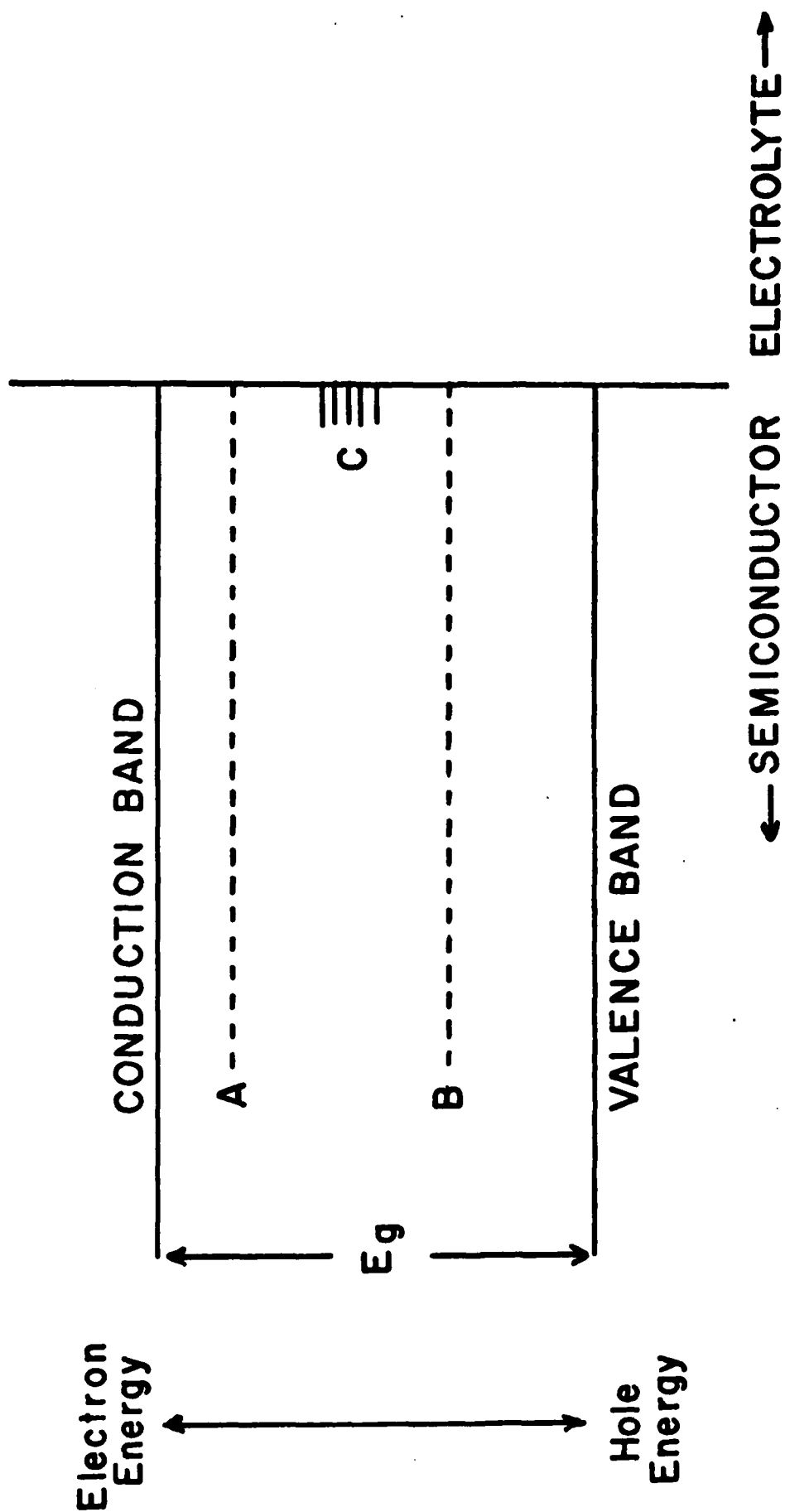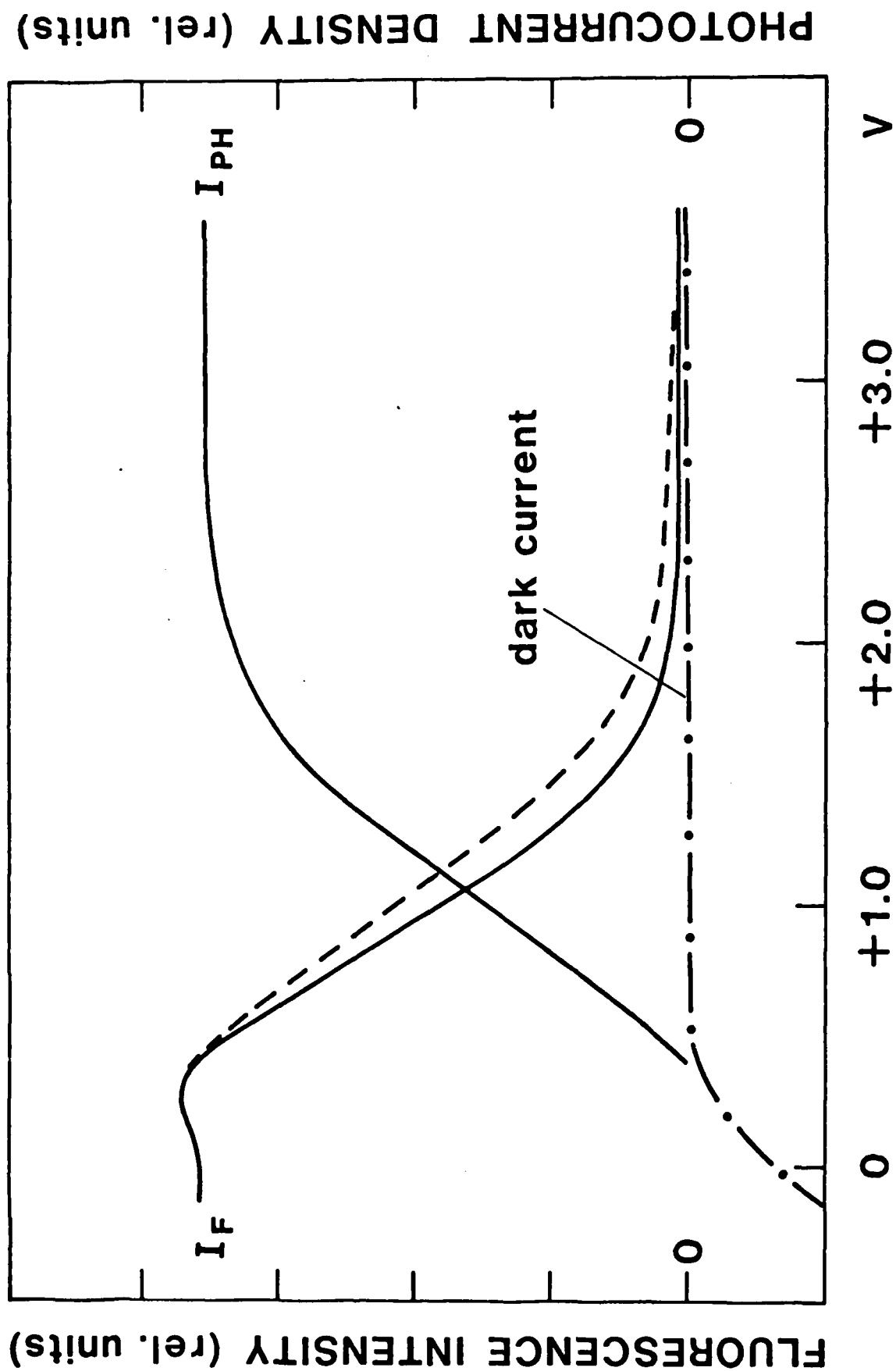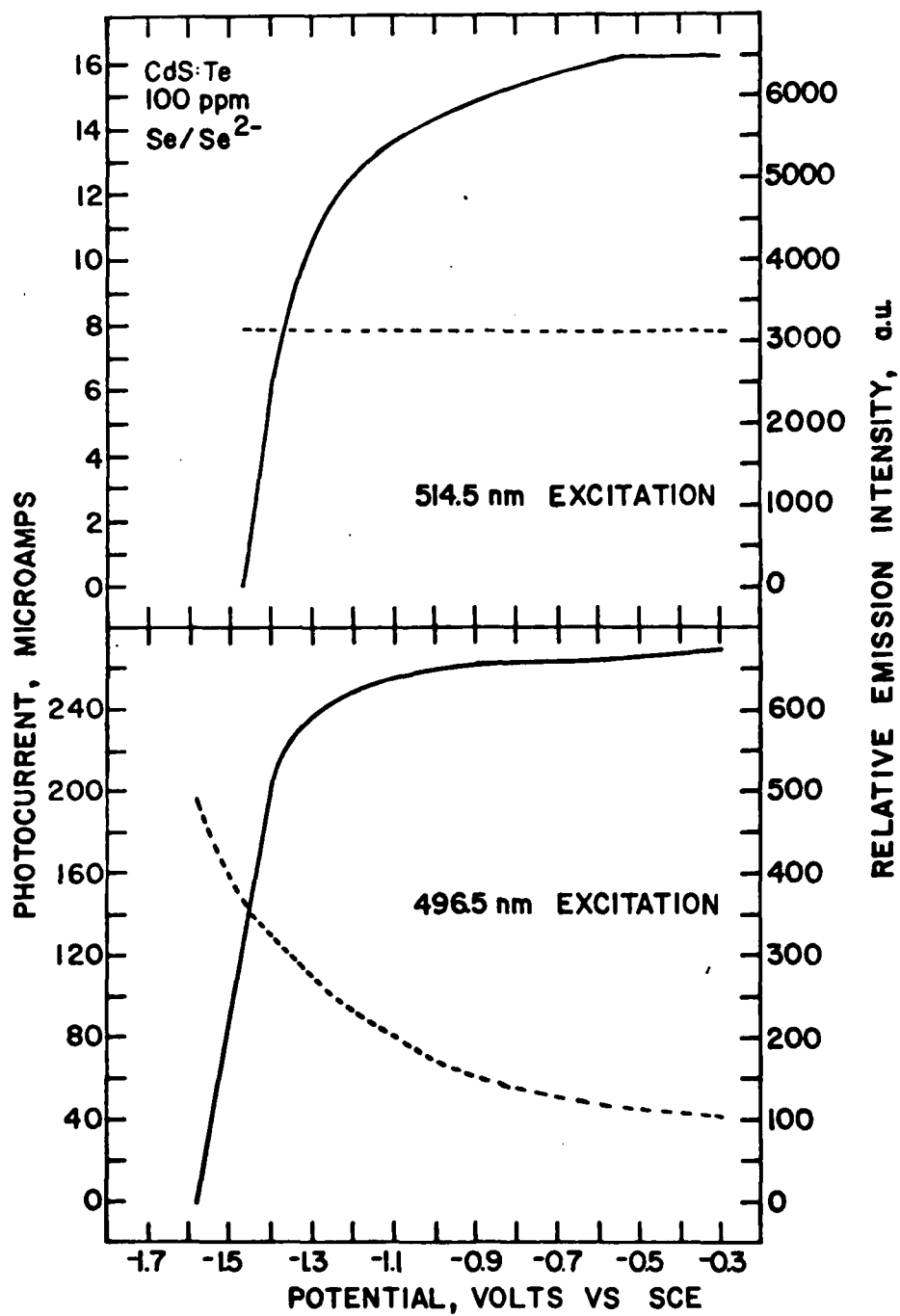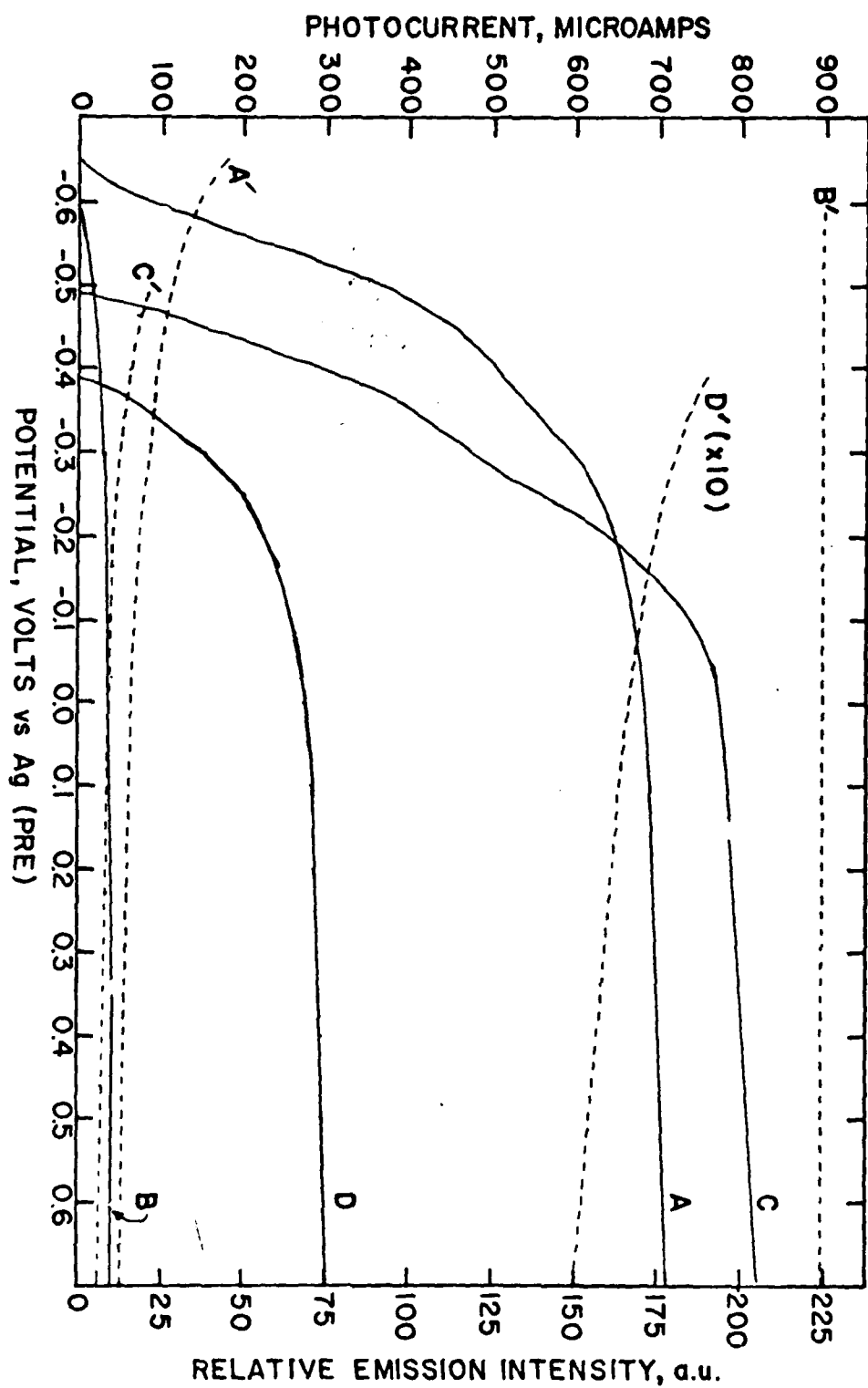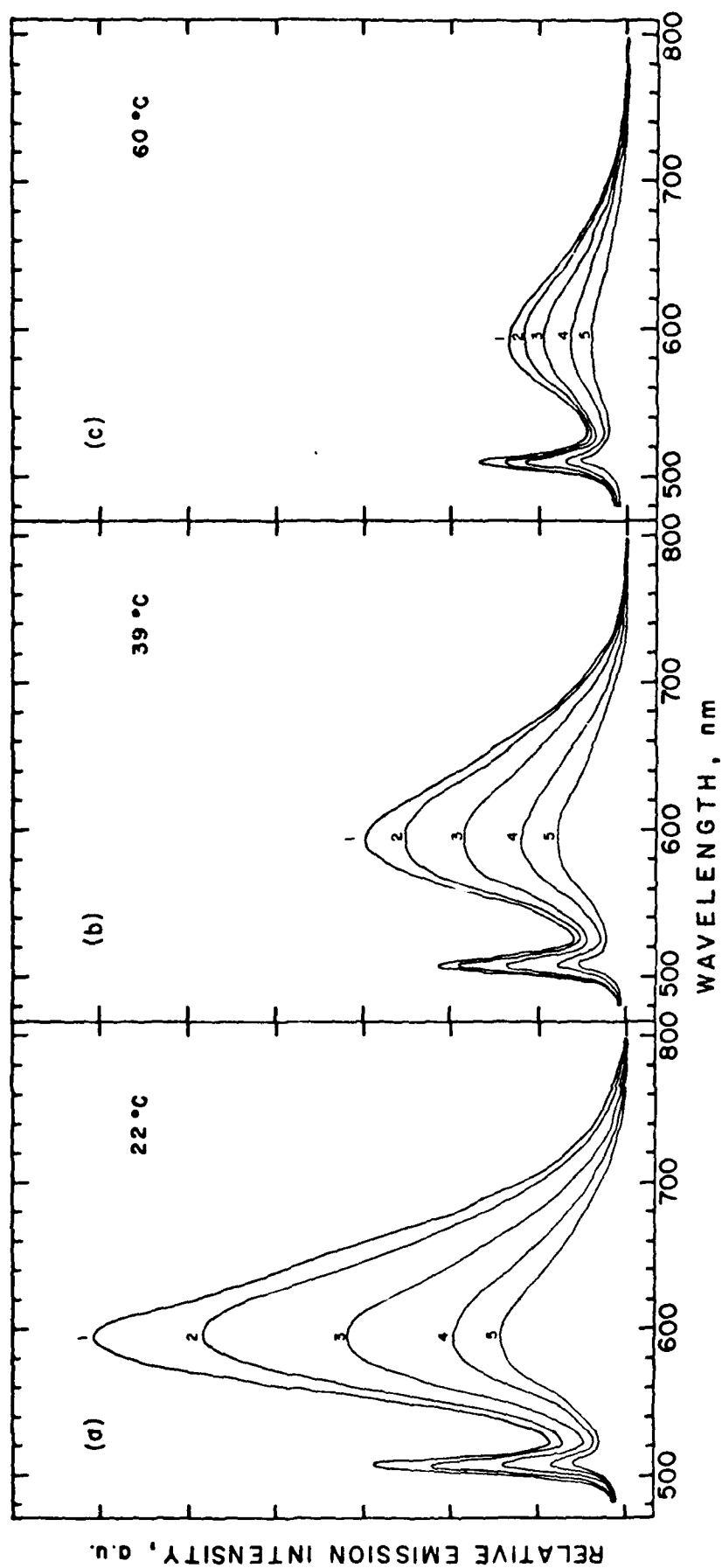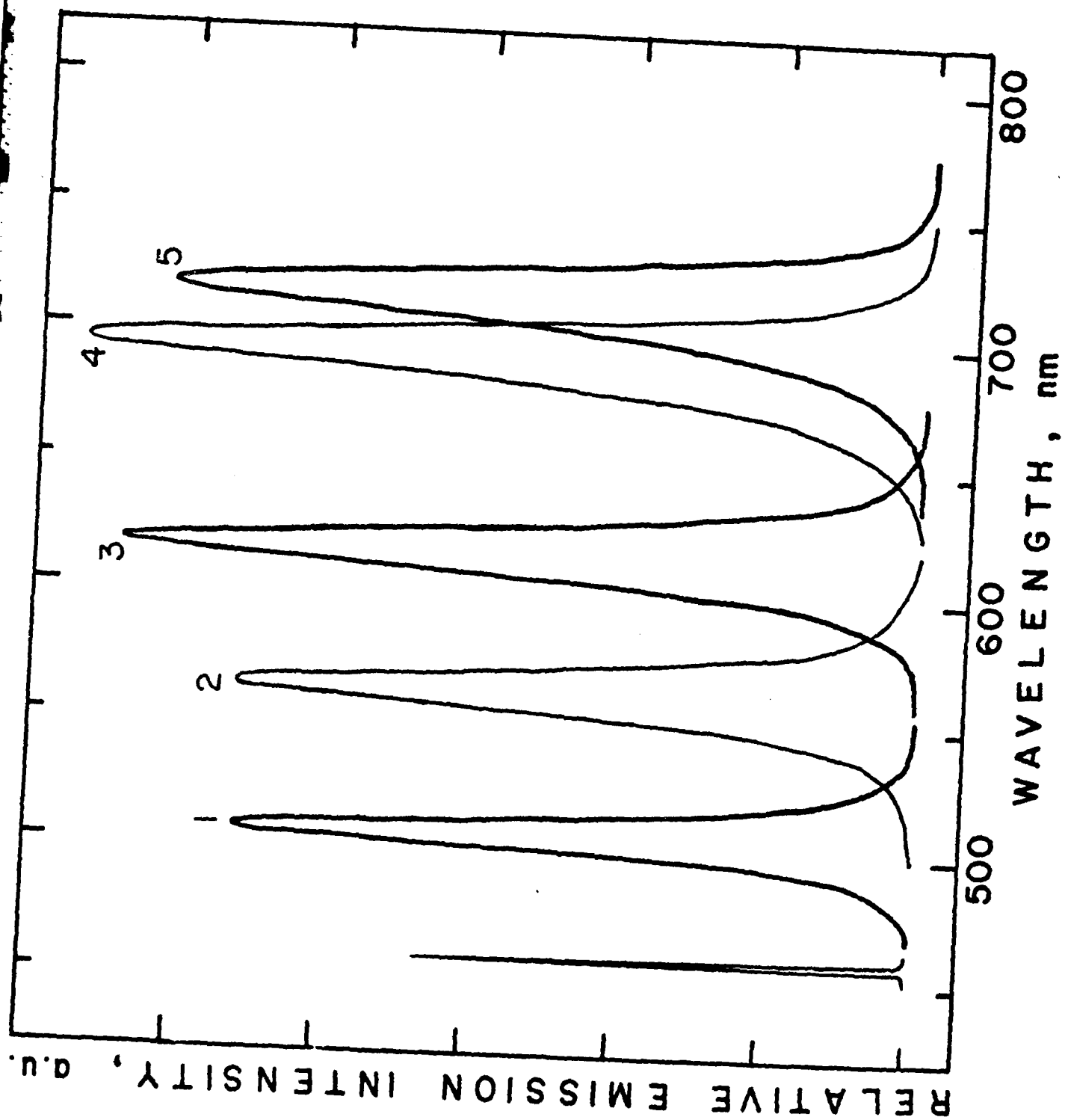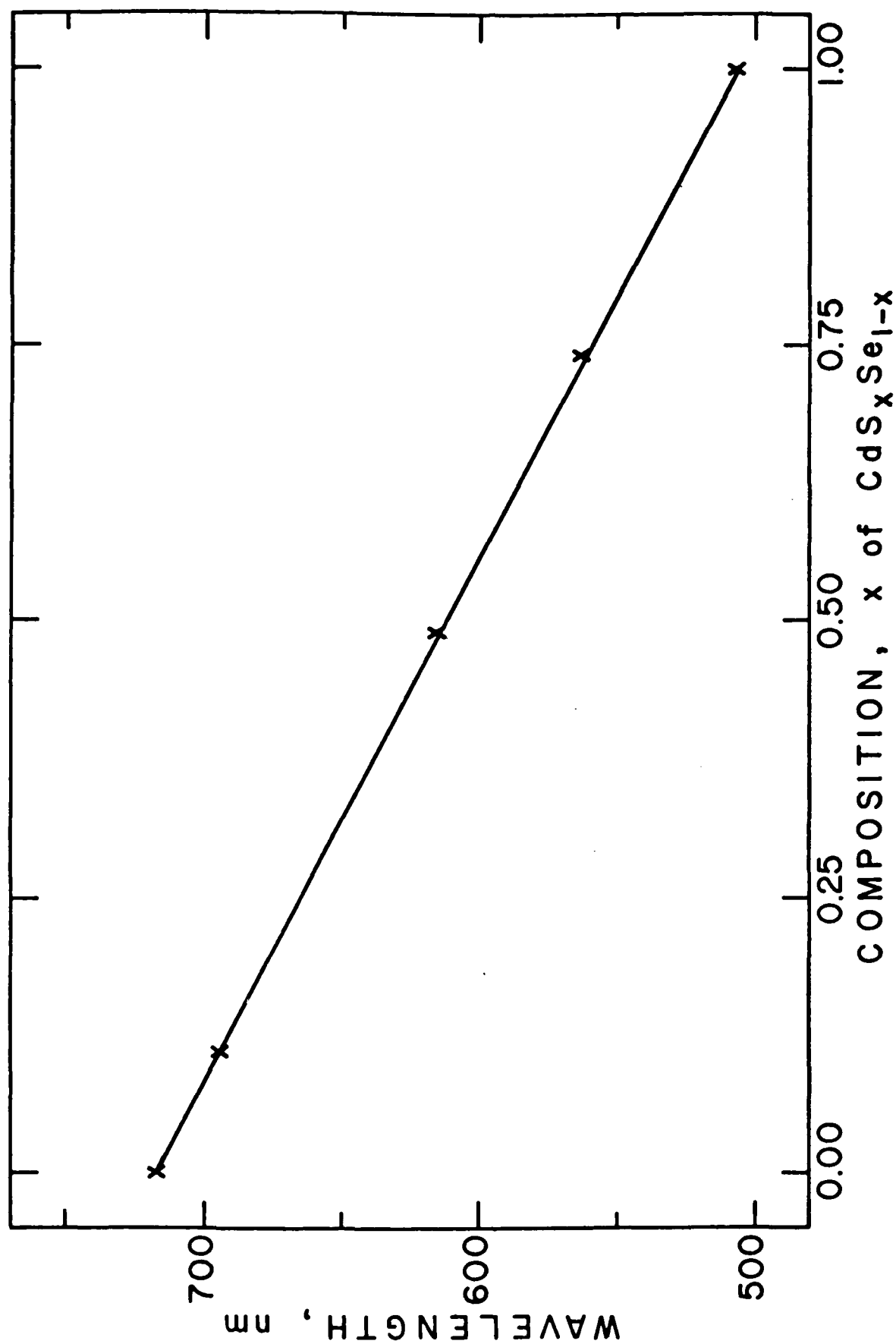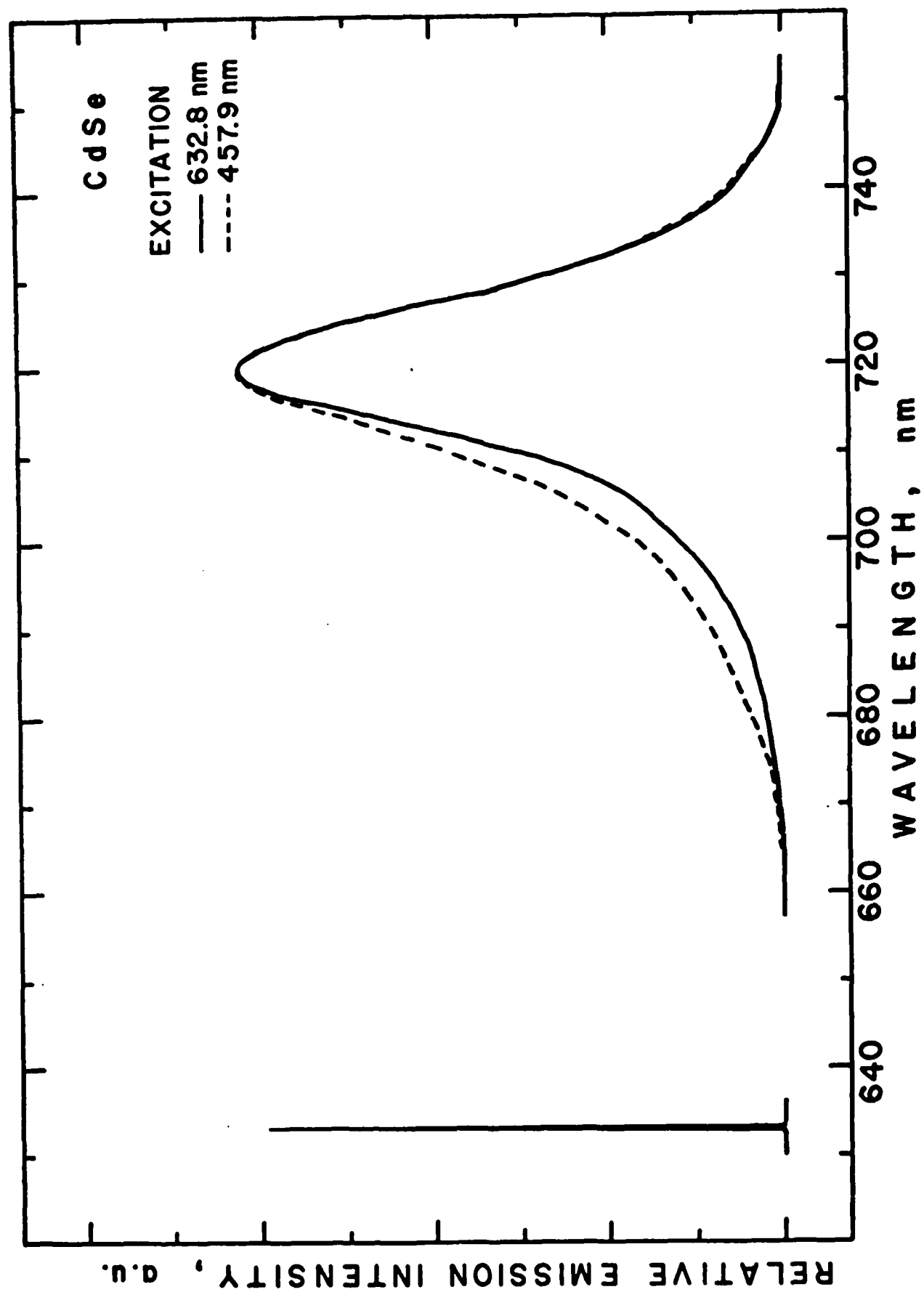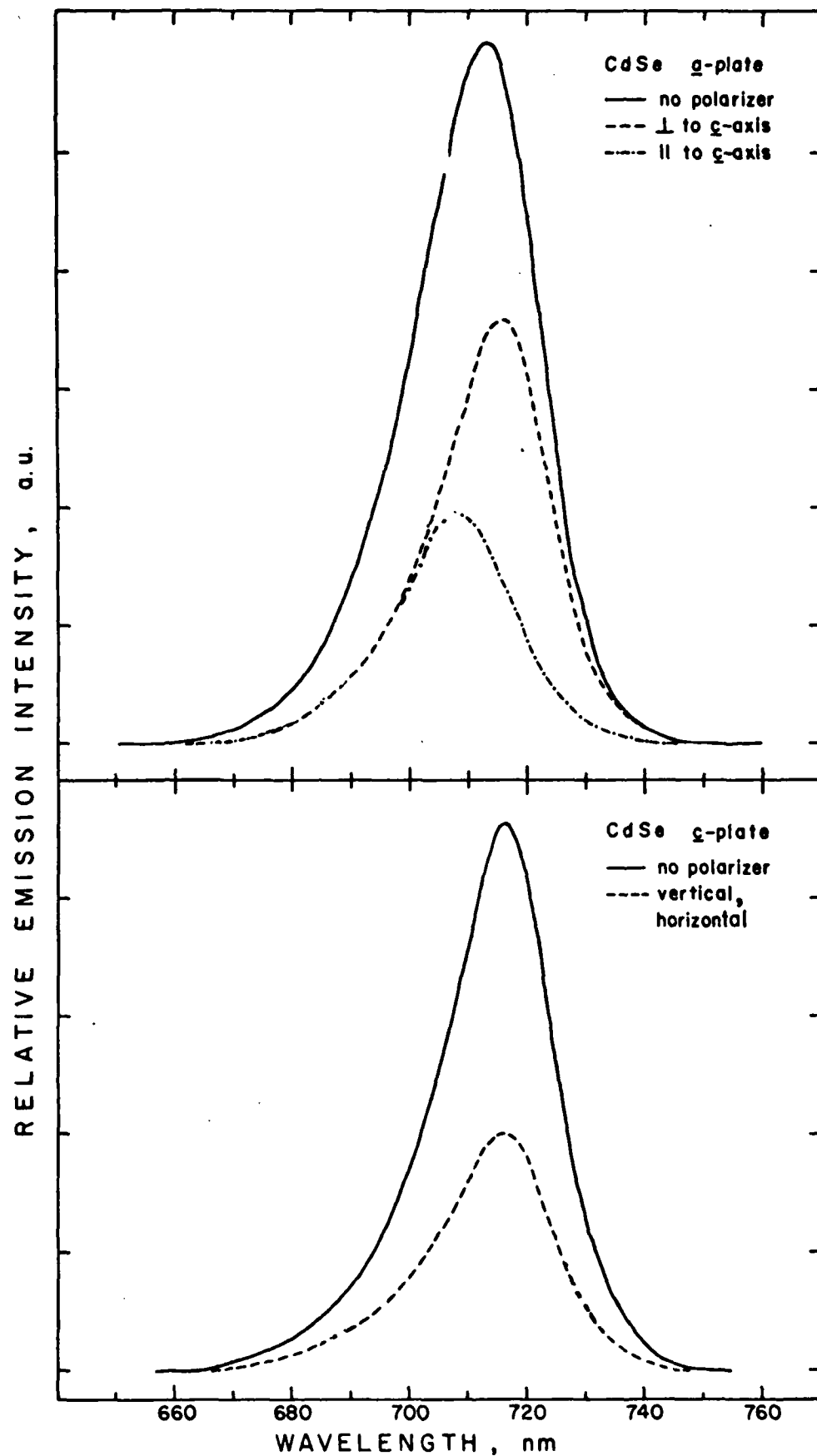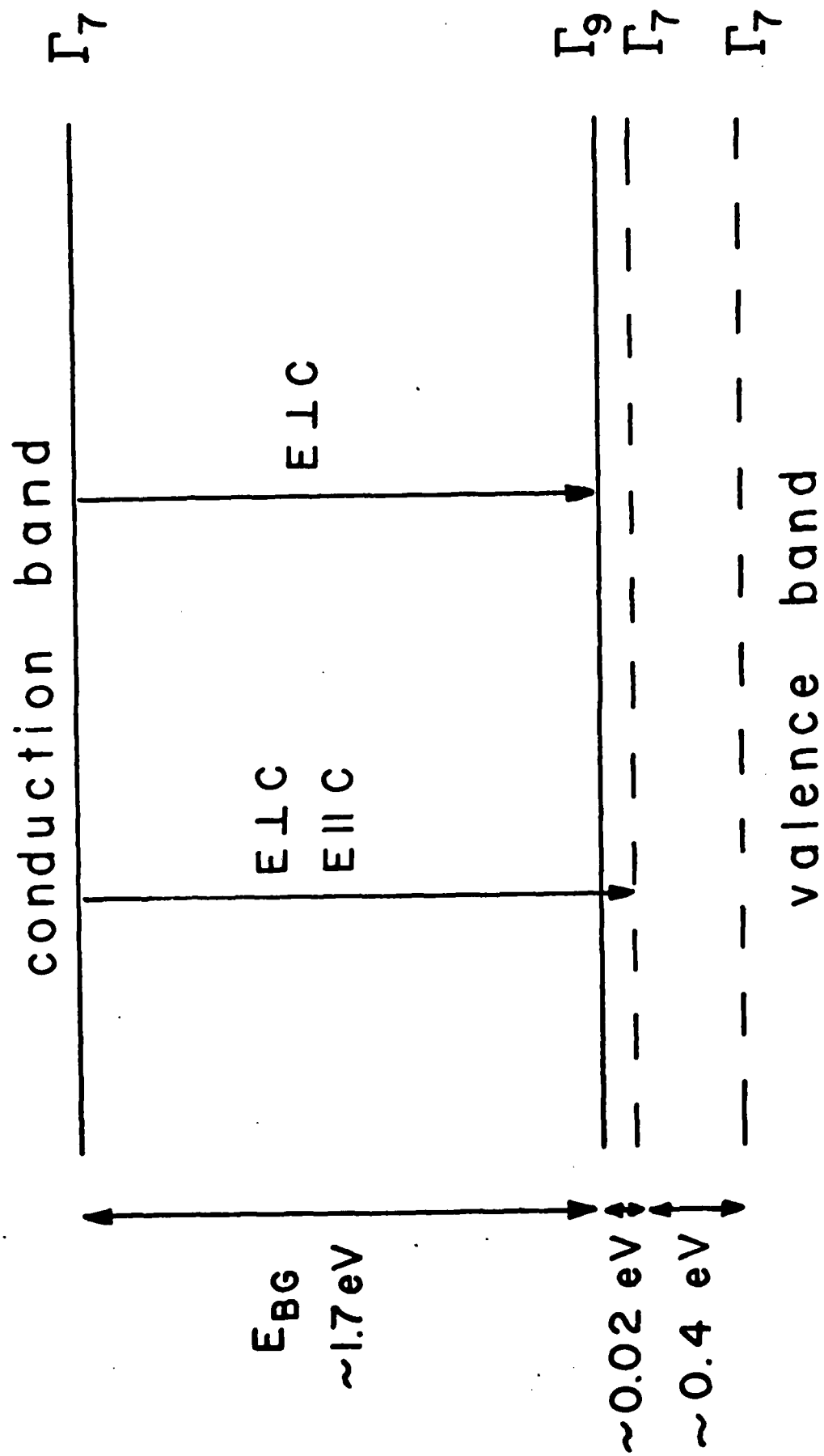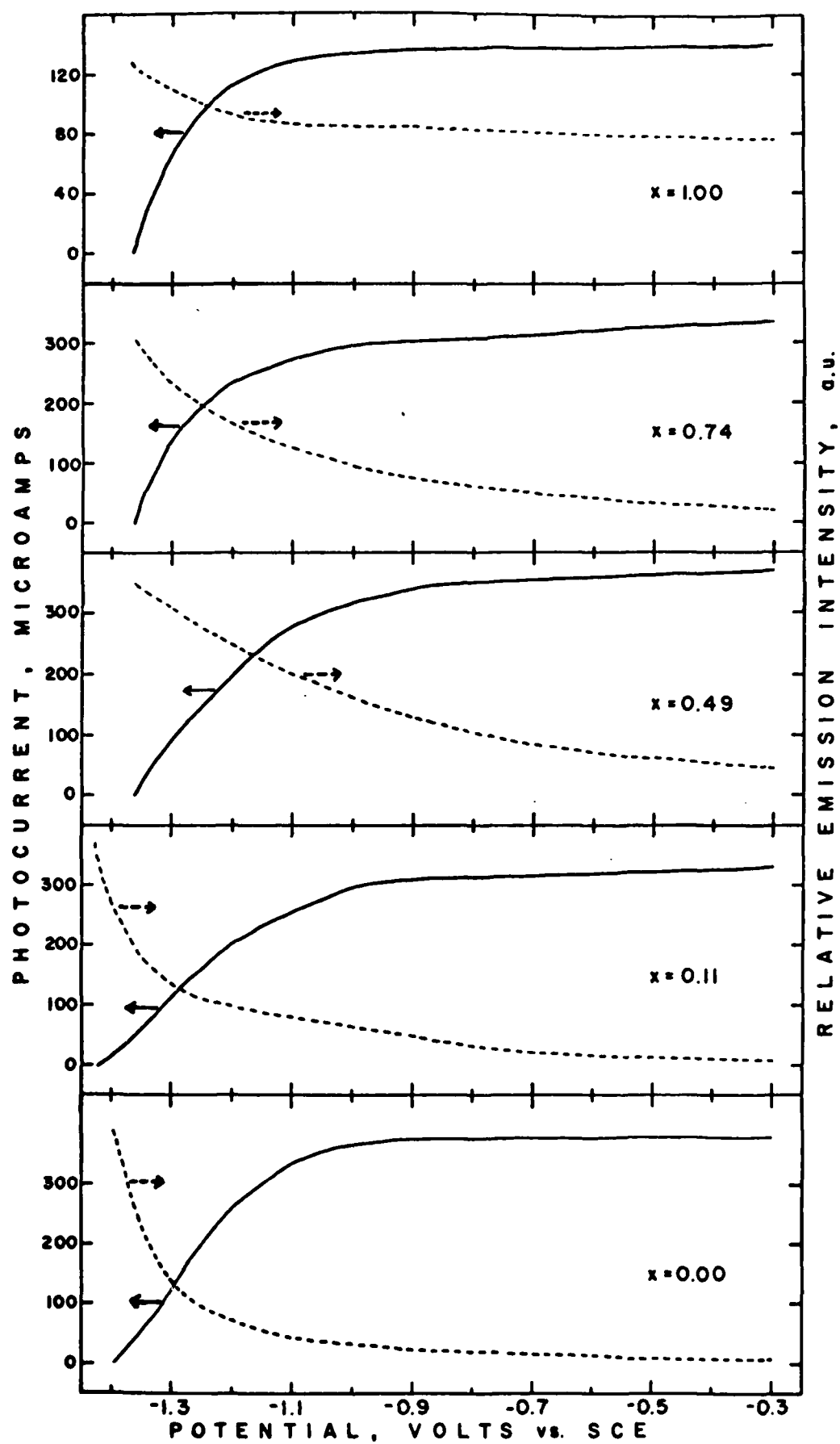
THE DEAD-LAYER MODEL

Flat-Band Potential

CB

I_0

VB

PL Intensity (PL_{FB}) proportional to I_0

In-Circuit Potentials

CB

$I_0 \exp(-\alpha'D)$

I_0

VB

D

PL Intensity (PL) proportional to

$I_0 \exp(-\alpha'D)$
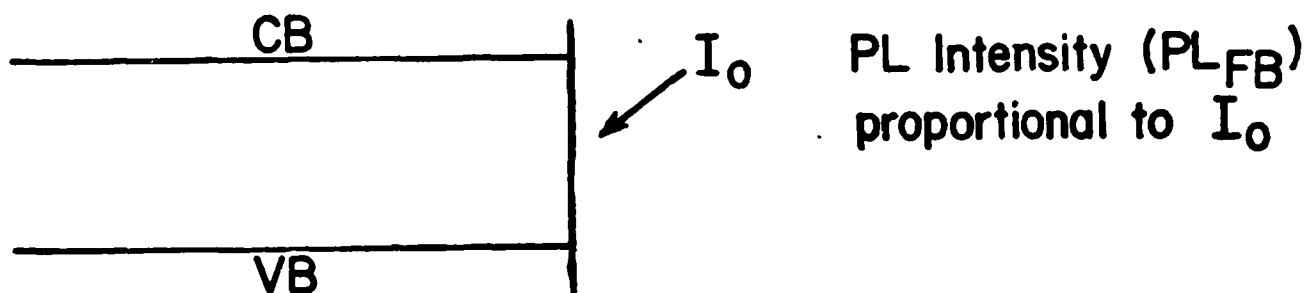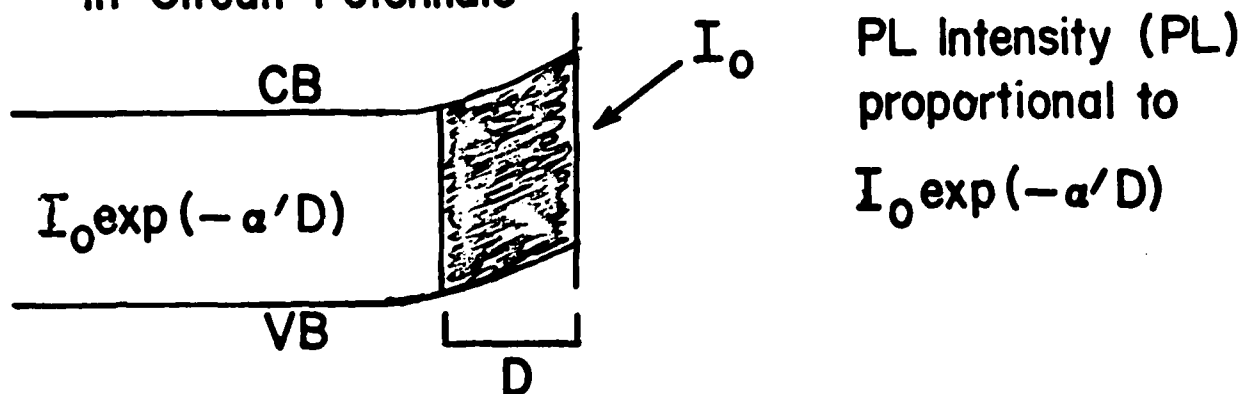
← n-semiconductor   electrolyte →

$$\frac{PL}{PL_{FB}} = \exp(-\alpha'D)$$
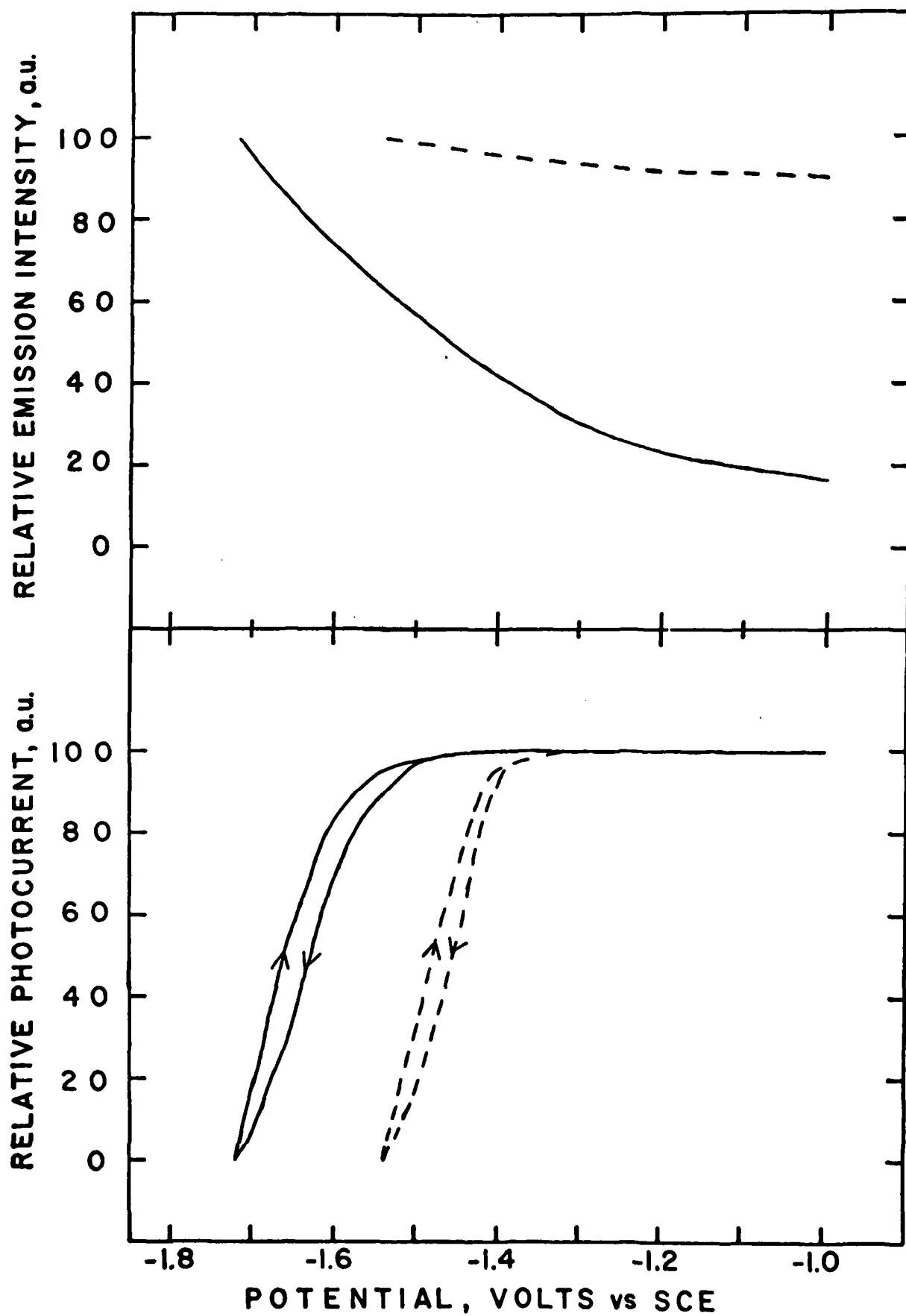
RELATIVE EMISSION INTENSITY, a.u.
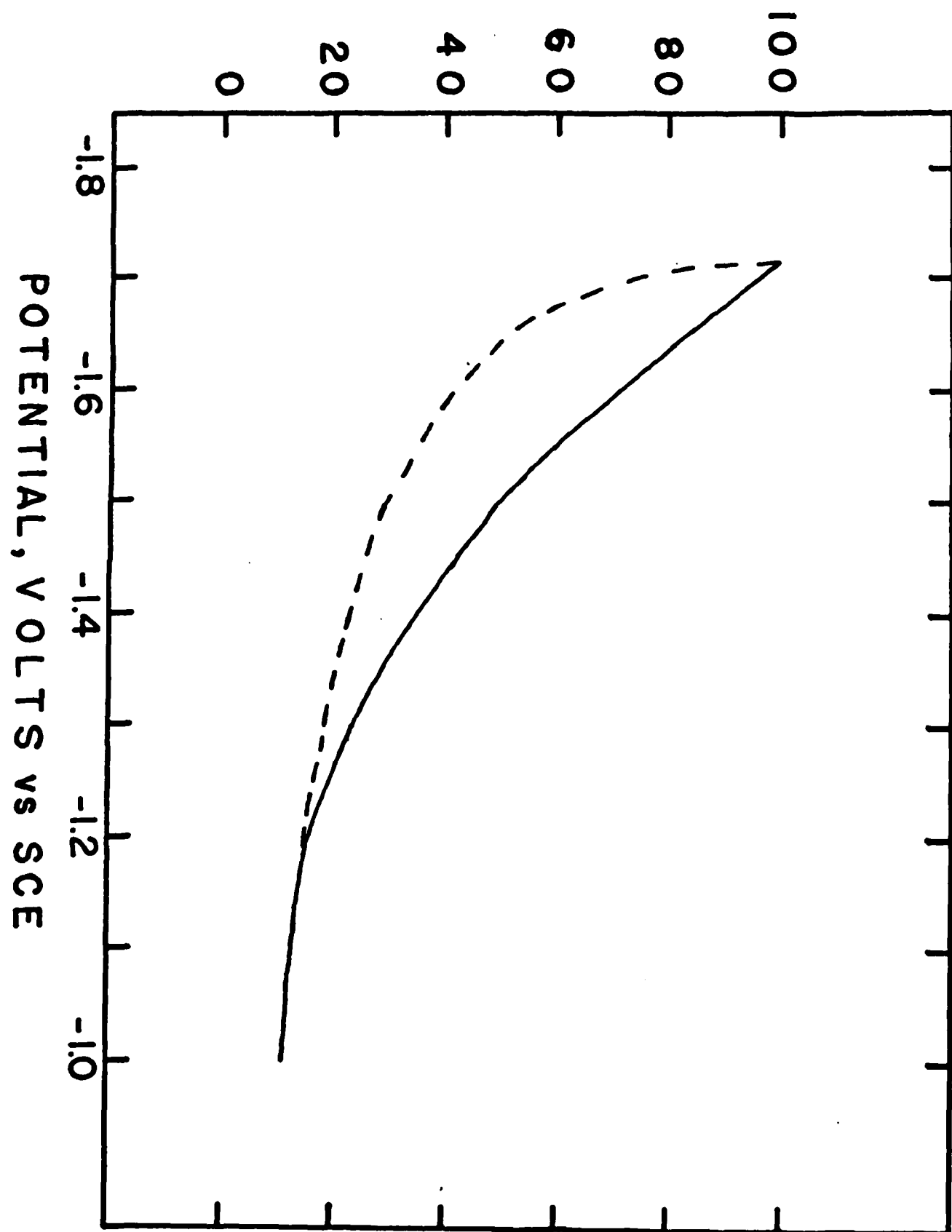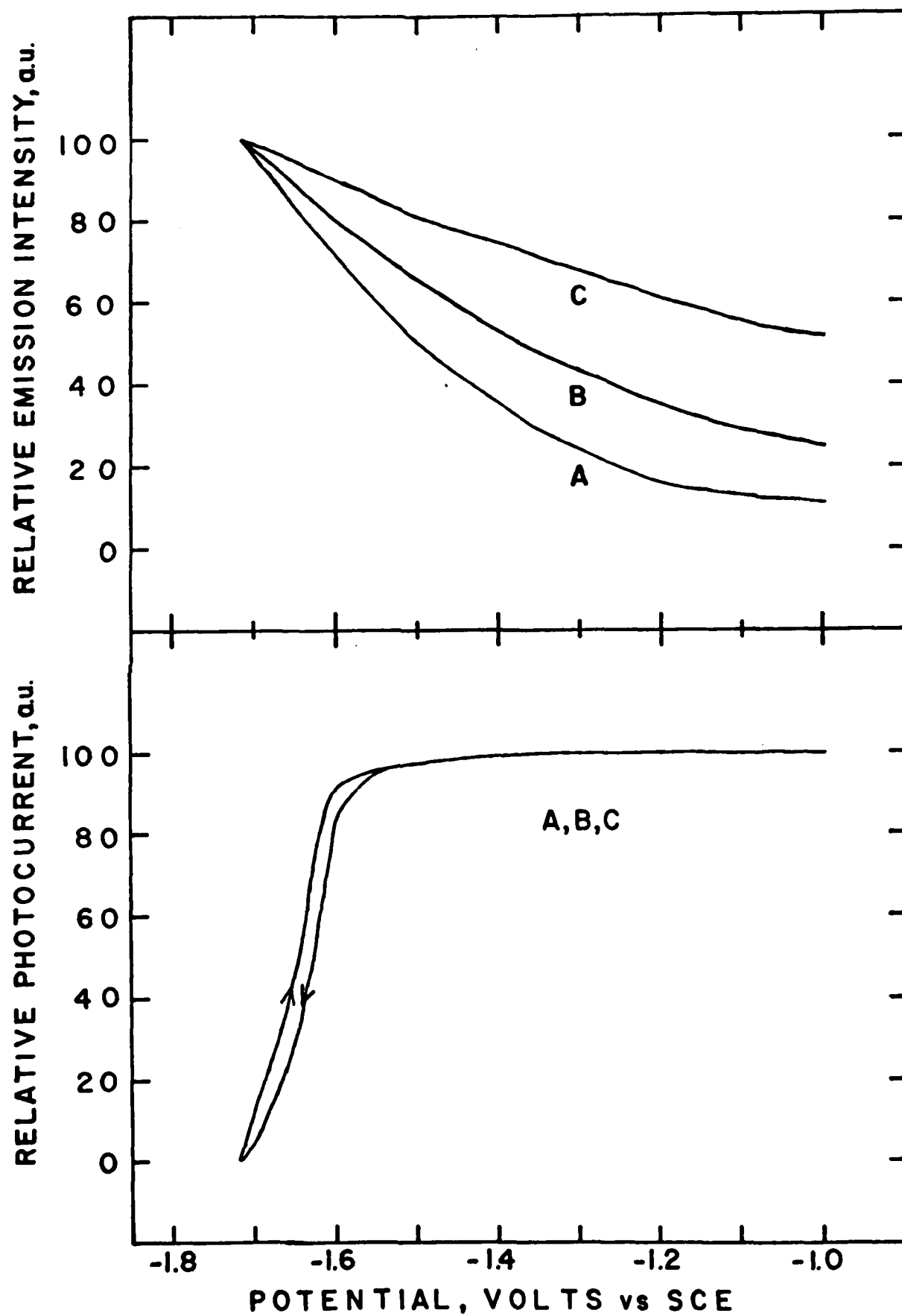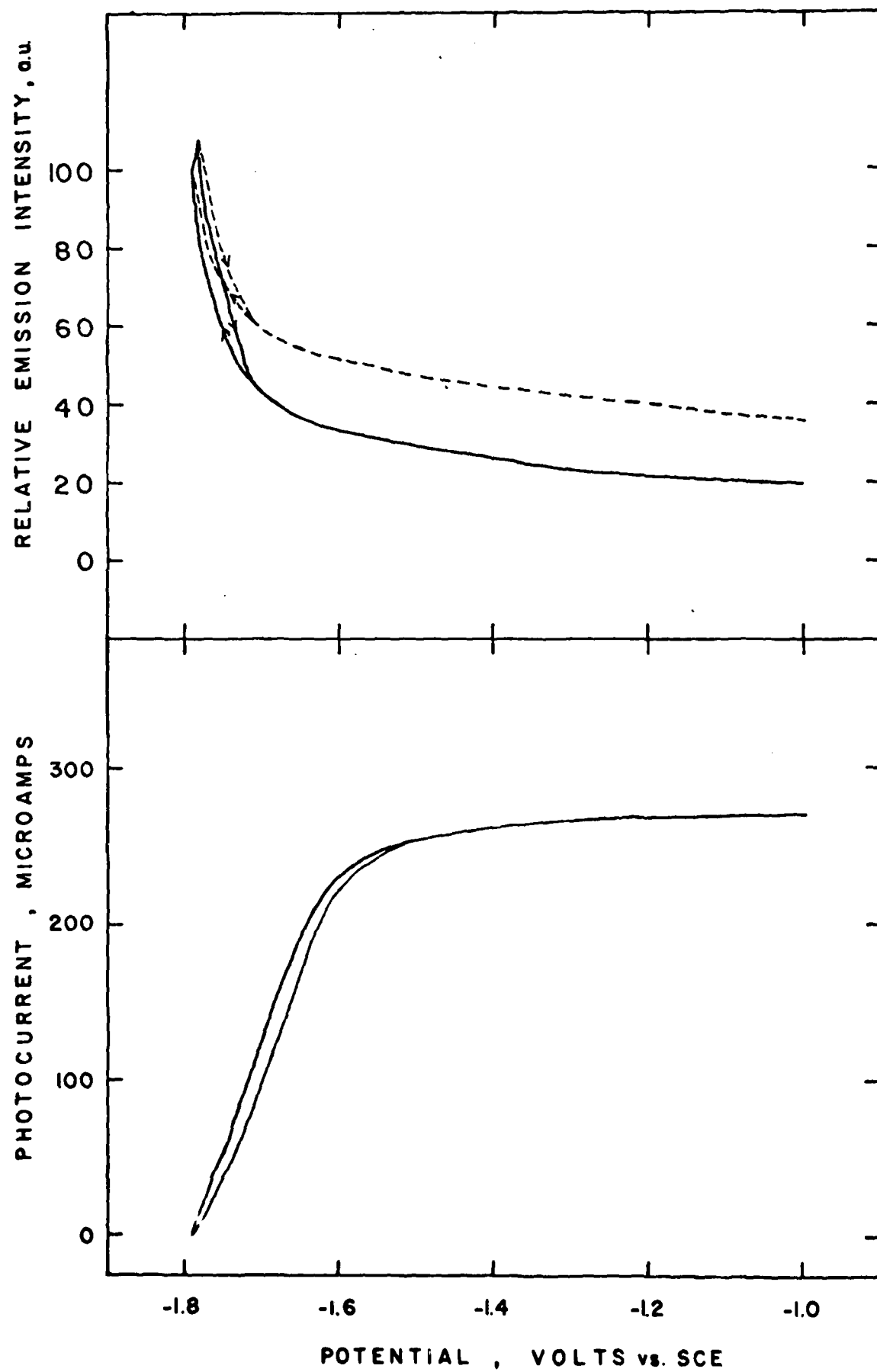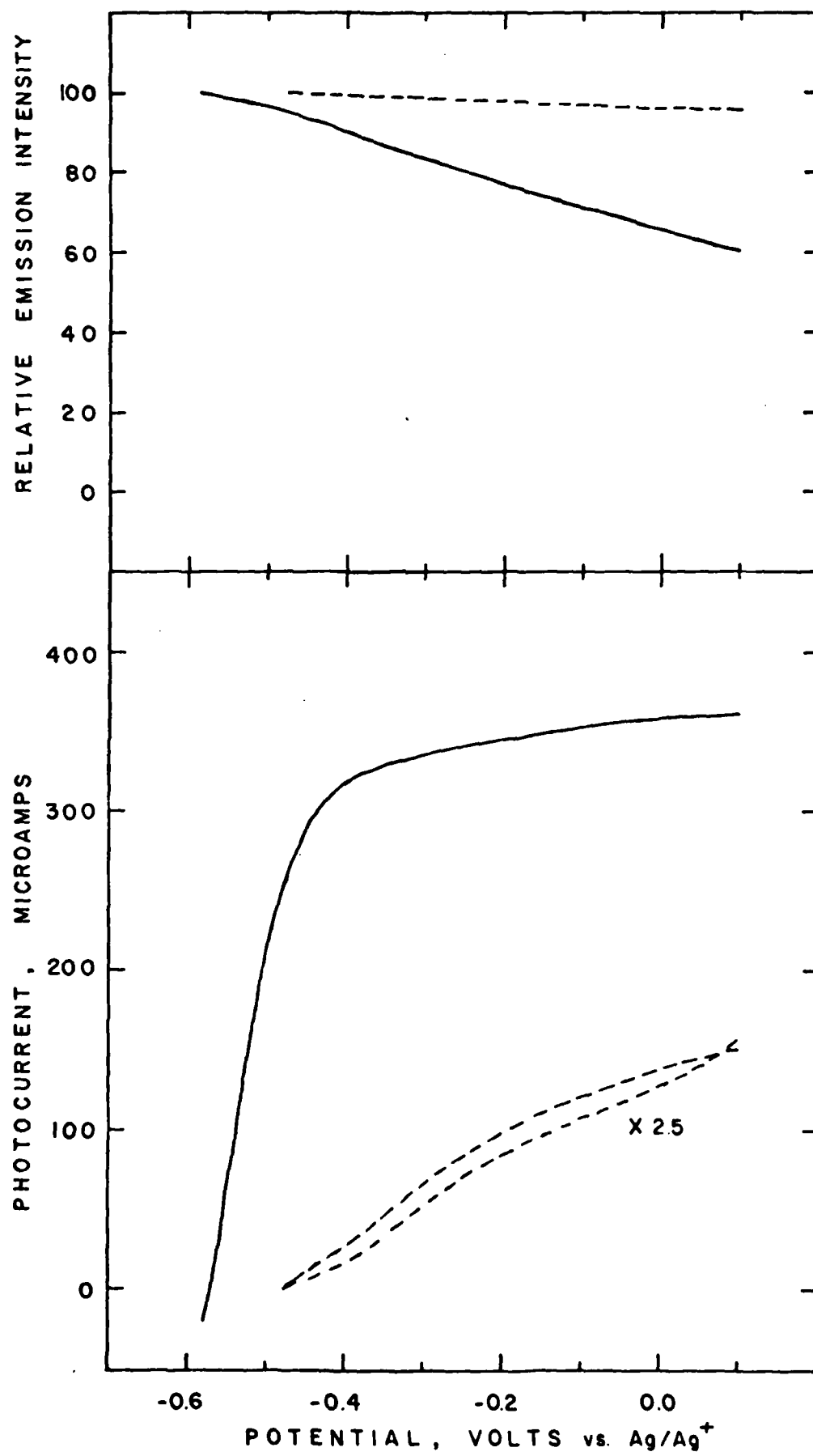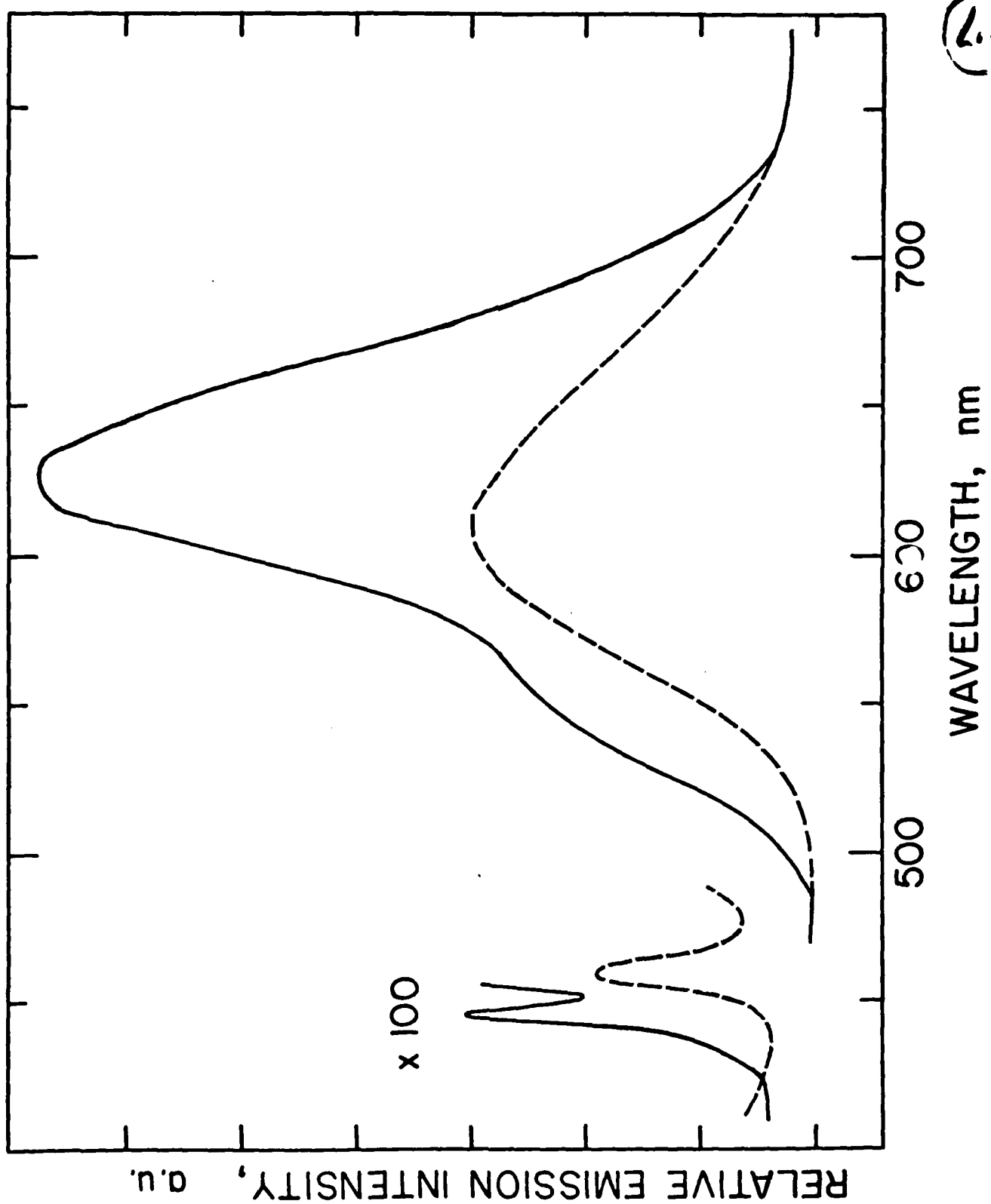
POTENTIAL, VOLTS vs SCE

JMP / 231C004 / OCT 83 / A6 3 / 35%

RELATIVE EMISSION INTENSITY

PHOTOCURRENT, MICROAMPS

X 2.5

POTENTIAL, VOLTS vs. Ag/Ag$^+$

x 100

RELATIVE EMISSION INTENSITY, a.u.

WAVELENGTH, nm

500   600   700

METAL SEMICONDUCTOR ELECTROLYTE

$$1 \quad S_2O_8^{2-} + e_{CB}^- \longrightarrow SO_4^{2-} + SO_4^{\cdot -}$$

$$2 \quad SO_4^{\cdot -} \longrightarrow SO_4^{2-} + h_{VB}^+$$

$$3 \quad h\nu$$

Fig. 3 PIMS

45

RELATIVE EMISSION INTENSITY, a.u. vs WAVELENGTH, nm

RELATIVE EMISSION INTENSITY, a.u.

WAVELENGTH, nm

RELATIVE EMISSION INTENSITY, a.u.

WAVELENGTH, nm

PHOTOCURRENT, μA

POTENTIAL, VOLTS vs. SCE

(a) -1.30 V

(b) -1.45 V

(c) -1.60 V

RELATIVE EMISSION INTENSITY, a.u.

WAVELENGTH, nm

PATTERNED MULTI-COLORED EMISSION

green

CdS

orange

CdS.5 Se.5

red

CdSe
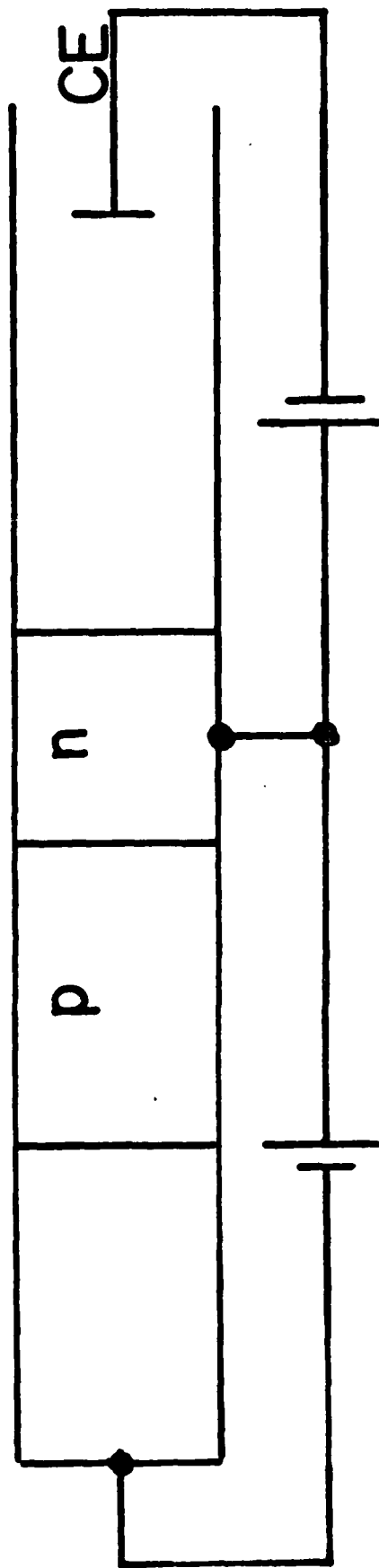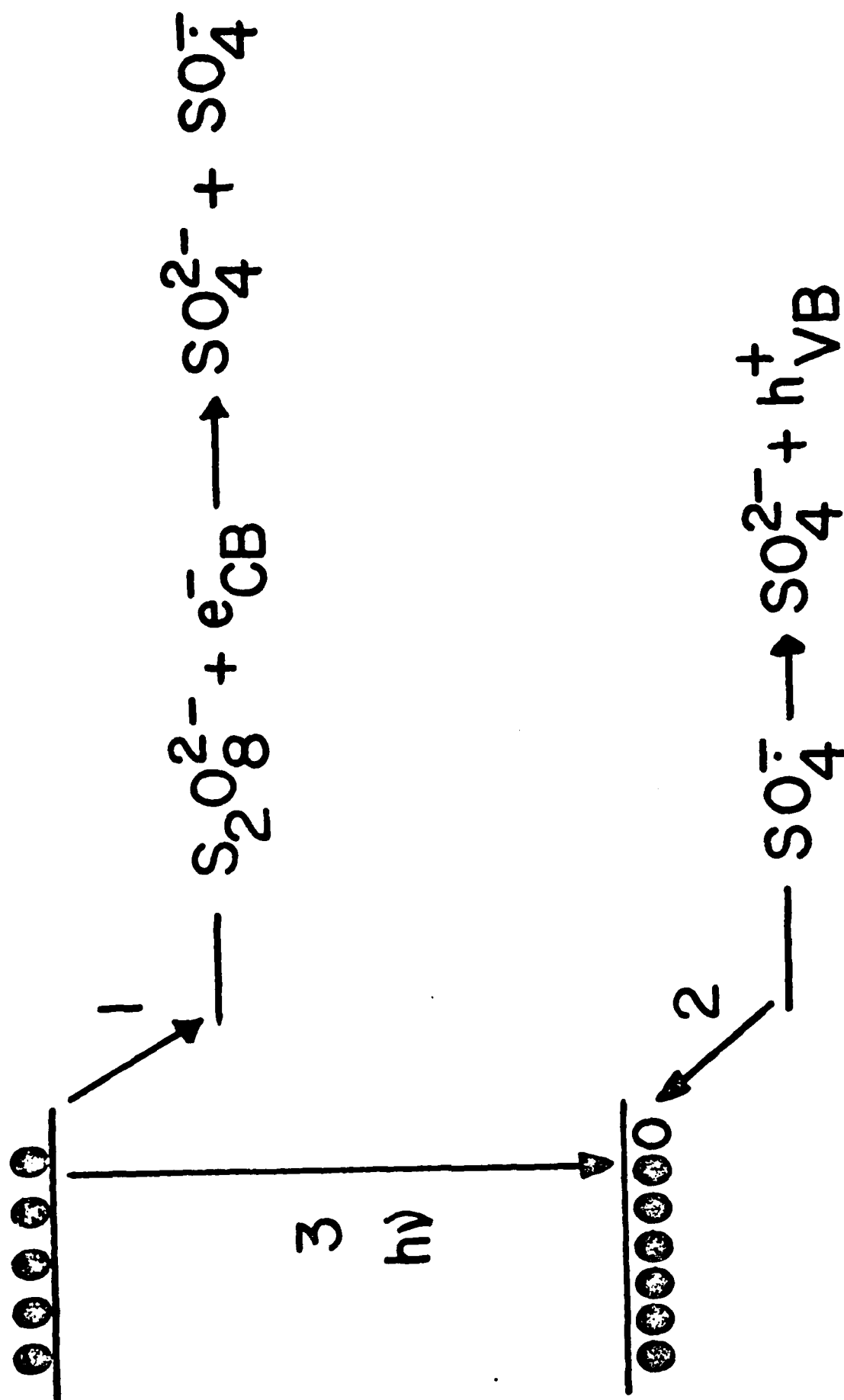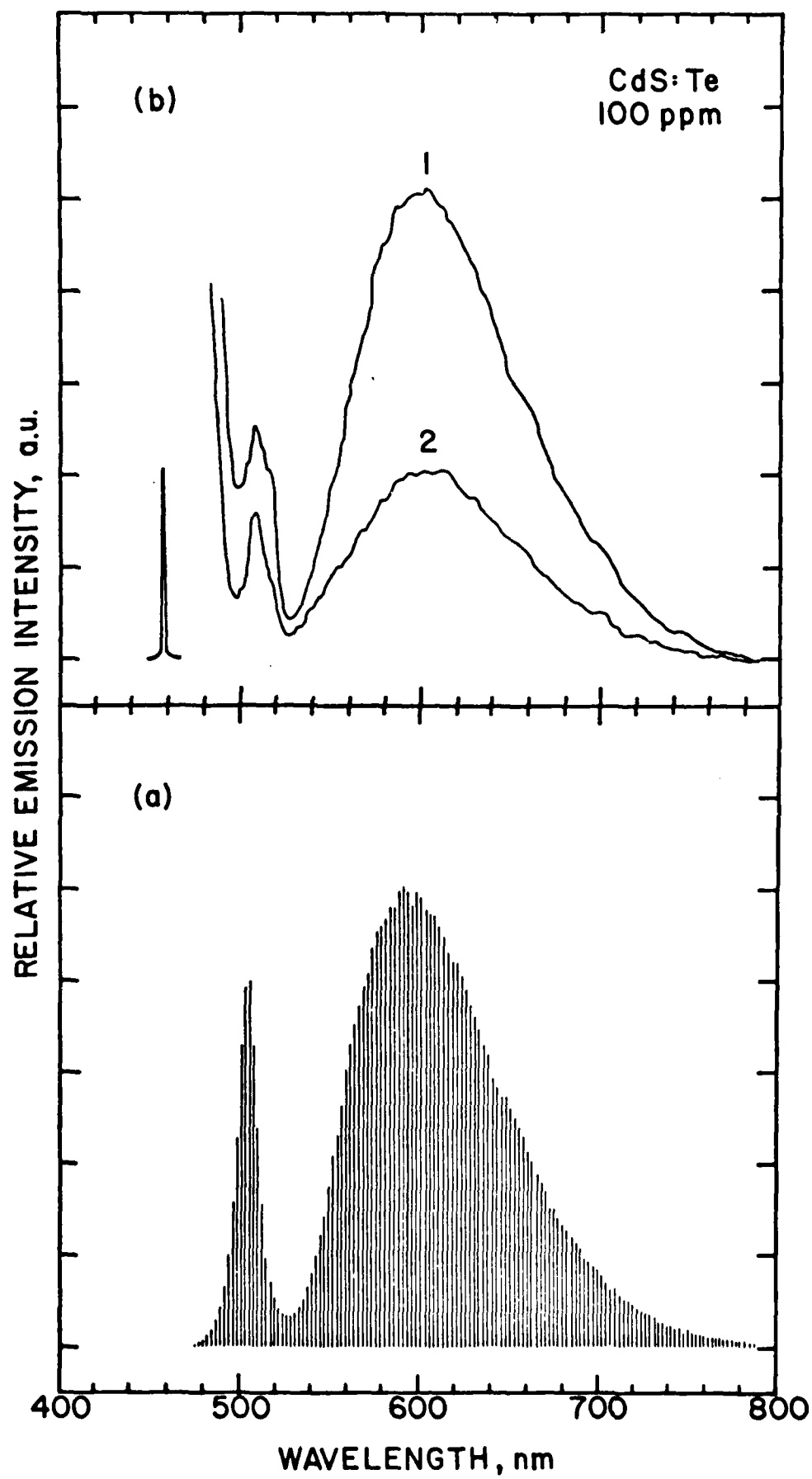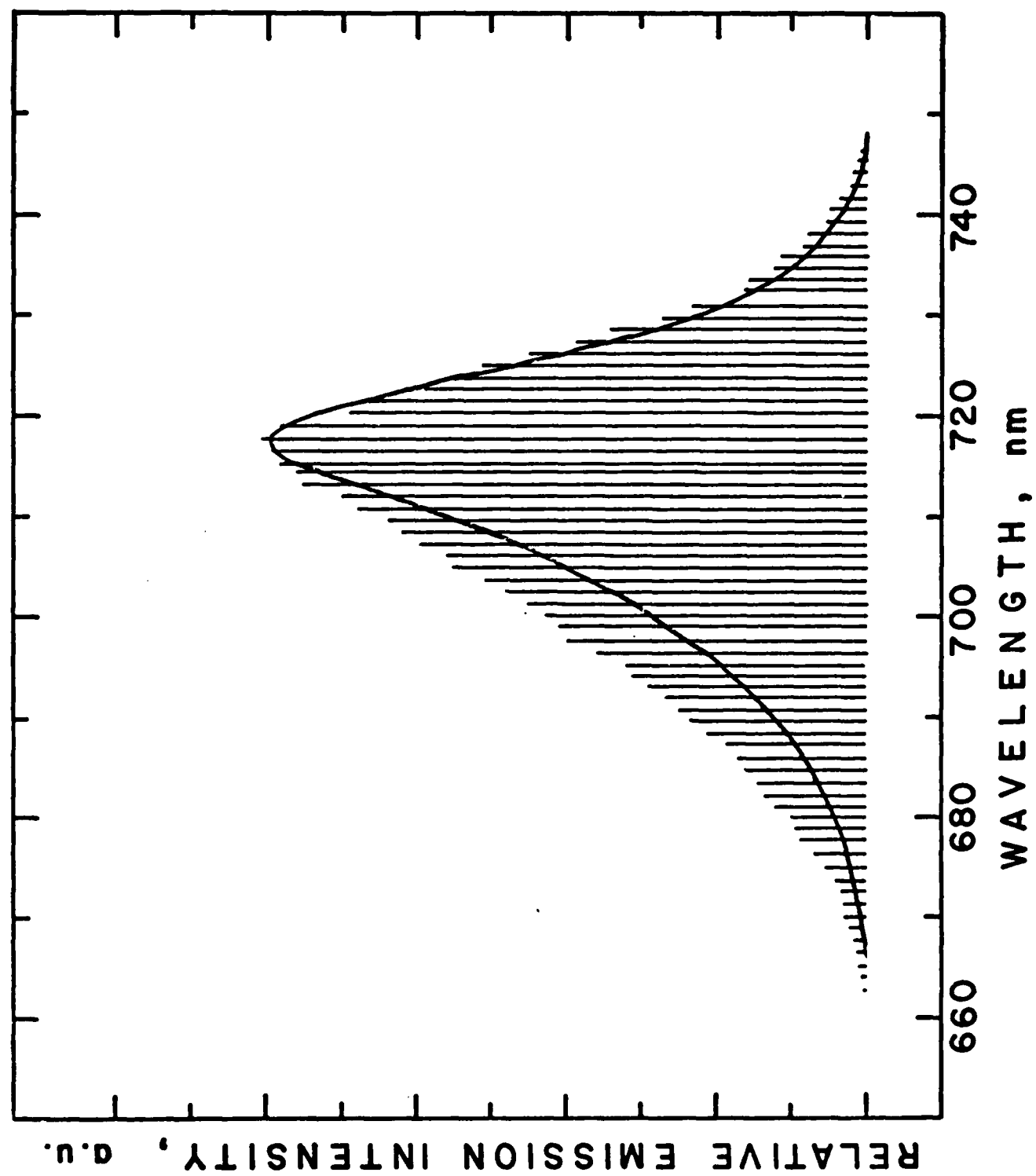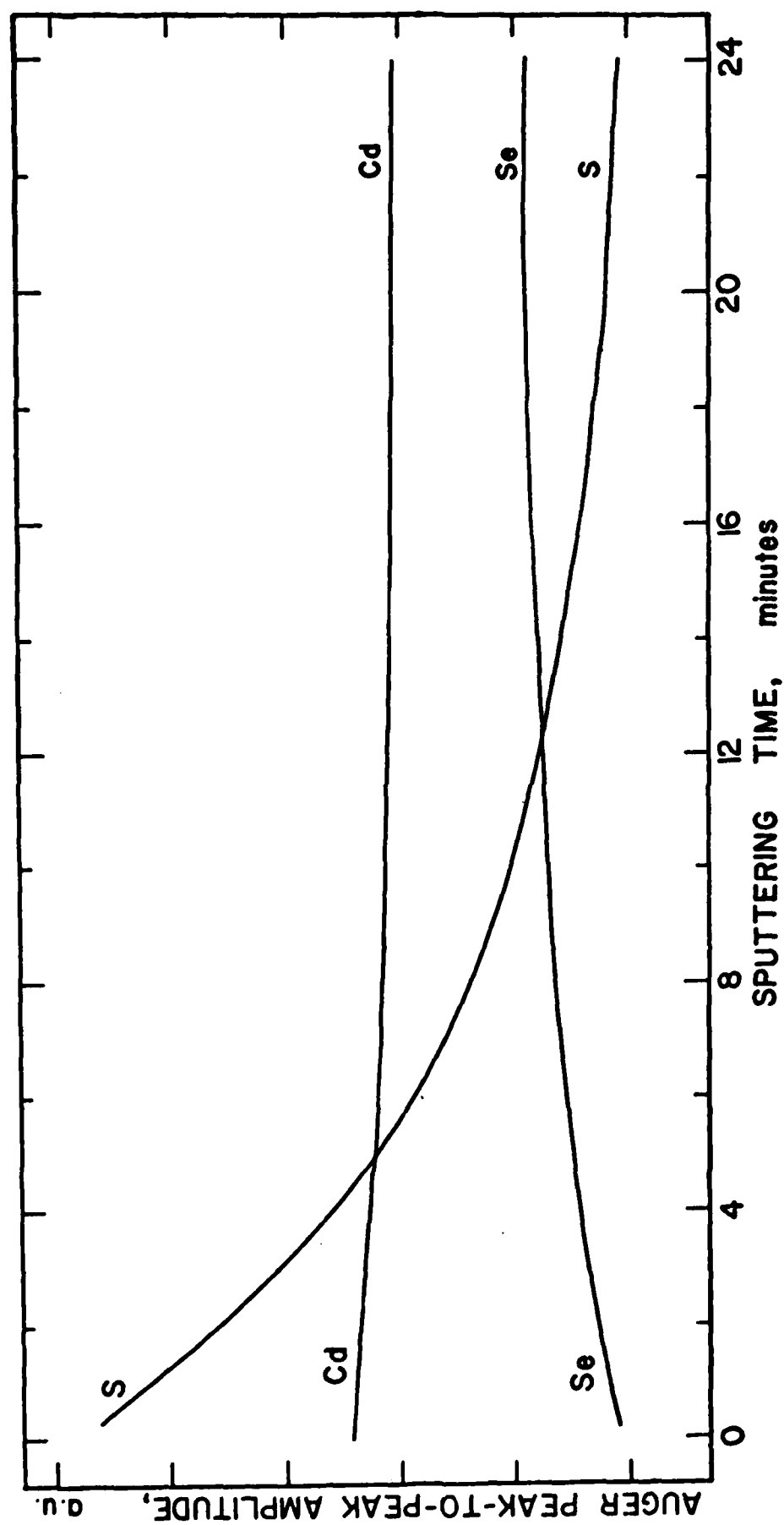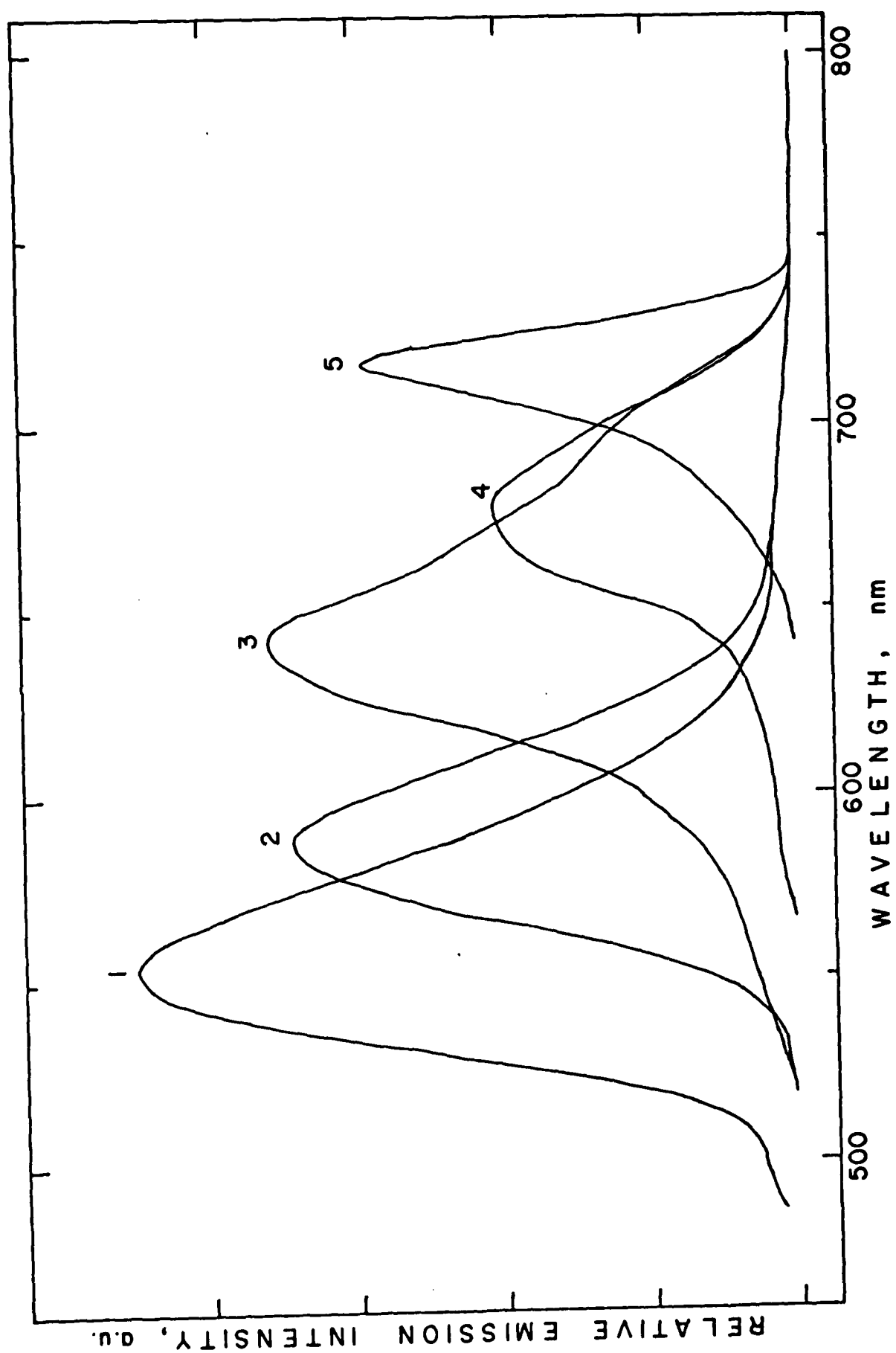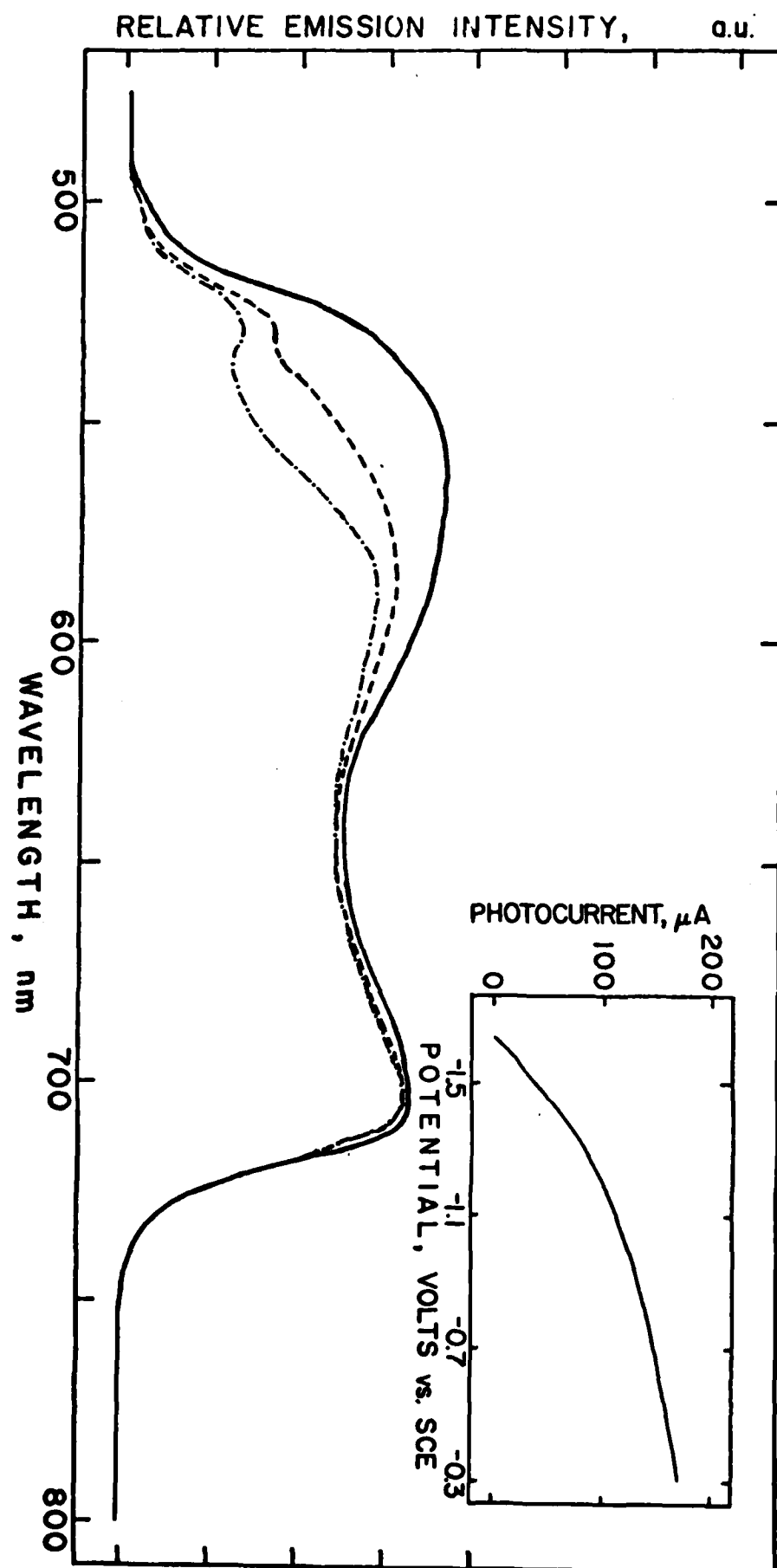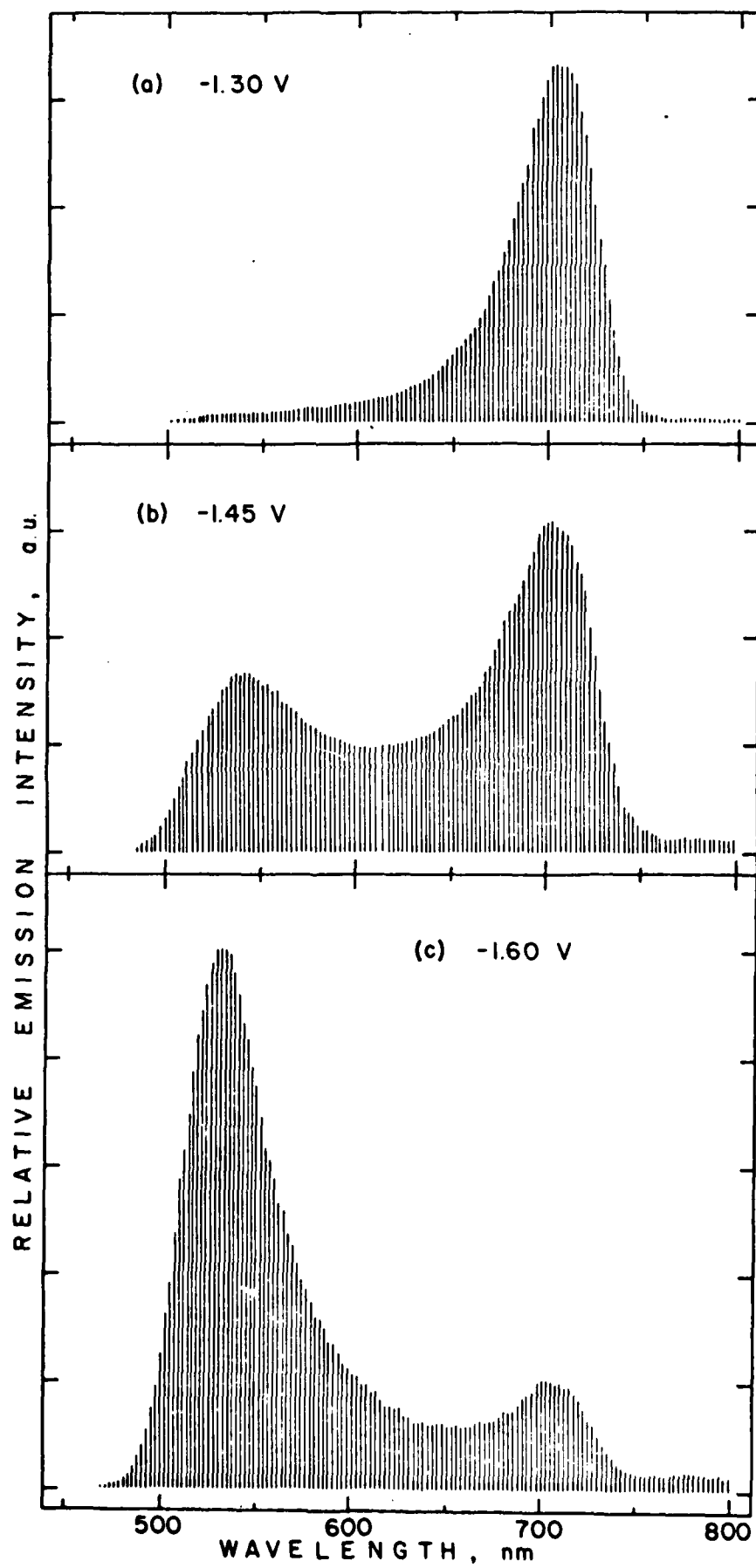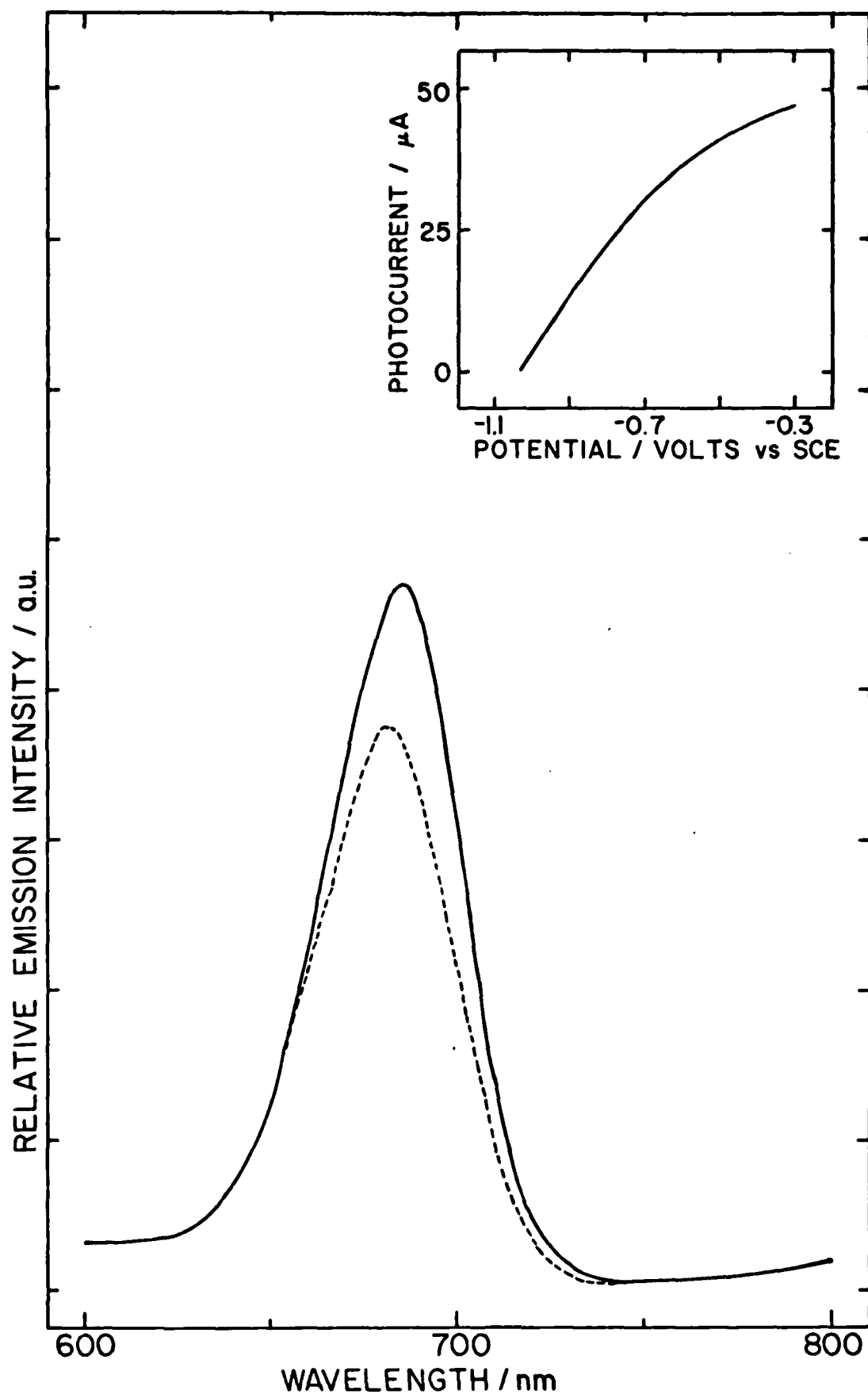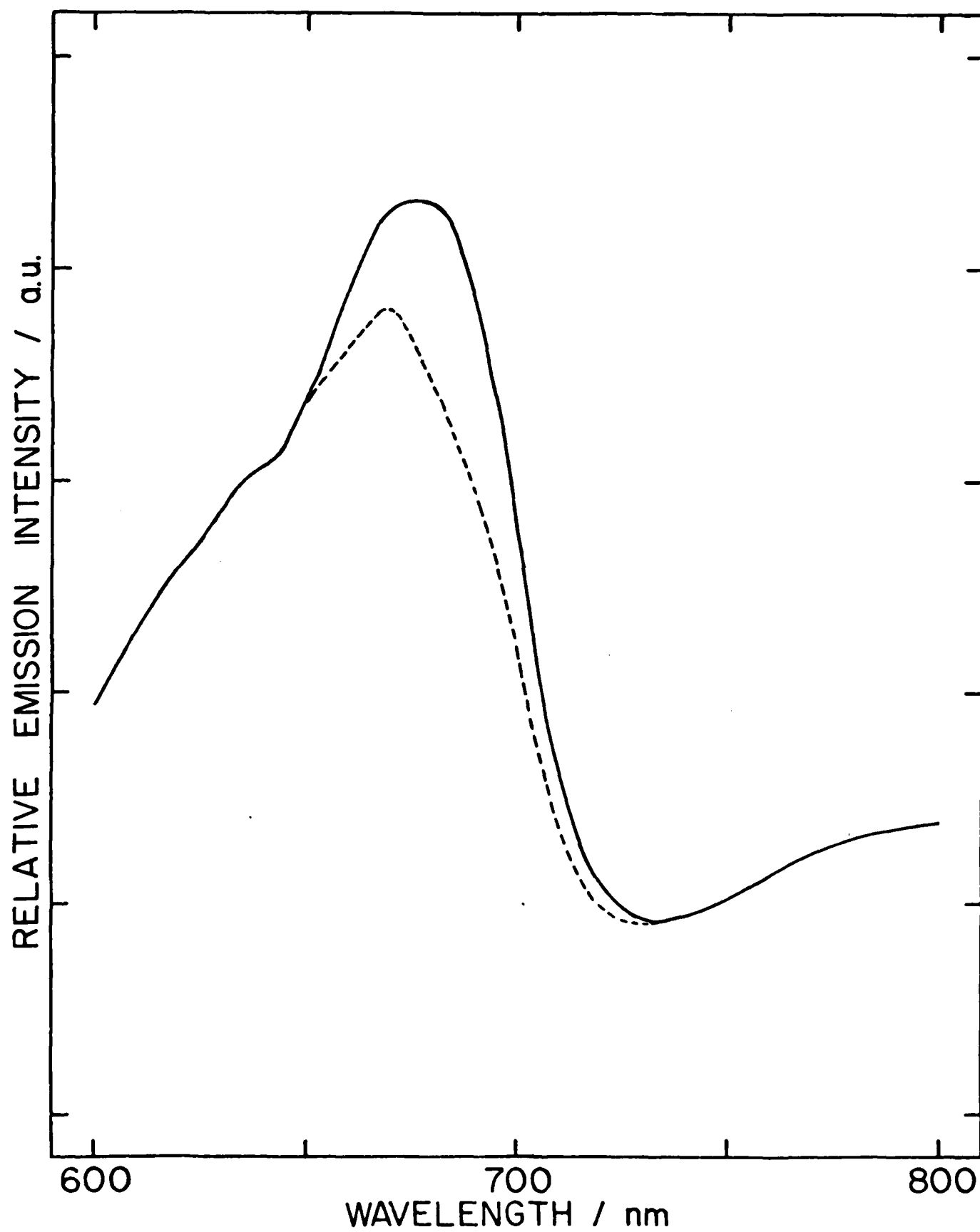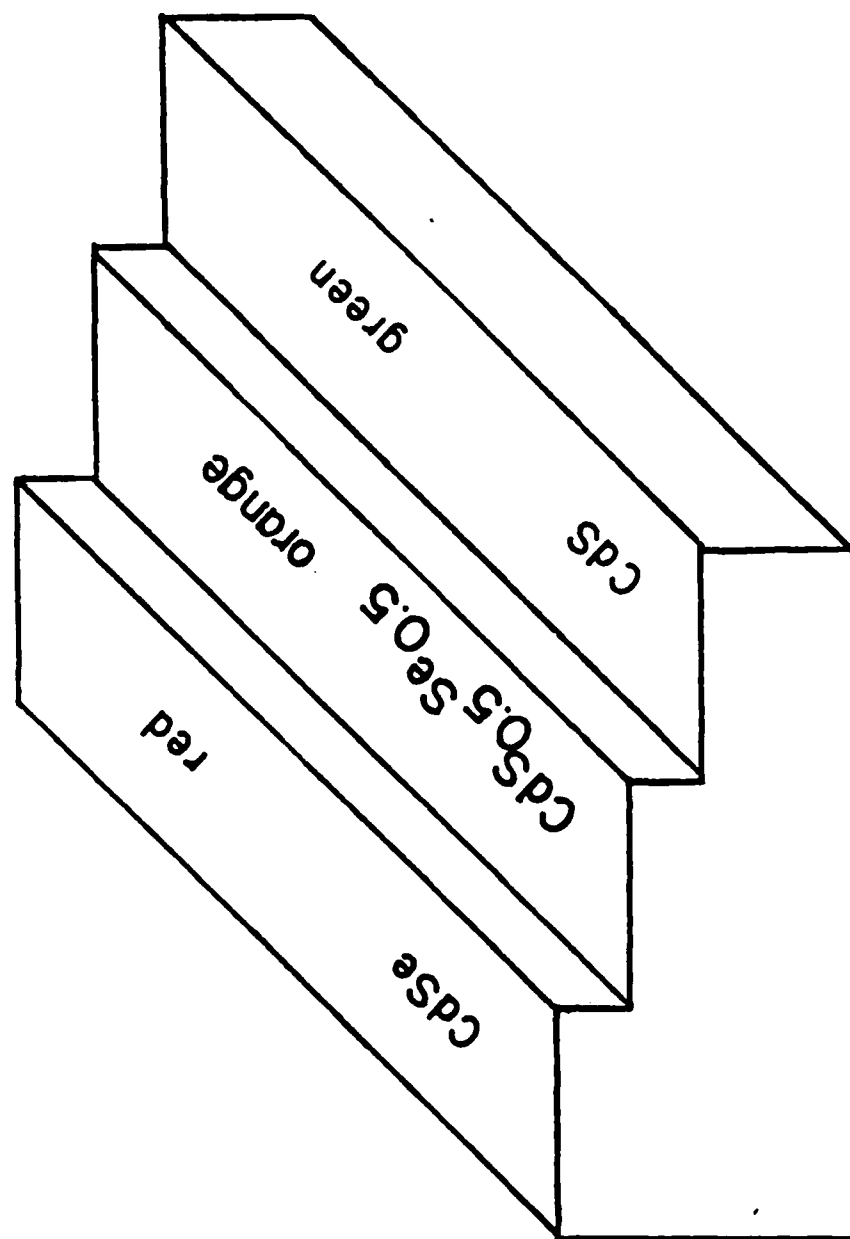
Samples prepared by spatially-controlled chemical etching.

$GaAs_{1-x}P_x$ —— $GaAs_{1-y}P_y$ ——→

I_0

$I_0 \exp(-\alpha^s D)$

$I_0 \exp(-\alpha^s X)$

D

X
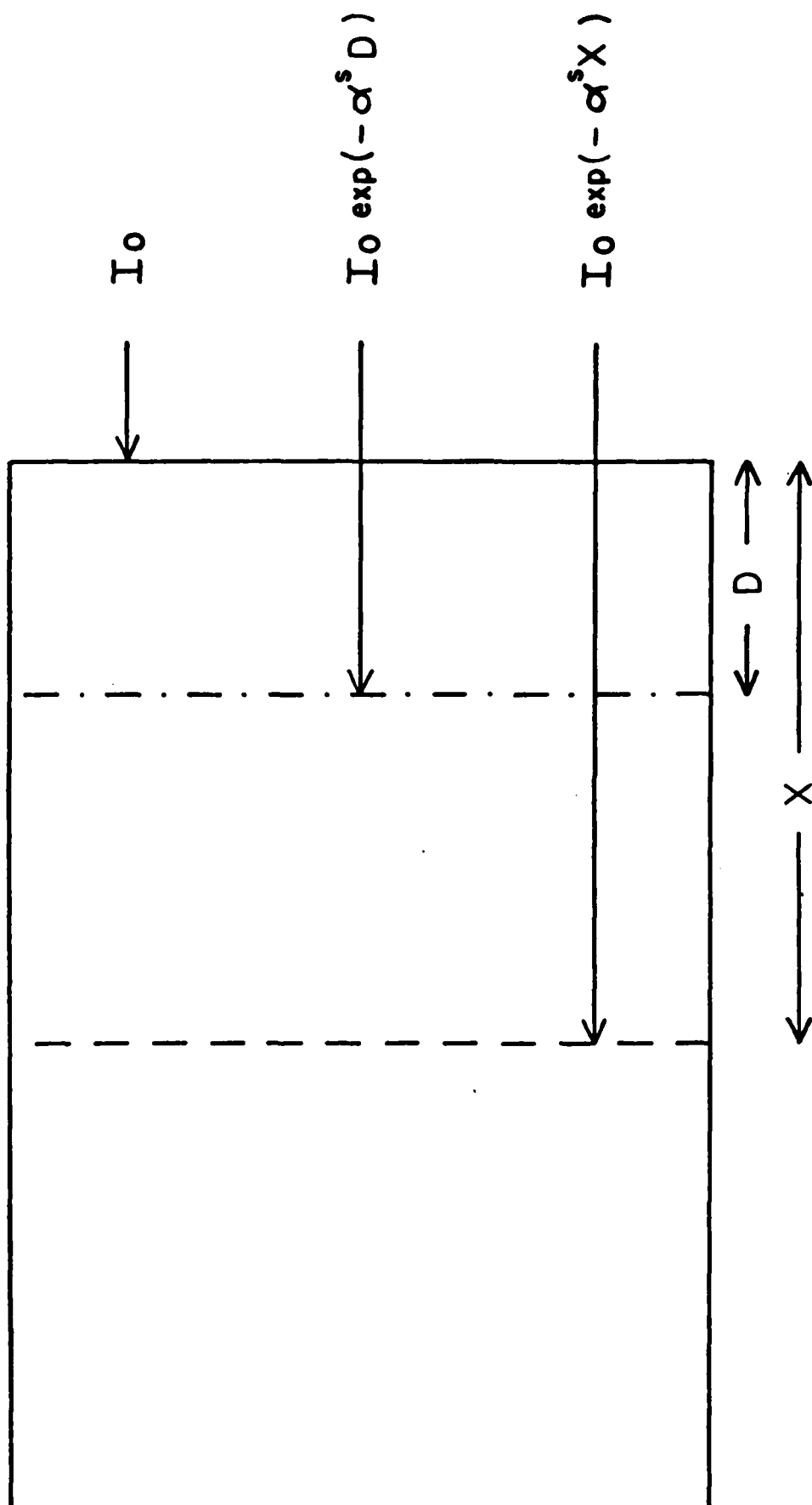
$$D = -\frac{1}{\alpha^s} \ln\left\{\frac{PL^s}{PL_0^s}\left[1-\exp(-\alpha^s X)\right]+\exp(-\alpha^s X)\right\}$$
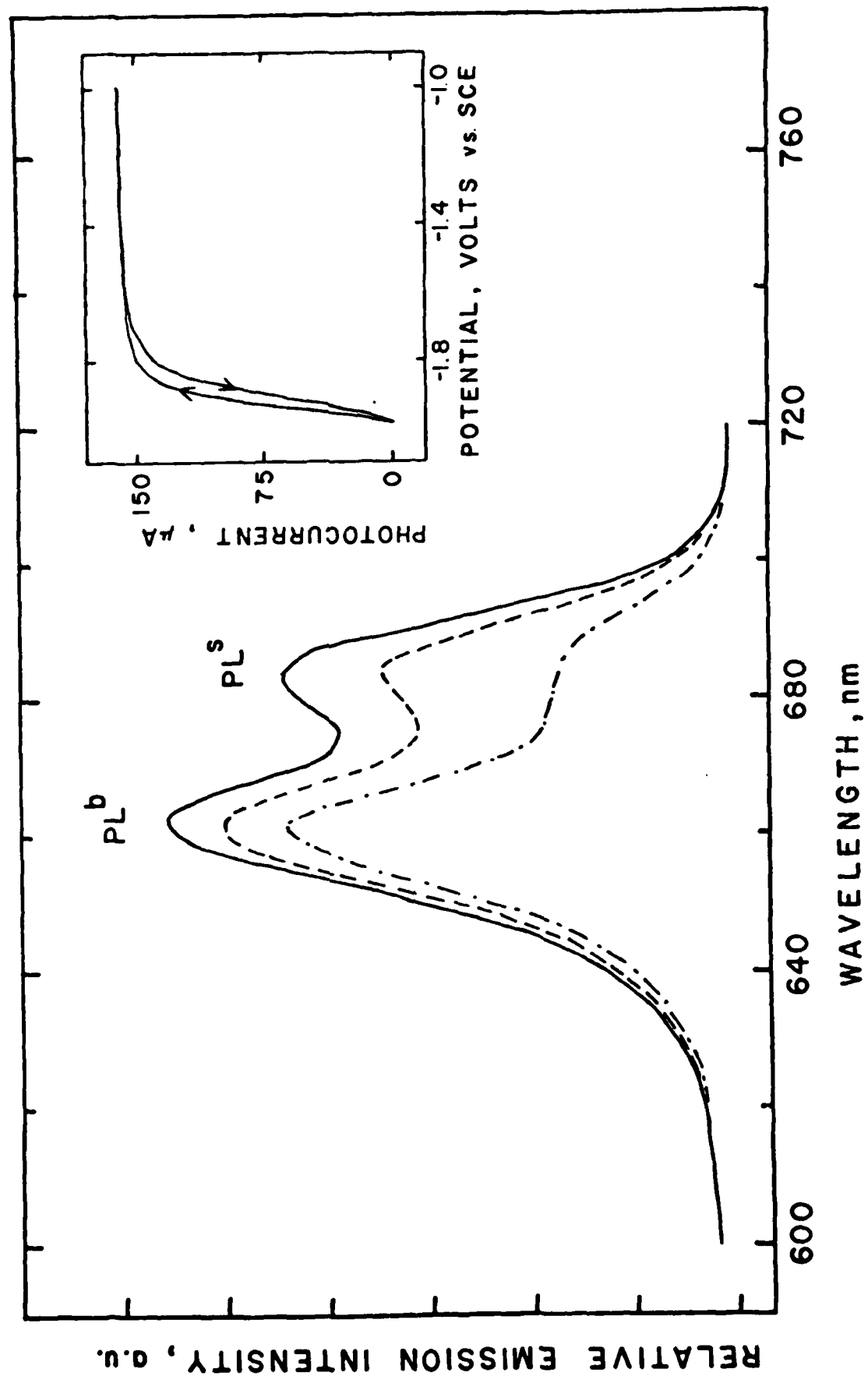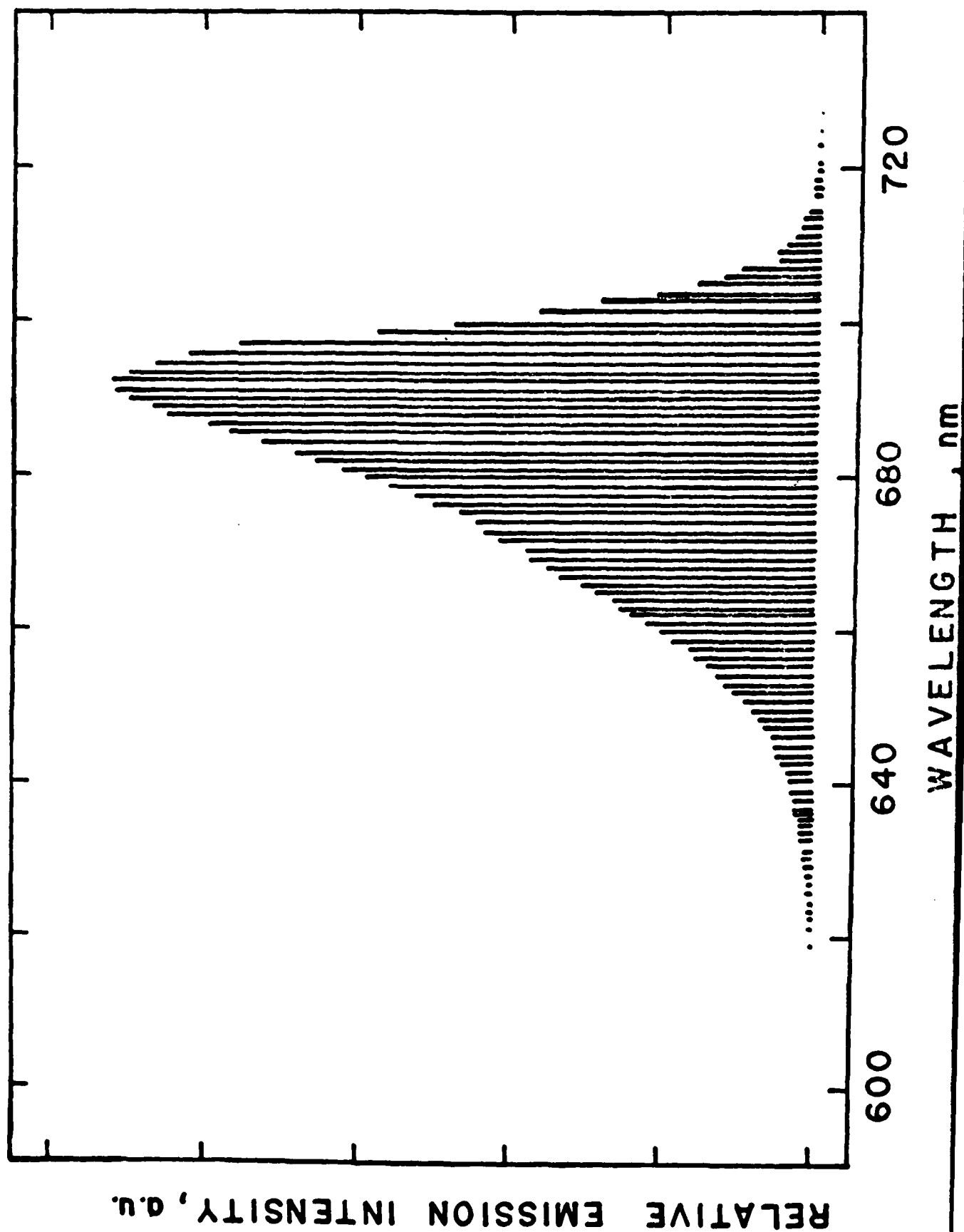
OL/413/83/01
GEN/413-2

TECHNICAL REPORT DISTRIBUTION LIST, GEN

	No. Copies		No. Copies
Office of Naval Research Attn: Code 413 800 N. Quincy Street Arlington, Virginia 22217	2	Dr. David Young Code 334 NORDA NSTL, Mississippi 39529	1
Dr. Bernard Douda Naval Weapons Support Center Code 5042 Crane, Indiana 47522	1	Naval Weapons Center Attn: Dr. Ron Atkins Chemistry Division China Lake, California 93555	1
Commander, Naval Air Systems Command Attn: Code 310C (H. Rosenwasser) Washington, D.C. 20360	1	Scientific Advisor Commandant of the Marine Corps Code RD-1 Washington, D.C. 20380	1
Naval Civil Engineering Laboratory Attn: Dr. R. W. Drisko Port Hueneme, California 93401	1	U.S. Army Research Office Attn: CRD-AA-IP P.O. Box 12211 Research Triangle Park, NC 27709	1
Defense Technical Information Center Building 5, Cameron Station Alexandria, Virginia 22314	12	Mr. John Boyle Materials Branch Naval Ship Engineering Center Philadelphia, Pennsylvania 19112	1
DTNSRDC Attn: Dr. G. Bosmajian Applied Chemistry Division Annapolis, Maryland 21401	1	Naval Ocean Systems Center Attn: Dr. S. Yamamoto Marine Sciences Division San Diego, California 91232	1
Dr. William Tolles Superintendent Chemistry Division, Code 6100 Naval Research Laboratory	1		

END

FILMED

10-85

DTIC